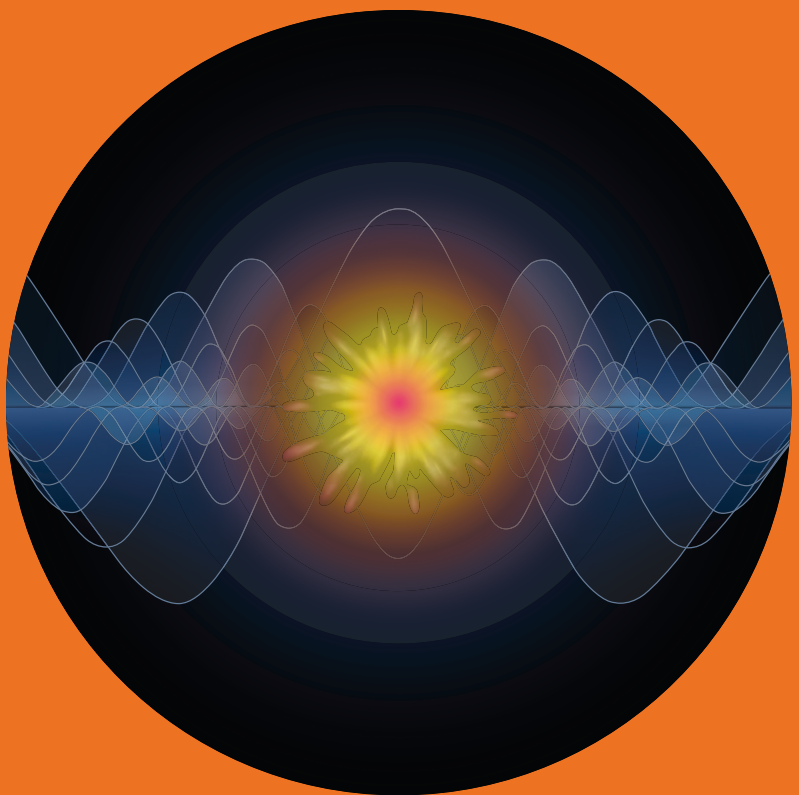# From Quantum Optics to Energy and Momentum Transport in Macroscopic Structures

**Mikko Partanen**

# From Quantum Optics to Energy and Momentum Transport in Macroscopic Structures

**Mikko Partanen**

A doctoral dissertation completed for the degree of Doctor of Science (Technology) to be defended, with the permission of the Aalto University School of Science, at a public examination held at the lecture hall F239a of the school on 26 October 2017 at 12.

**Aalto University**
**School of Science**
**Department of Neuroscience and Biomedical Engineering**
**Engineered Nanosystems group**

**Supervising professor**
Prof. Jukka Tulkki

**Thesis advisors**
D.Sc. (Tech.) Teppo Häyrynen
D.Sc. (Tech.) Jani Oksanen

**Preliminary examiners**
Prof. Kalle-Antti Suominen, University of Turku, Finland
Prof. Tero Setälä, University of Eastern Finland, Finland

**Opponent**
Prof. Martijn Wubs, Technical University of Denmark, Denmark

441    697
Printed matter

**Abstract**

One of the most intriguing quantum phenomena of light is the wave–particle duality which is related to the inability of the classical wave and particle concepts to fully describe the behavior of quantum objects. Theoretically, the wave features of the electromagnetic field, such as interference, follow from the solution of Maxwell's equations while particle features are a consequence of the field quantization, in which the electromagnetic field is described to consist of discrete energy packets, photons. Due to the wave–particle duality, for example, simultaneous description of optical absorption, emission, and interference of propagating fields has conventionally not been considered feasible using local optical models but has required using Maxwell's equations with stochastic source terms accounting for the wave–particle duality. Also the description of the momentum of light in a medium has been problematic.

In the research described in this thesis, the quantized fluctuational electrodynamics (QFED) model is derived based on combining the electromagnetic Green's functions to the field quantization to describe the position dependence of the photon number and local thermal balance in general non-equilibrium conditions, and to separate the electromagnetic field into parts propagating in different directions in resonant structures, which has conventionally been problematic due to interference effects. The QFED method is shown to resolve the previously found anomalies in the canonical commutation relations of photon ladder operators. The QFED method is also used to derive quantum optical field–matter interaction parameters fully capturing the interference, emission, damping, and scattering of propagating photons in stratified media leading to an interference-exact radiative transfer equation (RTE) model. Therefore, the derived interaction parameters solve the problem of simultaneously describing interference and losses in the widely used RTE framework.

The particle aspects of light are also studied by directly applying the conservation laws of nature and the special theory of relativity to show that light propagating in a medium must be described as mass-polariton (MP) quasiparticles, covariant coupled states of the field and matter. These quasiparticles are shown to have momentum of the Minkowski form and a nonzero mass that is carried by a mass density wave associated with light. The field–matter interaction related to the MP quasiparticles also leads to the dissipation of photon energy. These particle model results are also derived using a wave-based optoelastic continuum dynamics (OCD) approach following from the electrodynamics of continuous media and the continuum mechanics. The obtained results verify the full agreement between the wave and particle models when they are correctly applied. The key finding that a light pulse propagating in a medium is inevitably associated with an experimentally measurable mass implies a fundamental change in the prevailing perceptions of light.

# A! Aalto-yliopisto

**Tiivistelmä**

**Tiivistelmä**

Eräs kiehtovimmista valon kvantti-ilmiöistä on aalto–hiukkasdualismi, joka liittyy klassisten aalto- ja hiukkaskäsitysten kykenemättömyyteen kuvata täydellisesti kvanttiobjektien käyttäytymistä. Teoreettisesti sähkömagneettisen kentän aalto-ominaisuudet, kuten interferenssi, seuraavat Maxwellin yhtälöiden ratkaisusta kun taas hiukkasominaisuudet ovat seuraus kentän kvanttiteoriasta, jossa sähkömagneettinen kenttä kuvataan muodostuvaksi erillisistä energiapaketeista, fotoneista. Aalto–hiukkasdualismista johtuen esimerkiksi etenevien kenttien optisen absorption, emission ja interferenssin samanaikaista kuvausta ei ole tavanomaisesti pidetty lokaaleja optisia malleja käyttäen mahdollisena vaan kuvaus on vaatinut Maxwellin yhtälöiden käyttöä stokastisten lähdetermien kanssa, jotta aalto–hiukkasdualismi tulee huomioitua. Myös valon liikemäärän kuvaaminen väliaineessa on ollut ongelmallista.

Väitöskirjassa kuvatussa tutkimuksessa johdetaan kvanttifluktuaatioelektrodynamiikan (QFED) malli, joka perustuu sähkömagneettisten Greenin funktioiden ja kentän kvanttiteorian yhdistämiseen, jotta voidaan kuvata fotonien lukumäärän ja paikallisen termisen tasapainon paikkariippuvuutta yleisissä epätasapainotilanteissa ja erottaa sähkömagneettinen kenttä eri suuntiin eteneviin osiin resonanssirakenteissa, mikä on tavanomaisesti ollut ongelmallista interferenssi-ilmiöistä johtuen. QFED-menetelmän näytetään hävittävän aiemmin löydetyt anomaliat fotonien tikapuuoperaattoreiden kommutaatiorelaatioissa. QFED-menetelmää käytetään myös kvanttioptisten kentän ja aineen vuorovaikutusparametrien johtamiseen. Nämä parametrit ottavat täysin huomioon fotonien interferenssin, emission, vaimenemisen ja sironnan kerroksellisissa rakenteissa johtaen interferenssin suhteen eksaktiin säteilyn siirtoyhtälöön (RTE). Näin ollen johdetut vuorovaikutusparametrit ratkaisevat interferenssin ja häviöiden samanaikaisen kuvaamisen ongelmat laajasti käytetyssä RTE-mallin viitekehyksessä.

Valon hiukkasominaisuuksia tutkitaan myös soveltamalla suoraan luonnon säilymislakeja ja erityistä suhteellisuusteoriaa sen näyttämiseen, että väliaineessa etenevä valo täytyy kuvata massapolaritonikvasihiukkasina (MP), kovariantteina kentän ja aineen kytkettyinä tiloina. Näillä kvasihiukkasilla näytetään olevan Minkowskin muotoa oleva liikemäärä ja nollasta poikkeava massa, jota kuljettaa valoon aineessa liittyvä massatiheysaalto. MP-kvasihiukkasiin liittyvä kentän ja aineen vuorovaikutus myös johtaa fotonin energian menetykseen. Nämä hiukkasmallin tulokset johdetaan myös käyttäen aaltoperustaista optoelastista jatkumodynamiikan (OCD) mallia, joka seuraa jatkuvan aineen sähködynamiikasta ja mekaniikasta. Saadut tulokset vahvistavat aalto- ja hiukkasmallien täyden yhtäpitävyyden niitä oikein käytettäessä. Päätulos, jonka mukaan väliaineessa etenevään valopulssiin liittyy väistämättä kokeellisesti mitattavissa oleva massa, merkitsee perustavanlaatuista muutosta valoon liittyvissä vallitsevissa käsityksissä.

# Preface

This work has been carried out between 2013 and 2017 in the Engineered Nanosystems group at the Department of Neuroscience and Biomedical Engineering at Aalto University, School of Science. First of all, I would like to express my warmest gratitude to my thesis instructors, Dr. Jani Oksanen and Dr. Teppo Häyrynen, for all their guidance, encouragement, and challenging projects throughout my doctoral studies. Especially, I want to thank them for asking challenging research questions and for patiently suggesting ways to more clearly express my thoughts when writing the publications and this compiling part of the dissertation. I also want to thank my supervisor, Prof. Jukka Tulkki, for his guidance, providing the excellent working environment, and also for the time we spent together in the process of writing the last publication included in this thesis.

During the years, it has been a pleasure to discuss, have lunch, and share office with excellent colleagues. Especially, I want to thank the present and former group members Kimmo Sääskilahti, Pyry Kivisaari, Toufik Sadi, Oskari Heikkilä, Ville Saarikivi, Teemu Laakso, Anders Olsson, Jonna Tiira, Ivan Radevici, and Tuomas Haggren for their company. My thanks also go to Mikko Hakala, Jarkko Salmi, and Janne Blomqvist from Aalto IT for keeping the computers running. In addition, I want to thank Eeva Lampinen, Marita Stenman, Henrika Wilkman, Susanna Väänänen, and Katja Korpinurmi for arranging practical matters.

In March 2017, I got an opportunity for a brief visit to the University of Connecticut in Storrs, USA. I am very grateful to Prof. Juha Javanainen for the opportunity and his kind hospitality. I also want to thank Prof. George Gibson, Prof. Winthrop Smith, and Prof. Phillip Gould for the laboratory tours and interesting discussions that made my stay memorable. I also want to thank the organizers of the great summer schools

that I attended during my doctoral studies: Nanoscale Radiative Heat Transfer, Les Houghes, France 2013; European School on Nanosciences and Nanotechnologies (ESONN), Grenoble, France, 2014; and Photonic Integrated Compound Quantum Encoding (PICQUE) Scientific School, Rome, Italy, 2015.

I would also like to thank my family and friends. I want to thank my parents Leena and Jari for sincere and invaluable support for everything I have decided to do in my life. I also want to thank my brother and colleague Matti and my sister Minna. I could not have hoped for a better brother and sister. Finally, I want to thank my dear Tarja for the support and the great moments we have had and will have in our life. I would also like to thank Tarja for sharing her opinions on how to improve certain visualizations including the cover image of this thesis.

Otaniemi, September 25, 2017,

Mikko Partanen

# Contents

# List of publications

This thesis consists of an overview and of the following publications which are referred to in the text by their Roman numerals.

**I** Mikko Partanen, Teppo Häyrynen, Jani Oksanen, and Jukka Tulkki. Noiseless amplification of weak coherent fields exploiting energy fluctuations of the field. *Physical Review A*, **86**, 063804, December 2012.

**II** Mikko Partanen, Teppo Häyrynen, Jani Oksanen, and Jukka Tulkki. Thermal balance and photon-number quantization in layered structures. *Physical Review A*, **89**, 033831, March 2014.

**III** Mikko Partanen, Teppo Häyrynen, Jani Oksanen, and Jukka Tulkki. Unified position-dependent photon-number quantization in layered structures. *Physical Review A*, **90**, 063804, December 2014.

**IV** Mikko Partanen, Teppo Häyrynen, Jukka Tulkki, and Jani Oksanen. Commutation-relation-preserving ladder operators for propagating optical fields in nonuniform lossy media. *Physical Review A*, **92**, 033839, September 2015.

**V** Mikko Partanen, Teppo Häyrynen, Jukka Tulkki, and Jani Oksanen. Generalized noise terms for the quantized fluctuational electrodynamics. *Journal of Physics B*, **50**, 055503, February 2017.

**VI** Mikko Partanen, Teppo Häyrynen, Jukka Tulkki, and Jani Oksanen. Quantized fluctuational electrodynamics for three-dimensional plasmonic structures. *Physical Review A*, **95**, 013848, January 2017.

**VII**  Mikko Partanen, Teppo Häyrynen, and Jani Oksanen. Interference-exact radiative transfer equation. *Scientific Reports*, **7**, 11534, September 2017.

**VIII**  Mikko Partanen, Teppo Häyrynen, Jani Oksanen, and Jukka Tulkki. Photon mass drag and the momentum of light in a medium. *Physical Review A*, **95**, 063850, June 2017.

# Author's contribution

The author wrote the first draft, developed and adapted the required theoretical and numerical models, and performed the calculations and numerical analysis in Publications I–VII. The concept of the coupled state of the field and matter was elaborated in a trial and error process as a joint effort in Publication VIII, where the author performed the theoretical and numerical calculations and had an essential role in interpreting the main results and writing the manuscript.

The author was also the first author of the following articles in conference proceedings written on the topics of this thesis:

- Mikko Partanen, Teppo Häyrynen, Jani Oksanen, and Jukka Tulkki, "Noiseless amplification of weak coherent fields without external energy," Proc. SPIE **8773**, 877312, Photon Counting Applications IV; and Quantum Optics and Quantum Information Transfer and Processing, Prague, Czech Republic (2013).

- Mikko Partanen, Teppo Häyrynen, Jani Oksanen, and Jukka Tulkki, "Position-dependent photon operators in the quantization of the electromagnetic field in dielectrics at local thermal equilibrium," Proc. SPIE **9136**, 91362B, Nonlinear Optics and Its Applications VIII; and Quantum Optics III, Brussels, Belgium (2014).

- Mikko Partanen, Teppo Häyrynen, Jani Oksanen, and Jukka Tulkki, "Photon momentum and optical forces in cavities," Proc. SPIE **9742**, 974217, Physics and Simulation of Optoelectronic Devices XXIV, San Francisco, California, USA (2016).

- Mikko Partanen and Jukka Tulkki, "Momentum and rest mass of the covariant state of light in a medium," Proc. SPIE **10098**, 100980P, Physics and Simulation of Optoelectronic Devices XXV, San Francisco, California, USA (2017).

The author also had a minor role in the theoretical modeling part of the following experimental paper closely related to the topics of this thesis:

- A. Olsson, J. Tiira, M. Partanen, T. Hakkarainen, E. Koivusalo, A. Tukiainen, M. Guina, and J. Oksanen, "Optical energy transfer and loss mechanisms in coupled intracavity light emitters," IEEE Trans. Electron Dev. **63**, 3567 (2016).

# List of abbreviations

| | |
|---|---|
| CEV | Center of energy velocity |
| FDT | Fluctuation–dissipation theorem |
| FED | Fluctuational electrodynamics |
| IFDOS | Interference density of states |
| IOF | Input–output formalism |
| LDOS | Local density of states |
| LTE | Local thermal equilibrium |
| MDW | Mass density wave |
| MP | Mass-polariton |
| NLDOS | Nonlocal density of states |
| NOF | Noise operator formalism |
| OCD | Optoelastic continuum dynamics |
| QED | Quantum electrodynamics |
| QFED | Quantized fluctuational electrodynamics |
| QND | Quantum nondemolition |
| QW | Quantum well |
| RTE | Radiative transfer equation |
| SP | Surface plasmon |

List of abbreviations

# List of symbols

| | |
|---|---|
| $\boldsymbol{\alpha}$ | RTE-coefficient matrix |
| $\alpha$ | Basis variable of a coherent basis |
| $\alpha_{\pm}$ | Damping coefficients for photon numbers |
| $\beta_{\pm}$ | Scattering coefficients for photon numbers |
| $\gamma$ | Lorentz factor |
| $\delta_{jk}$ | Kronecker symbol |
| $\delta(\mathbf{r} - \mathbf{r}')$ | Dirac delta function |
| $\delta_{\mathrm{T}}(\mathbf{r} - \mathbf{r}')$ | Transverse delta function |
| $\varepsilon$ | Relative permittivity of a material |
| $\varepsilon_0$ | Permittivity of vacuum |
| $\varepsilon_{\mathrm{i}}$ | Imaginary part of the relative permittivity of a material |
| $\varepsilon_{\mathrm{r}}$ | Real part of the relative permittivity of a material |
| $\boldsymbol{\eta}$ | Vector formed of source-field photon numbers |
| $\hat{\eta}$ | Photon number operator of the source field |
| $\Theta$ | Average energy of a quantum harmonic oscillator |
| $\kappa$ | Spring constant of a harmonic oscillator |
| $\lambda$ | Wavelength of light in a medium |
| $\lambda_0$ | Wavelength of light in vacuum |
| $\mu$ | Relative permeability of a material |
| $\mu_0$ | Permeability of vacuum |
| $\mu_{\mathrm{i}}$ | Imaginary part of the relative permeability of a material |

| | |
|---|---|
| $\mu_{\mathrm{r}}$ | Real part of the relative permeability of a material |
| $\rho$ | Electromagnetic local density of states |
| $\rho_{\pm}$ | Local densities of states for propagating fields |
| $\rho_0$ | Equilibrium mass density of a medium |
| $\rho_{\mathrm{a}}$ | Atomic mass density |
| $\rho_{\mathrm{e}}$ | Electric local density of states |
| $\rho_{\mathrm{f}}$ | Electric charge density of free charges |
| $\rho_{\mathrm{IF}}$ | Interference density of states |
| $\rho_{\mathrm{m}}$ | Magnetic local density of states |
| $\rho_{\mathrm{MDW}}$ | Mass density of a mass density wave |
| $\rho_{\mathrm{NL}}$ | Nonlocal density of states |
| $\rho_{\mathrm{rec}}$ | Mass density perturbance due to the recoil effect |
| $\hat{\rho}$ | Density operator |
| $\phi$ | Phase angle |
| $\chi_{\mathrm{e}}$ | Electric susceptibility |
| $\chi_{\mathrm{m}}$ | Magnetic susceptibility |
| $\omega$ | Angular frequency |
| $\omega_0$ | Central angular frequency of a light pulse |
| $\omega_{\tau}$ | Damping frequency |
| $\omega_{\mathrm{p}}$ | Plasma frequency |
| $\Delta\omega$ | Spectral width of a light pulse |
| $\hat{\mathbf{A}}$ | Vector potential operator |
| $A$ | Cross-sectional area |
| $\hat{A}$ | Magnitude of the vector potential operator |
| $\hat{a}$ | Photon annihilation operator |
| $\hat{a}_{\pm}$ | Photon annihilation operators of propagating fields |
| $\hat{a}_{\mathrm{e}}$ | Electric part of the photon annihilation operator |
| $\hat{a}_{\mathrm{m}}$ | Magnetic part of the photon annihilation operator |
| $\hat{a}^{\dagger}$ | Photon creation operator |

| | |
|---|---|
| $\hat{a}^{\dagger}_{\pm}$ | Photon creation operators of propagating fields |
| $\hat{a}^{\dagger}_{e}$ | Electric part of the photon creation operator |
| $\hat{a}^{\dagger}_{m}$ | Magnetic part of the photon creation operator |
| $\mathbf{B}$ | Magnetic field density |
| $B$ | Bulk modulus |
| $C$ | Normalization factor of the annihilation operator |
| $c$ | Speed of light in vacuum |
| $\mathbf{D}$ | Displacement field |
| $\mathbf{E}$ | Electric field |
| $\hat{\mathbf{E}}$ | Electric field operator |
| $E$ | Energy |
| $E_0$ | Electromagnetic energy of a light pulse |
| $E_g$ | Band gap energy |
| $E_{\mathrm{MP}}$ | Total energy of a mass-polariton |
| $\hat{E}$ | Magnitude of the electric field operator |
| $\hat{\mathbf{e}}$ | Polarization unit vector |
| $F$ | Fidelity |
| $F_{\mathrm{eff}}$ | Effective fidelity |
| $F_{\mathrm{ideal}}$ | Ideal fidelity |
| $\mathbf{f}_{\mathrm{el}}$ | Elastic force density |
| $\mathbf{f}_{\mathrm{opt}}$ | Optical force density |
| $\hat{f}_{e}$ | Electric noise field operator |
| $\hat{f}_{m}$ | Magnetic noise field operator |
| $\overset{\leftrightarrow}{\mathbf{G}}$ | Dyadic Green's function |
| $\overset{\leftrightarrow}{\mathbf{g}}$ | Spectral dyadic Green's function |
| $G$ | Shear modulus or scalar component of the Green's function |
| $\hat{G}$ | Approximative amplification operator |
| $g$ | Gain of amplification |
| $g_{\mathrm{eff}}$ | Effective gain of amplification |

| | |
|---|---|
| $\mathbf{H}$ | Magnetic field |
| $\hat{\mathbf{H}}$ | Magnetic field operator |
| $\hat{H}$ | Magnitude of the magnetic field operator |
| $h$ | Planck constant |
| $\hbar$ | Reduced Planck constant |
| $\overset{\leftrightarrow}{\mathbf{I}}$ | Unit dyadic |
| $\mathbf{J}_\mathrm{e}$ | Polarization current density |
| $\mathbf{J}_\mathrm{f}$ | Current density of free charges |
| $\mathbf{J}_\mathrm{m}$ | Magnetization current density |
| $\hat{J}_\mathrm{e}$ | Electric noise-current operator |
| $\hat{J}_\mathrm{e,abs}$ | Electric absorption-current operator |
| $\hat{J}_\mathrm{e,tot}$ | Total electric noise-current operator |
| $\hat{J}_\mathrm{m}$ | Magnetic noise-current operator |
| $\hat{J}_\mathrm{m,abs}$ | Magnetic absorption-current operator |
| $\hat{J}_\mathrm{m,tot}$ | Total magnetic noise-current operator |
| $j_\mathrm{0,e}$ | Normalization factor for the electric noise-current |
| $j_\mathrm{0,m}$ | Normalization factor for the magnetic noise-current |
| $\mathbf{K}$ | Wave vector component in the $x$-$y$ plane |
| $\mathbf{k}$ | Wave vector |
| $k$ | Wavenumber in a medium |
| $k_0$ | Wavenumber in vacuum |
| $k_\mathrm{B}$ | Boltzmann's constant |
| $k_\mathrm{i}$ | Imaginary part of the wavenumber |
| $k_\mathrm{r}$ | Real part of the wavenumber |
| $k_z$ | Wave vector $z$-component |
| $k_{z,\mathrm{i}}$ | Imaginary part of the wave vector $z$-component |
| $\Delta k_x$ | Standard deviation of the wavenumber in vacuum |
| $L_n$ | Laguerre polynomial of order $n$ |
| $\delta\mathbf{M}$ | Noise in the magnetization field |

| | |
|---|---|
| $M$ | Rest mass of a medium block |
| $\delta M$ | Total mass transferred by a light pulse |
| $m_0$ | Rest mass of a particle |
| $\delta m$ | Mass transferred by a mas-polariton |
| $N_0$ | Photon number of a light pulse |
| $\mathbf{n}$ | Vector formed of propagating field photon numbers |
| $n$ | Refractive index |
| $n_i$ | Imaginary part of the refractive index |
| $n_r$ | Real part of the refractive index |
| $\hat{n}$ | Photon number operator |
| $\hat{n}_\pm$ | Photon number operators of propagating fields |
| $\hat{n}_\mathrm{e}$ | Electric part of the photon-number operator |
| $\hat{n}_\mathrm{m}$ | Magnetic part of the photon-number operator |
| $\delta\mathbf{P}$ | Noise in the polarization field |
| $p$ | Momentum |
| $p_\mathrm{field}$ | Momentum of the electromagnetic field |
| $p_\mathrm{MP}$ | Total momentum of a mass-polariton |
| $\hat{Q}$ | Net emission operator |
| $\hat{Q}_\mathrm{abs}$ | Absorption operator |
| $\hat{Q}_\mathrm{em}$ | Emission operator |
| $\mathbf{R}$ | Position vector component in the $x$-$y$ plane |
| $\mathbf{R}'$ | Field source position vector component in the $x$-$y$ plane |
| $\overset{\leftrightarrow}{\mathbf{R}}$ | Rotation matrix |
| $\mathcal{R}$ | Multi-interface reflection coefficient |
| $\mathcal{R}'$ | Reverse multi-interface reflection coefficient |
| $\mathbf{r}$ | Position vector |
| $\mathbf{r}'$ | Position vector of a field source |
| $\mathbf{r}_\mathrm{a}$ | Atomic displacement field of a medium |
| $r$ | Reflection coefficient of a field |

| | |
|---|---|
| $r'$ | Reverse reflection coefficient of a field |
| $\mathbf{S}$ | Poynting vector |
| $\mathbf{S}_{\mathrm{BS}}$ | Scattering matrix of a beam splitter |
| $\hat{\mathbf{S}}$ | Poynting vector operator |
| $S$ | Area of quantization in the $y$-$z$ plane |
| $\hat{S}$ | Magnitude of the Poynting vector operator |
| $T$ | Temperature |
| $T_{\mathrm{eff}}$ | Effective field temperature |
| $T_{\mathrm{ex}}$ | Excitation temperature |
| $\mathcal{T}$ | Multi-interface transmission coefficient |
| $\mathcal{T}'$ | Reverse multi-interface transmission coefficient |
| $t$ | Time coordinate or transmission coefficient of a field |
| $t'$ | Reverse transmission coefficient of a field |
| $\Delta t$ | Standard deviation of the temporal width of a light pulse |
| $U$ | Voltage |
| $u$ | Energy density |
| $\hat{u}$ | Energy density operator |
| $V$ | Volume of quantization or velocity of a medium block |
| $v$ | Velocity |
| $W$ | Wigner function |
| $W_{\mathrm{coh}}$ | Wigner function of a coherent state |
| $W_{|n\rangle\langle n|}$ | Wigner function of an $n$-photon Fock state |
| $W_{\mathrm{th}}$ | Wigner function of a thermal state |
| $x$ | Position coordinate on the $x$ axis |
| $x'$ | Position coordinate of a field source on the $x$ axis |
| $x^{\pm}$ | Position coordinates on each side infinitesimally close to $x$ |
| $\Delta x$ | Standard deviation of the spatial width of a light pulse |

# 1. Introduction

## 1.1 Motivation

The foundations of classical electrodynamics are laid upon Maxwell's equations which describe how electric and magnetic fields depend on charges and currents and on each other. These equations were discovered by James Clerk Maxwell in the 1860s [1, 2]. The classical electrodynamics provides an accurate description of electromagnetic phenomena whenever the field strengths and relevant length scales are large enough for the quantum mechanical effects to be negligible. Instead, for low field strengths and for small distances, the electromagnetic interactions are known to be better described by quantum electrodynamics (QED), which is the well-known quantum theory of electromagnetism developed between the 1920s and 1950s by many physicists [3–12]. QED describes how the field and matter interact at the quantum level by means of exchange of photons. It was also the first theory where full agreement between the special theory of relativity and quantum mechanics was achieved.

The downside of using QED is that, without approximations, it is extremely difficult to apply QED to complex systems including a huge amount of electromagnetically interacting particles. Such a system is formed even by an electromagnetic field and a simple dielectric medium, where there is a huge amount of induced dipoles interacting with the electromagnetic field. Additional inhomogeneities in the materials make the system even more complex. Between the pure classical and quantum approaches, there exist semiclassical theories, which aim to include some quantum features of the fields in computations, which are tractable also in quite complex geometries. One of the most widely used semiclassi-

cal theories is fluctuational electrodynamics (FED) originally developed by Sergeǐ Mikhaǐlovich Rytov in the 1950s [13, 14]. In FED, the thermal and zero-point motion of real and virtual electrically charged particles inside materials and vacuum results in a fluctuating electromagnetic field. An essential part of FED is the application of the fluctuation–dissipation theorem (FDT), which combines statistical physics, quantum physics, and macroscopic electrodynamics to relate the rate of energy dissipation in a non-equilibrium system to the spontaneous fluctuations that occur in equilibrium systems [13, 15]. The well-known FDT relates the spectral density of fluctuating charge density to the local temperature, and frequency-dependent relative dielectric permittivity of materials [13, 15]. The essence of FED is the frequency distribution of the fluctuations and its relation to the dissipation of electromagnetic waves.

The most conventional quantum approach to study the behavior of quantized electromagnetic field in simple optical instruments is the mode picture and the related input–output formalism (IOF) [16, 17]. Basically, IOF is a scattering theory approach, where the input fields are given and the output fields of the system are computed. Consequently, IOF relates the photon creation and annihilation operators of the input fields to the corresponding operators of the output fields, but it does not reveal the properties of intermediate states. In IOF, the spatial field evolution is only included in the form of mode functions that are typically arbitrarily scaled. The formalism was originally developed for dispersionless and lossless dielectrics for the study of passive optical devices, such as resonatorlike cavities, beam splitters, lenses, and filters by Knöll *et al.* in the 1980s [18, 19]. Soon, the formalism was also extended to describe lossy and dispersive media by several groups [20–25] eventually leading to a complete position-dependent noise operator formalism (NOF) [24–26]. The resulting complete quantization procedures fully account for the coupling between the electromagnetic field and the states of lossy dielectric media highlighting that the noise and field operators in general lossy systems became position dependent.

The electric field and vector potential operators in the above works using IOF obeyed the well-known canonical commutation relation for an arbitrary choice of normal mode functions as expected [23, 24]. However, the well-known canonical commutation relations of the ladder operators were not found to be generally satisfied as the ladder operators were found to

exhibit anomalies in resonant structures [27]. The anomalous commutation relations of the ladder operators were investigated in several works [28–31] but no clear resolution for the anomalies was found apart from reaching a consensus that the anomalies were irrelevant as long as the classical field quantities and the commutation relations of the corresponding field operators were well defined. Since then, in the studies of electromagnetic fields inside dielectric media, IOF has mainly been applied in calculating the classical field quantities. Only recently it has been suggested that, despite the early interpretations, the ladder operators and their commutation relations might in fact relate to experimentally measurable physical properties [32, 33]. Such a property is for example the threshold for the second harmonic generation when it occurs inside microcavities [32, 33]. The commutation relation anomalies also lead to other problems. For example, the photon number is a useful concept in thermodynamics, but due to the commutation relation anomalies, it has been difficult to consistently define the photon number in resonant structures and in non-equilibrium conditions.

Due to the very precise explanation of a large set of phenomena in electrodynamics, Maxwell's equations are often thought to provide a complete picture on classical electrodynamics. However, surprisingly the understanding of the theory of classical electromagnetic fields can still be seen as somewhat incomplete since there have been remaining significant controversies even in certain simple questions. For example, the form of the momentum of light in transparent materials has remained as an extensive scientific controversy for more than a century [34–46]. This controversy is known as the Abraham–Minkowski dilemma, where there exist two rivaling forms for the photon momentum in a medium. The angular momentum of light forms another challenging topic that has allowed new discoveries until these days [47]. The modern interest in the angular momentum of light started from the discovery of how the angular momentum of light is split into the orbital and spin related parts [48, 49].

One of the main goals of this thesis has been to increase our understanding of the relations between the classical, quantum, and semiclassical theories and to develop practical approaches that can be used to simulate the behavior of quantized electromagnetic field in materials. This is important as optical energy transfer has a key role in several fields of optical technologies related, e.g., to thin-film light-emitting diodes [50, 51],

nanoplasmonics [52–55], near-field microscopy [56, 57], metamaterials [58, 59], photonic crystals [60, 61], optical data processing [62, 63], and radiative cooling [64]. The behavior of light in microscopic systems and the related optical phenomena also naturally lead to questions on the quantum nature of light, on proper ways to quantize the electromagnetic field, and, even more importantly, on how to correctly interpret the results of various experiments. Related questions consider the wave–particle duality and the possibility to describe the propagating electromagnetic field as a flow of photons. These questions have their origin in the principle of complementarity according to which wave and particle aspects of physical objects cannot be measured at a particular moment. The photon flow picture of the electromagnetic field is known to become especially challenging in the case of resonant structures and it is also closely related to the mentioned Abraham–Minkowski controversy of the photon momentum in a medium [34–46].

The research related to classical and quantum optics of microscopic systems is strongly influenced by the availability of simple and transparent theoretical models and tools that allow in-depth understanding of the various relevant phenomena in a sufficiently simple form. Such insight has been used, for example, in the recent experimental demonstrations and theoretical investigations of noiseless but nondeterministic optical amplifiers [65–71] and in the studies of optical properties of cavities [33, 72–74]. Simple description of the quantum aspects of energy transfer is especially interesting and challenging in lossy microscopic systems often simulated by the prototypical layered structures. Due to the existing challenges, there is a growing need for transparent theoretical tools that allow modeling electromagnetic fields and related quantities in a wide range of applications, especially, including lossy systems and resonant structures.

## 1.2   Scope and objectives

This doctoral thesis project aims at developing the physical insight needed to describe quantum optical energy and momentum transfer and photon number in lossy and lossless microscopic structures. As fundamental starting points for our investigations, we use Maxwell's equations, the conventional FED, the second quantization of fields, the canonical commutation relations of field and ladder operators, and the covariance principle

of the special theory of relativity. Another goal is also to clarify our understanding of the relations between the classical, quantum, and semiclassical theories of light propagation in a medium. In particular, we focus on deriving and analyzing physical quantities that quantify energy and momentum transfer in a medium in a clear and comprehensible fashion. We also aim at bringing the insight offered by the equations towards the practical limit where they can be adapted to engineering problems.

We started the studies of this thesis by investigating the output fields of simple beam-splitter-based setups. In Publication I, we presented an experimental setup for noiseless amplification of weak coherent fields and modeled it theoretically using the conventional Wigner function formalism of quantum optics. The proposed setup differs from previously demonstrated setups [65–68] by replacing the usually used single-photon source with a quantum nondemolition (QND) measurement. The annihilation and creation operators in these kinds of beam-splitter-based setups are generally considered as independent of position and they naturally obey their canonical commutation relations in any QED description.

After studying simple beam-splitter-based setups, it became natural to investigate how the behavior of fields changes inside material structures, where the field quantities were known to become position-dependent, and where previous theoretical works using IOF had observed anomalies in the commutation relations of the ladder operators. The simplest examples of such structures are given by stratified media, which form optical cavities. In Publication II, we introduced a quantized fluctuational electrodynamics (QFED) method to determine commutation-relation-preserving photon ladder operators for the electric field part of the total electromagnetic field in arbitrary dielectric structures. The main idea was to avoid the IOF related challenges in defining the optical modes by adopting an approach, where the canonical commutation relations are combined with the spatial field modes directly following from Maxwell's equations. This starting point naturally led to unambiguous commutation relations, but also enabled to generalize the photon-number concept to arbitrary resonator structures. In Publication II, we also established a simple connection relating the electric part of the photon number to thermal balance and illustrated the results by studying the field fluctuations and photon number in stratified media.

In Publication III, we presented how to extend the previous electric

field based quantization introduced in Publication II to describe also the magnetic field and the total electromagnetic field. We showed that the photon-number parts of the electric, magnetic, and total electromagnetic fields have different position dependencies near material interfaces at non-equilibrium conditions. We also introduced the concept of frequency-dependent local field temperature that describes the equilibrium temperature of a resonant particle interacting with the electromagnetic field at a single frequency. Later, in Publication IV, we adapted a photon flow picture of the propagation of light in a medium to present how to separate the fields and photon numbers into parts propagating in different directions in interfering structures. Thus, our approach bridged QFED and the commonly used quantum optical IOF. We also introduced the concept of the interference density of states that was instrumental in the unambiguous separation of the fields and the related quantum operators into parts propagating in different directions.

In Publication V, we described how to extend QFED field quantization previously applied only to dielectric media to describe also magnetic media with nonunity permeability. This non-trivial generalization became possible by using two independent noise operators that follow from the additional degree of freedom introduced by the magnetic field–matter interactions. Then, in Publication VI, we developed the QFED formalism further to three dimensions by using the dyadic Green's functions and the three-dimensional noise-current operators. The extended description allowed studying also field components that are not normal to material interfaces in the studied layered structures. The evanescent waves and surface plasmons (SPs) were naturally included in the description via the dyadic Green's functions. We also illustrated the position-dependent effective field temperatures in a selected quantum well (QW) structure with a metallic coating supporting SPs. Then, in Publication VII, we used the propagating photon number concepts of Publication IV to derive the interference-exact radiative transfer equation (RTE), which extended the applicability of the conventional RTE [75–79] beyond its main limitation in describing interference effects. We obtained position-dependent damping and scattering coefficients that can be used to replace the conventional damping and scattering coefficients used in the RTE. These coefficients account for both the nonlocal wave and local particle features in stratified geometries providing tools to study the wave–particle duality [80].

During studying the photon number in the QFED description in several works, we started to investigate if and how the adapted photon flow description of optical fields could be applied to the centennial Abraham–Minkowski controversy of photon momentum in a medium, a puzzling problem which had been faced by the other members of the Engineered Nanosystems group in the previous studies on thermal cavities. The solution to the Abraham–Minkowski controversy would essentially increase our understanding of the momentum flow associated to the photon flow. As the QFED method was not as such found to provide sufficient tools to solve the controversy without additional assumptions on the form of the optical force density (that was a controversial topic in the previous literature [34–41]) and the related dynamics of the medium, we decided to rely our investigations on the most fundamental relations between energy and momentum, namely the conservation laws and the covariance condition of the special theory of relativity. This led us to present the foundations of a covariant theory of light in a medium and the related resolution of the Abraham–Minkowski controversy in Publication VIII. The theory was derived using two approaches: (1) The mass-polariton (MP) quasiparticle picture was based only on the fundamental conservation laws of nature and the special theory of relativity. (2) The electrodynamics of continuous media and the continuum mechanics were coupled to form an optoelastic continuum dynamics (OCD) theory of light in a medium. Our solution of the Abraham–Minkowski controversy shows that the light wave propagating in a medium must be described by using MP quasiparticles, coupled states of the field and matter. We also introduced the concept of a light associated mass density wave (MDW) and predicted the photon mass drag effect displacing the medium along the photon flow. We also showed that the photon mass drag effect must lead to dissipation of photon energy when the photon propagates through transparent materials.

## 1.3   Organization of this thesis

This thesis is organized as follows: Chapter 2 reviews the theoretical background for the investigations of this thesis. It covers the essential parts from both the classical and quantum theories of electromagnetic fields and the dynamics of field–matter interaction. Chapter 3 presents the new models developed in this thesis. In particular, it covers the QFED

formalism developed in Publications II–VII and the MP and OCD models of energy and momentum transfer in a medium developed in Publication VIII. Chapter 4 presents selected results obtained by applying the conventional models and developed tools to example structures. The results of Publication I are discussed in Sec. 4.1, the results of Publications II–VII are reviewed in Sec. 4.2, and the results of Publication VIII are discussed in Sec. 4.3. Chapter 5 concludes the dissertation with a summary and discussion of the obtained main results and future challenges.

# 2. Theoretical background

This chapter covers the theoretical background of electromagnetic fields and the dynamics of field–matter interaction applied in this thesis. In Sec. 2.1, we review the classical theory of electromagnetic fields based on Maxwell's equations. We also cover the solution of electromagnetic fields in terms of Green's functions and discuss the framework of FED. The covariance principle of the special theory of relativity is also described as, in this thesis, we also directly apply this fundamental principle to describe the coupled dynamics of the field and matter. Section 2.2 covers the quantum theory. It first reviews the foundation, which is formed by the second quantization and the canonical commutation relations of fields and ladder operators. Then it describes the quantum optical IOF used to calculate possible output fields of a setup when the input fields are known. It also covers the position-dependent NOF and the Wigner function formalism commonly used to model quantum optical experiments.

## 2.1 Classical theory

This section reviews the classical theory of electromagnetic fields in a medium, which lays the foundation for the studies of this thesis. In Sec. 2.1.1, we start the review with the frequency space Maxwell's equations in linear and isotropic media since, in this thesis, all media are assumed to be piecewise linear and isotropic. This is followed by presenting the solution of classical electric and magnetic fields in a medium using the Green's function approach in Sec. 2.1.2. The Green's function approach also forms the basis for the solution of the fields in the classical FED formalism presented in Sec. 2.1.3. The covariance principle of the special theory of relativity is described in Sec. 2.1.4.

## 2.1.1 Maxwell's equations

In classical electrodynamics, the behavior of the electromagnetic field is completely described by Maxwell's equations. In the macroscopic form, Maxwell's equations relate the electric field strength $\mathbf{E}$, the magnetic field strength $\mathbf{H}$, the electric flux density $\mathbf{D}$, and the magnetic flux density $\mathbf{B}$ to the free electric charge density $\rho_\mathrm{f}$ and the current density $\mathbf{J}_\mathrm{f}$ as [81]

$$\nabla \times \mathbf{E}(\mathbf{r}, t) = -\frac{\partial \mathbf{B}(\mathbf{r}, t)}{\partial t}, \tag{2.1}$$

$$\nabla \times \mathbf{H}(\mathbf{r}, t) = \mathbf{J}_\mathrm{f}(\mathbf{r}, t) + \frac{\partial \mathbf{D}(\mathbf{r}, t)}{\partial t}, \tag{2.2}$$

$$\nabla \cdot \mathbf{D}(\mathbf{r}, t) = \rho_\mathrm{f}(\mathbf{r}, t), \tag{2.3}$$

$$\nabla \cdot \mathbf{B}(\mathbf{r}, t) = 0. \tag{2.4}$$

It is convenient to represent the fields in Maxwell's equations in terms of their Fourier transforms written, e.g., for the electric field as

$$\mathbf{E}(\mathbf{r}, t) = \int_0^\infty \mathbf{E}(\mathbf{r}, \omega) e^{-i\omega t} d\omega + c.c., \tag{2.5}$$

where $\mathbf{E}(\mathbf{r}, \omega)$ describes the time-harmonic component of the electric field at angular frequency $\omega$ and $c.c.$ denotes the complex conjugate of the first term. Similar relations apply also for the fields $\mathbf{D}$, $\mathbf{H}$, $\mathbf{B}$ and sources $\rho_\mathrm{f}$ and $\mathbf{J}_\mathrm{f}$. Note that, throughout this thesis, we use the same symbols for the fields and their frequency components and specify the meaning with the function arguments.

By applying the time harmonic field components defined in Eq. (2.5), Maxwell's equations (2.1)–(2.4) read [81]

$$\nabla \times \mathbf{E}(\mathbf{r}, \omega) = i\omega \mathbf{B}(\mathbf{r}, \omega), \tag{2.6}$$

$$\nabla \times \mathbf{H}(\mathbf{r}, \omega) = \mathbf{J}_\mathrm{f}(\mathbf{r}, \omega) - i\omega \mathbf{D}(\mathbf{r}, \omega), \tag{2.7}$$

$$\nabla \cdot \mathbf{D}(\mathbf{r}, \omega) = \rho_\mathrm{f}(\mathbf{r}, \omega), \tag{2.8}$$

$$\nabla \cdot \mathbf{B}(\mathbf{r}, \omega) = 0. \tag{2.9}$$

Under the conditions of an approximatively linear and isotropic medium used in this thesis, the fields and field densities are related by the constitutive relations [82]

$$\mathbf{D}(\mathbf{r}, \omega) = \varepsilon_0 \varepsilon(\mathbf{r}, \omega) \mathbf{E}(\mathbf{r}, \omega) + \delta \mathbf{P}(\mathbf{r}, \omega), \tag{2.10}$$

$$\mathbf{B}(\mathbf{r}, \omega) = \mu_0 \mu(\mathbf{r}, \omega) \mathbf{H}(\mathbf{r}, \omega) + \mu_0 \delta \mathbf{M}(\mathbf{r}, \omega), \tag{2.11}$$

where $\varepsilon_0$ and $\mu_0$ are the permittivity and permeability of vacuum, $\varepsilon(\mathbf{r}, \omega) = \varepsilon_{\mathrm{r}}(\mathbf{r}, \omega) + i\varepsilon_{\mathrm{i}}(\mathbf{r}, \omega)$ and $\mu(\mathbf{r}, \omega) = \mu_{\mathrm{r}}(\mathbf{r}, \omega) + i\mu_{\mathrm{i}}(\mathbf{r}, \omega)$ are the relative permittivity and permeability of the medium with real and imaginary parts denoted by subscripts r and i, and $\delta\mathbf{P}$ and $\delta\mathbf{M}$ are the polarization and magnetization fields that are not linearly proportional to the respective electric and magnetic field strengths [82, 83]. In the context of this thesis, $\delta\mathbf{P}$ and $\delta\mathbf{M}$ describe small noise related parts in the linear polarization and magnetization fields as customary in the classical FED [84].

### 2.1.2 Solution of fields using Green's functions

From Maxwell's equations for time-harmonic field components in Eqs. (2.6)–(2.9) and the constitutive relations in Eqs. (2.10) and (2.11), it follows that the electric field obeys the well-known equation [26]

$$\nabla \times \left[ \frac{\nabla \times \mathbf{E}(\mathbf{r}, \omega)}{\mu_0 \mu(\mathbf{r}, \omega)} \right] - \omega^2 \varepsilon_0 \varepsilon(\mathbf{r}, \omega) \mathbf{E}(\mathbf{r}, \omega) = i\omega \mathbf{J}_{\mathrm{e}}(\mathbf{r}, \omega) - \nabla \times \left[ \frac{\mathbf{J}_{\mathrm{m}}(\mathbf{r}, \omega)}{\mu_0 \mu(\mathbf{r}, \omega)} \right], \quad (2.12)$$

where $\mathbf{J}_{\mathrm{e}}(\mathbf{r}, \omega) = \mathbf{J}_{\mathrm{f}}(\mathbf{r}, \omega) - i\omega\delta\mathbf{P}(\mathbf{r}, \omega)$ and $\mathbf{J}_{\mathrm{m}}(\mathbf{r}, \omega) = -i\omega\mu_0\delta\mathbf{M}(\mathbf{r}, \omega)$ represent the polarization and magnetization noise currents that act as field sources in the classical FED [85, 86]. The electric noise-current term $\mathbf{J}_{\mathrm{e}}(\mathbf{r}, \omega)$ includes contributions from both the electric currents due to free charges, which amount to zero for insulating dielectrics, as well as polarization terms associated with dipole currents and thermal dipole fluctuations. The magnetic noise-current term $\mathbf{J}_{\mathrm{m}}(\mathbf{r}, \omega)$ acts as a separate field source arising from the magnetic dipole fluctuations.

The dyadic Green's functions are used to make the presentation of the solution of electromagnetic problems compact [82, 87]. In short, in the dyadic notation, the solutions of fields for three independent dipoles oriented along different coordinate axes are collected into a single dyadic, which can be presented as a matrix [88]. Formally dyadic Green's functions are solutions of vector form differential equations for delta function sources. For the delta function source term $\overset{\leftrightarrow}{\mathbf{I}}\delta(\mathbf{r} - \mathbf{r}')$, where $\overset{\leftrightarrow}{\mathbf{I}}$ is the unit dyadic and $\delta(\mathbf{r} - \mathbf{r}')$ is the Dirac delta function, an equation for the Green's function of Eq. (2.12) is written as [26, 89]

$$\nabla_{\mathbf{r}} \times \left[ \frac{\nabla_{\mathbf{r}} \times \overset{\leftrightarrow}{\mathbf{G}}_{\mathrm{ee}}(\mathbf{r}, \omega, \mathbf{r}')}{\mu(\mathbf{r}, \omega)} \right] - k_0^2 \varepsilon(\mathbf{r}, \omega) \overset{\leftrightarrow}{\mathbf{G}}_{\mathrm{ee}}(\mathbf{r}, \omega, \mathbf{r}') = \overset{\leftrightarrow}{\mathbf{I}}\delta(\mathbf{r} - \mathbf{r}'). \quad (2.13)$$

Here $k_0 = \omega/c$ is the wavenumber in vacuum with the vacuum velocity of light $c$ and $\nabla_{\mathbf{r}}$ is the vector differential operator $\nabla$ with respect to $\mathbf{r}$. In terms of the electric Green's function $\overset{\leftrightarrow}{\mathbf{G}}_{\mathrm{ee}}(\mathbf{r}, \omega, \mathbf{r}')$, the solution of Eq. (2.12)

is then written by integrating the product of the Green's function and the source terms over all the source points $\mathbf{r}'$ as

$$
\begin{aligned}
&\mathbf{E}(\mathbf{r}, \omega)\\
&= \mu_0 \int \overset{\leftrightarrow}{\mathbf{G}}_{\mathrm{ee}}(\mathbf{r}, \omega, \mathbf{r}') \cdot \left\{ i\omega \mathbf{J}_{\mathrm{e}}(\mathbf{r}', \omega) - \nabla_{\mathbf{r}'} \times \left[ \frac{\mathbf{J}_{\mathrm{m}}(\mathbf{r}', \omega)}{\mu_0 \mu(\mathbf{r}', \omega)} \right] \right\} d^3 r'\\
&= i\omega\mu_0 \int \overset{\leftrightarrow}{\mathbf{G}}_{\mathrm{ee}}(\mathbf{r}, \omega, \mathbf{r}') \cdot \mathbf{J}_{\mathrm{e}}(\mathbf{r}', \omega) d^3 r' + k_0 \int \overset{\leftrightarrow}{\mathbf{G}}_{\mathrm{em}}(\mathbf{r}, \omega, \mathbf{r}') \cdot \mathbf{J}_{\mathrm{m}}(\mathbf{r}', \omega) d^3 r'.
\end{aligned}
$$
(2.14)

In the case of the second term in (2.14), we have applied Stokes' theorem, which results in the integration by parts formula $\int_V \mathbf{G}^j \cdot (\nabla_{\mathbf{r}'} \times \mathbf{J}) d^3 r' = \int_V (\nabla_{\mathbf{r}'} \times \mathbf{G}^j) \cdot \mathbf{J} d^3 r' - \int_{\partial V} (\mathbf{G}^j \times \mathbf{J}) \cdot d\mathbf{S}'$ for each row vector $\mathbf{G}^j$ of the matrix representation of $\overset{\leftrightarrow}{\mathbf{G}}_{\mathrm{ee}}(\mathbf{r}, \omega, \mathbf{r}')$. As the boundary condition, the Green's functions are assumed to go to zero when the separation between the field point $\mathbf{r}$ and the source point $\mathbf{r}'$ tends to infinity. Using the shorthand notation $\overset{\leftrightarrow}{\mathbf{G}}(\mathbf{r}, \omega, \mathbf{r}') \times \overset{\leftarrow}{\nabla}_{\mathbf{r}'} = -[\nabla_{\mathbf{r}'} \times \mathbf{G}^1, \nabla_{\mathbf{r}'} \times \mathbf{G}^2, \nabla_{\mathbf{r}'} \times \mathbf{G}^3]^T$ adopted from Ref. [26], where $T$ denotes transpose, we have then defined the exchange Green's function $\overset{\leftrightarrow}{\mathbf{G}}_{\mathrm{em}}(\mathbf{r}, \omega, \mathbf{r}')$ in the last step in (2.14) as

$$
\overset{\leftrightarrow}{\mathbf{G}}_{\mathrm{em}}(\mathbf{r}, \omega, \mathbf{r}') = \frac{\overset{\leftrightarrow}{\mathbf{G}}_{\mathrm{ee}}(\mathbf{r}, \omega, \mathbf{r}') \times \overset{\leftarrow}{\nabla}_{\mathbf{r}'}}{k_0 \mu(\mathbf{r}', \omega)}.
$$
(2.15)

After solving for the electric field, the magnetic field can be solved by using Faraday's law in Eq. (2.6) and the constitutive relation in Eq. (2.11) resulting in

$$
\begin{aligned}
&\mathbf{H}(\mathbf{r}, \omega)\\
&= \frac{1}{i\omega\mu_0 \mu(\mathbf{r}, \omega)} \left[ \mathbf{J}_{\mathrm{m}}(\mathbf{r}, \omega) + \nabla_{\mathbf{r}} \times \mathbf{E}(\mathbf{r}, \omega) \right]\\
&= k_0 \int \frac{\nabla_{\mathbf{r}} \times \overset{\leftrightarrow}{\mathbf{G}}_{\mathrm{ee}}(\mathbf{r}, \omega, \mathbf{r}')}{k_0 \mu(\mathbf{r}, \omega)} \cdot \mathbf{J}_{\mathrm{e}}(\mathbf{r}', \omega) d^3 r'\\
&\quad - \frac{i k_0^2}{\omega\mu_0} \int \left[ \frac{\nabla_{\mathbf{r}} \times \overset{\leftrightarrow}{\mathbf{G}}_{\mathrm{em}}(\mathbf{r}, \omega, \mathbf{r}')}{k_0 \mu(\mathbf{r}, \omega)} + \overset{\leftrightarrow}{\mathbf{I}} \frac{\delta(\mathbf{r} - \mathbf{r}')}{k_0^2 \mu(\mathbf{r}, \omega)} \right] \cdot \mathbf{J}_{\mathrm{m}}(\mathbf{r}', \omega) d^3 r'\\
&= k_0 \int \overset{\leftrightarrow}{\mathbf{G}}_{\mathrm{me}}(\mathbf{r}, \omega, \mathbf{r}') \cdot \mathbf{J}_{\mathrm{e}}(\mathbf{r}', \omega) d^3 r' + i\omega\varepsilon_0 \int \overset{\leftrightarrow}{\mathbf{G}}_{\mathrm{mm}}(\mathbf{r}, \omega, \mathbf{r}') \cdot \mathbf{J}_{\mathrm{m}}(\mathbf{r}', \omega) d^3 r'.
\end{aligned}
$$
(2.16)

Here we have first substituted the expression for $\mathbf{E}(\mathbf{r}, \omega)$ in terms of the Green's functions given in Eq. (2.14) and incorporated the separate source term $\mathbf{J}_{\mathrm{m}}(\mathbf{r}, \omega)$ into the integral using a suitable delta function presentation and, in the last step, defined the exchange Green's function $\overset{\leftrightarrow}{\mathbf{G}}_{\mathrm{me}}(\mathbf{r}, \omega, \mathbf{r}')$ and the magnetic Green's function $\overset{\leftrightarrow}{\mathbf{G}}_{\mathrm{mm}}(\mathbf{r}, \omega, \mathbf{r}')$ as

$$
\overset{\leftrightarrow}{\mathbf{G}}_{\mathrm{me}}(\mathbf{r}, \omega, \mathbf{r}') = \frac{\nabla_{\mathbf{r}} \times \overset{\leftrightarrow}{\mathbf{G}}_{\mathrm{ee}}(\mathbf{r}, \omega, \mathbf{r}')}{k_0 \mu(\mathbf{r}, \omega)},
$$
(2.17)

$$\overset{\leftrightarrow}{\mathbf{G}}_{\mathrm{mm}}(\mathbf{r},\omega,\mathbf{r}') = -\frac{\nabla_{\mathbf{r}} \times \overset{\leftrightarrow}{\mathbf{G}}_{\mathrm{em}}(\mathbf{r},\omega,\mathbf{r}')}{k_0 \mu(\mathbf{r},\omega)} - \overset{\leftrightarrow}{\mathbf{I}} \frac{\delta(\mathbf{r}-\mathbf{r}')}{k_0^2 \mu(\mathbf{r},\omega)}. \qquad (2.18)$$

By using Eqs. (2.15) and (2.18), we also obtain an expression of the magnetic Green's function $\overset{\leftrightarrow}{\mathbf{G}}_{\mathrm{mm}}(\mathbf{r},\omega,\mathbf{r}')$ directly in terms of the electric Green's function $\overset{\leftrightarrow}{\mathbf{G}}_{\mathrm{ee}}(\mathbf{r},\omega,\mathbf{r}')$ as

$$\overset{\leftrightarrow}{\mathbf{G}}_{\mathrm{mm}}(\mathbf{r},\omega,\mathbf{r}') = -\frac{\nabla_{\mathbf{r}} \times [\overset{\leftrightarrow}{\mathbf{G}}_{\mathrm{ee}}(\mathbf{r},\omega,\mathbf{r}') \times \overset{\leftarrow}{\nabla}_{\mathbf{r}'}]}{k_0^2 \mu(\mathbf{r},\omega)\mu(\mathbf{r}',\omega)} - \overset{\leftrightarrow}{\mathbf{I}} \frac{\delta(\mathbf{r}-\mathbf{r}')}{k_0^2 \mu(\mathbf{r},\omega)}. \qquad (2.19)$$

Even though many problems may be solved without using dyadic Green's functions, the symbolic simplicity offered by them makes the use of dyadic Green's functions attractive once one is familiar with the dyadic notation. This is especially true in complex scattering problems, in which the physics related to the electromagnetic vector field is compactly accounted for using the dyadic Green's functions.

### 2.1.3 Fluctuational electrodynamics

In FED, the studied objects are considered to be close to equilibrium, and the non-equilibrium behavior is described by using linear response theory. In this regime, the fluctuation–dissipation theorem (FDT) relates the rate of energy dissipation in a non-equilibrium system to the fluctuations that occur spontaneously in equilibrium systems. For example, if a system is placed in a state that is slightly out of thermal equilibrium, e.g., by a mechanical force acting on the system, then the system will relax back to the initial state of thermal equilibrium. In the relaxation process, the energy of the small perturbation is dissipated to heat on a characteristic time scale that is related to the thermal fluctuations of the system in thermal equilibrium. Therefore, a statistical fluctuation in thermal equilibrium is indistinguishable from a small mechanical perturbation that puts the system out of equilibrium.

The FDT is also needed for the understanding of fluctuating fields near microscopic objects and optical interactions at small distances. Typically, the FDT for the polarization current density in a dielectric medium is written in the frequency domain as [84, 90]

$$\langle J_{\mathrm{e},j}(\mathbf{r},\omega)J_{\mathrm{e},k}^*(\mathbf{r}',\omega') \rangle = 4\pi\omega\varepsilon_0\varepsilon_{\mathrm{i}}(\mathbf{r},\omega)\Theta(\omega,T)\delta_{jk}\delta(\mathbf{r}-\mathbf{r}')\delta(\omega-\omega'), \quad (2.20)$$

where $j,k \in \{x,y,z\}$, the brackets denote the expectation value, and $\Theta(\omega,T) = \hbar\omega/2 + \hbar\omega/(e^{\hbar\omega/(k_{\mathrm{B}}T)}-1)$, where $\hbar$ is the reduced Planck constant

and $k_{\mathrm{B}}$ is Boltzmann's constant, is the average energy of the quantum harmonic oscillator in thermal equilibrium at an angular frequency $\omega$ and at temperature $T$. The Dirac delta functions $\delta(\mathbf{r} - \mathbf{r}')$ and $\delta(\omega - \omega')$ are present due to the spatial and temporal locality of the dielectric constant and the Kronecker symbol $\delta_{jk}$ accounts for the assumption of isotropic media [91]. The term $\hbar\omega/2$ in the average energy of the quantum harmonic oscillator corresponds to the zero-point energy and it is often neglected as it is compensated by the surrounding of the body [14].

The FDT can also be applied to derive the fields radiated by a system with an inhomogeneous temperature distribution [84, 86]. Although the mean values of the fields are zero, their correlations corresponding to power densities are non-zero. For example, by using the FDT, the electric field solution in terms of the Green's function in Eq. (2.14), and neglecting the magnetization current fluctuations by setting $\mathbf{J}_{\mathrm{m}}(\mathbf{r}', \omega) = 0$, which applies to a dielectric medium, the symmetrized cross-spectral correlation function of the electric field is given by [84]

$$\langle E_j(\mathbf{r}, \omega) E_k^*(\mathbf{r}', \omega') \rangle = \frac{4\pi\omega^3}{c^4\varepsilon_0} \delta(\omega - \omega') \sum_l \int \varepsilon_{\mathrm{i}}(\mathbf{r}'', \omega) \Theta\big(\omega, T(\mathbf{r}'')\big)$$
$$\times\, G_{\mathrm{ee},jl}(\mathbf{r}, \omega, \mathbf{r}'') G_{\mathrm{ee},kl}^*(\mathbf{r}', \omega, \mathbf{r}'') d^3 r'', \qquad (2.21)$$

where $T(\mathbf{r}'')$ is the pointwise defined local temperature of the medium.

In addition to the electric field correlations, with the help of the FDT, it is also possible to calculate magnetic field correlations, the total electromagnetic energy density, energy flow described by the Poynting vector, and Maxwell's stress tensor [84]. In addition, it is possible to define the electric and magnetic local densities of states (LDOSs) [85, 92, 93]. Since the initiation of the theory, FED has been widely applied in the studies of field fluctuations, radiative energy transfer, and Casimir forces [86]. However, FED has not been previously used in the context of fully quantizing the electromagnetic field using position-dependent photon numbers and commutation-relation-preserving ladder operators. Together with the quantum-optical input–output formalism discussed in the following subsection, FED provides a solid background for the investigations of the position-dependent photon-number concept developed in this thesis.

### 2.1.4 Covariance principle

In the studies of the momentum of light in a medium in Publication VIII, we have taken the covariance principle of the special theory of relativity as one of the main starting points. The covariance principle essentially states that the laws of physics are the same for all inertial observers. In other words, the formulation of physical laws using certain physical quantities measured in different frames of reference can be unambiguously correlated via Lorentz transformations. The Lorentz transformation of the energy-momentum four-vector of a particle $(E, p_x c, p_y c, p_z c)$, where $E$ is energy and $p_x$, $p_y$, and $p_z$ are the $x$, $y$, and $z$ components of the momentum, is written in the case of motion in $x$ direction as [94]

$$E' = \gamma(E - vp_x), \tag{2.22}$$

$$p'_x c = \gamma(p_x c - vE/c), \tag{2.23}$$

$$p'_y c = p_y c, \tag{2.24}$$

$$p'_z c = p_z c. \tag{2.25}$$

Here $\gamma = 1/\sqrt{1 - v^2/c^2}$ is the Lorentz factor and primed quantities denote the quantities in the transformed reference frame.

A scalar quantity that is Lorentz invariant is the Minkowski inner product of the energy-momentum four-vector with itself. This covariance condition, which is also known as the relativistic energy-momentum relation, is given by [94]

$$E^2 - (pc)^2 = (m_0 c^2)^2, \tag{2.26}$$

where $p$ is the total momentum and $m_0$ is the rest mass of the particle. In the studies of this thesis in Publication VIII, we have shown that the conventional Abraham and Minkowski models of light in a medium do not satisfy the covariance principle in Eq. (2.26) due to the assumption that there is not any rest mass propagating with a light pulse in a medium. As these earlier formulations of the theory had failed to lead to a covariant description, in Publication VIII it became natural to consider a possibility that the light pulse is actually a coupled state of the field and matter with a small but finite rest mass. This will be described in more detail in Sec. 3.2.

## 2.2 Quantum theory

This section covers the conventional quantum theory of the electromagnetic field. Its foundation is provided by the second quantization that we briefly review in Sec. 2.2.1. Then, in Sec. 2.2.2, we describe the quantum optical IOF and the canonical commutation relations of fields and photon ladder operators. The noise source operators in NOF are presented in Sec. 2.2.3. To allow practical modeling of quantum noise in the output fields in beam splitter experiments, in Sec. 2.2.4, we also briefly review the Wigner function formalism, the related beam splitter description, and common quantum states of light.

### 2.2.1 Second quantization

In QED, like in other quantum field theories, the fields are presented as field operators, in a manner similar to how the physical quantities, such as position and momentum, are treated as operators in the conventional quantum mechanics. This method is called the second quantization or the canonical field quantization. The main underlying ideas of the second quantization were introduced by Paul Dirac in 1927 [3], and they were developed forward by many physicists, most notably, by Fock [95] and Jordan [96]. The formalism of the second quantization introduces the creation and annihilation operators that provide useful tools to the study of the quantum many-body problems. The creation operator $\hat{a}_{\mathbf{k}}^{\dagger}$ creates and the annihilation operator $\hat{a}_{\mathbf{k}}$ annihilates a photon with energy $\hbar\omega_{\mathbf{k}}$ in the electromagnetic field mode with wave vector $\mathbf{k}$. The canonical commutation relations of the creation and annihilation operators are given by [97]

$$[\hat{a}_{\mathbf{k}}, \hat{a}_{\mathbf{k'}}] = [\hat{a}_{\mathbf{k}}^{\dagger}, \hat{a}_{\mathbf{k'}}^{\dagger}] = 0,$$
$$[\hat{a}_{\mathbf{k}}, \hat{a}_{\mathbf{k'}}^{\dagger}] = \delta_{\mathbf{kk'}}. \tag{2.27}$$

In the second quantization with the Coulomb gauge $\nabla \cdot \hat{\mathbf{A}}(\mathbf{r}, t) = 0$, the vector potential operator $\hat{\mathbf{A}}(\mathbf{r}, t)$, the electric field operator $\hat{\mathbf{E}}(\mathbf{r}, t) = -\partial\hat{\mathbf{A}}(\mathbf{r}, t)/\partial t$, and the magnetic field operator $\hat{\mathbf{B}}(\mathbf{r}, t) = \nabla \times \hat{\mathbf{A}}(\mathbf{r}, t)$ at each point in free space are given in terms of the creation and annihilation operators as [98]

$$\hat{\mathbf{A}}(\mathbf{r}, t) = \sum_{\mathbf{k}} \sqrt{\frac{\hbar}{2\varepsilon_0 V \omega_{\mathbf{k}}}} \hat{\mathbf{e}}_{\mathbf{k}} (\hat{a}_{\mathbf{k}} e^{i\mathbf{k}\cdot\mathbf{r} - i\omega_{\mathbf{k}}t} + \hat{a}_{\mathbf{k}}^{\dagger} e^{-i\mathbf{k}\cdot\mathbf{r} + i\omega_{\mathbf{k}}t}), \tag{2.28}$$

$$\hat{\mathbf{E}}(\mathbf{r},t) = \sum_{\mathbf{k}} i\sqrt{\frac{\hbar\omega_{\mathbf{k}}}{2\varepsilon_0 V}}\hat{\mathbf{e}}_{\mathbf{k}}(\hat{a}_{\mathbf{k}}e^{i\mathbf{k}\cdot\mathbf{r}-i\omega_{\mathbf{k}}t} - \hat{a}_{\mathbf{k}}^{\dagger}e^{-i\mathbf{k}\cdot\mathbf{r}+i\omega_{\mathbf{k}}t}), \tag{2.29}$$

$$\hat{\mathbf{B}}(\mathbf{r},t) = \sum_{\mathbf{k}} i\sqrt{\frac{\hbar}{2\varepsilon_0 V\omega_{\mathbf{k}}}}\mathbf{k}\times\hat{\mathbf{e}}_{\mathbf{k}}(\hat{a}_{\mathbf{k}}e^{i\mathbf{k}\cdot\mathbf{r}-i\omega_{\mathbf{k}}t} - \hat{a}_{\mathbf{k}}^{\dagger}e^{-i\mathbf{k}\cdot\mathbf{r}+i\omega_{\mathbf{k}}t}). \tag{2.30}$$

Here $\hat{\mathbf{e}}_{\mathbf{k}}$ is the polarization unit vector of mode $\mathbf{k}$ and $V$ is the quantization volume. In the expressions in Eqs. (2.28)–(2.30), the first terms are the positive frequency parts conventionally denoted by $\hat{\mathbf{A}}^+(\mathbf{r},t)$, $\hat{\mathbf{E}}^+(\mathbf{r},t)$, and $\hat{\mathbf{B}}^+(\mathbf{r},t)$ [98]. The second terms, which are Hermitian conjugates of the first terms, are the negative frequency parts denoted by $\hat{\mathbf{A}}^-(\mathbf{r},t)$, $\hat{\mathbf{E}}^-(\mathbf{r},t)$, and $\hat{\mathbf{B}}^-(\mathbf{r},t)$. In the case of a continuum of modes, it is convenient to convert the summation over $\mathbf{k}$ to an integration by using the general substitution relation $\sum_{\mathbf{k}} \rightarrow [V/(2\pi)^3]\int d^3k$ [98].

As the ladder operators, also the field operators in Eqs. (2.28)–(2.30) obey certain commutation relations. For example, from commutation relations of the ladder operators in Eq. (2.27) and from the expressions of the vector potential and electric field operators in Eqs. (2.28) and (2.29), it follows that the vector potential and electric field operators obey the canonical commutation relation given by [98, 99]

$$[\hat{A}_j(\mathbf{r},t), -\varepsilon_0\hat{E}_l(\mathbf{r}',t)] = i\hbar\delta_{\mathrm{T}_{jl}}(\mathbf{r}-\mathbf{r}'). \tag{2.31}$$

Here $\delta_{\mathrm{T}_{jl}}(\mathbf{r}-\mathbf{r}')$ is the transverse delta function, which is an operator that maps a vector field to its transverse component defined as a part whose divergence is zero [98]. The transverse delta function is explicitly written as [98]

$$\delta_{\mathrm{T}_{jl}}(\mathbf{r}-\mathbf{r}') = \frac{1}{(2\pi)^3}\int\left(\delta_{jl} - \frac{k_j k_l}{k^2}\right)e^{i\mathbf{k}\cdot(\mathbf{r}-\mathbf{r}')}d^3k. \tag{2.32}$$

### 2.2.2 Quantum optical input–output formalism

The quantum optical IOF can be introduced by studying the input and output fields of a beam splitter, which is one of the simplest optical devices. In a beam splitter, two incident beams may interfere to produce two emerging beams. On dielectric interfaces of a beam splitter, it is also possible to split one incident beam into two beams as a part of the field is reflected while another part is transmitted. An ideal beam splitter is reversible and lossless. An illustration of a beam splitter is represented in Fig. 2.1.
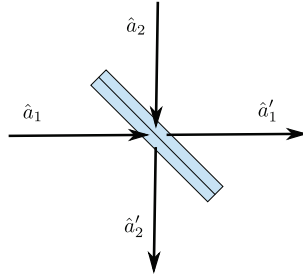
**Figure 2.1.** Beam splitter. Two incident beams are represented by mode operators $\hat{a}_1$ and $\hat{a}_2$, and the emerging beams by mode operators $\hat{a}_1'$ and $\hat{a}_2'$.

In the Heisenberg picture, the annihilation operators of the incident fields transform as [16]

$$\begin{pmatrix} \hat{a}_1' \\ \hat{a}_2' \end{pmatrix} = \mathbf{S}_{\mathrm{BS}} \begin{pmatrix} \hat{a}_1 \\ \hat{a}_2 \end{pmatrix}, \qquad \mathbf{S}_{\mathrm{BS}} = \begin{pmatrix} t_1 & r_2 \\ r_1 & t_2 \end{pmatrix}, \qquad (2.33)$$

where $t_1$, $t_2$, $r_1$, and $r_2$ are the transmission and reflection coefficients for the corresponding beams. In general, they are complex numbers resulting in a unitary scattering matrix $\mathbf{S}_{\mathrm{BS}}$ that preserves the bosonic commutation relations between the mode operators. The matrix elements must obey the relations

$$|r_1| = |r_2|, \qquad |t_1| = |t_2|, \qquad |r_1|^2 + |t_1|^2 = 1, \qquad r_2^* t_1 + r_1 t_2^* = 0. \quad (2.34)$$

Due to the linearity, the beam splitter scattering matrix $\mathbf{S}_{\mathrm{BS}}$ can also be used to obtain the vector potential, electric field, and magnetic field operators of the output fields, when the input field operators are known to be of the form in Eqs. (2.28)–(2.30).

In the description of a single beam splitter, we do not encounter any problems with the canonical commutation relations of the ladder operators as the commutation relations are preserved by the unitary scattering matrix $\mathbf{S}_{\mathrm{BS}}$. The same is also true in the case of two beam splitters if neither of the output fields of the second beam splitter is directed back to the first beam splitter, i.e., there does not exist back coupling between the beam splitters or self-interference of the fields. However, if an output field of the second beam splitter is directed back to the first beam splitter resulting in feedback, then the above description leads to anomalies in the commutation relations of the ladder operators [27]. The origin of the anomalies has previously been identified as self-interference of the mode whose coherence length is longer than the distance between the

beam splitters [27]. However, as we have shown in Publications II and IV and as discussed in Sec. 3.1, we can completely resolve the anomalies by adapting a different approach, which results in meaningful ladder operators and the related photon-number concept also in resonant structures.

### 2.2.3 Noise operator formalism

In the conventional NOF, as a starting point for the field quantization, one uses an approach where the field quantities in the classical equations of Secs. 2.1.1 and 2.1.2 are replaced by corresponding quantum operators [24, 26]. The relations of the electric and magnetic field operators $\hat{\mathbf{E}}^+(\mathbf{r}, \omega)$ and $\hat{\mathbf{H}}^+(\mathbf{r}, \omega)$ to the polarization and magnetization noise-current operators $\hat{\mathbf{J}}_e^+(\mathbf{r}, \omega)$ and $\hat{\mathbf{J}}_m^+(\mathbf{r}, \omega)$ are given by the classical forms in Eqs. (2.14) and (2.16). The forms of the polarization and magnetization noise-current operators $\hat{\mathbf{J}}_e^+(\mathbf{r}, \omega)$ and $\hat{\mathbf{J}}_m^+(\mathbf{r}, \omega)$ are then determined by requiring that the resulting electric field and vector potential operators obey the well-known canonical commutation relation in Eq. (2.31). As a result, the operators $\hat{\mathbf{J}}_e^+(\mathbf{r}, \omega)$ and $\hat{\mathbf{J}}_m^+(\mathbf{r}, \omega)$ are written in terms of the bosonic source-field operators $\hat{f}_e(\mathbf{r}, \omega)$ and $\hat{f}_m(\mathbf{r}, \omega)$ and normalization factors $j_{0,e}(\mathbf{r}, \omega)$ and $j_{0,m}(\mathbf{r}, \omega)$ as

$$\hat{\mathbf{J}}_e^+(\mathbf{r}, \omega) = \sum_l j_{0,e}(\mathbf{r}, \omega) \hat{\mathbf{e}}_l \hat{f}_e(\mathbf{r}, \omega), \qquad (2.35)$$

$$\hat{\mathbf{J}}_m^+(\mathbf{r}, \omega) = \sum_l j_{0,m}(\mathbf{r}, \omega) \hat{\mathbf{e}}_l \hat{f}_m(\mathbf{r}, \omega), \qquad (2.36)$$

where the index $l$ ranges over the three independent coordinate directions. The bosonic source-field operators $\hat{f}_e(\mathbf{r}, \omega)$ and $\hat{f}_m(\mathbf{r}, \omega)$ obey the canonical commutation relations

$$[\hat{f}_j(\mathbf{r}, \omega), \hat{f}_k(\mathbf{r}', \omega')] = [\hat{f}_j^\dagger(\mathbf{r}, \omega), \hat{f}_k^\dagger(\mathbf{r}', \omega')] = 0,$$
$$[\hat{f}_j(\mathbf{r}, \omega), \hat{f}_k^\dagger(\mathbf{r}', \omega')] = \delta_{jk} \delta(\mathbf{r} - \mathbf{r}') \delta(\omega - \omega'), \qquad (2.37)$$

where $j, k \in \{e, m\}$. These relations clearly resemble the commutation relations of the free-space photon ladder operators in Eq. (2.27), but here the operators are not only uncorrelated at different frequencies but also at different positions. The normalization factors $j_{0,e}(\mathbf{r}, \omega)$ and $j_{0,m}(\mathbf{r}, \omega)$ in Eqs. (2.35) and (2.36) are given by $j_{0,e}(\mathbf{r}, \omega) = \sqrt{4\pi\hbar\omega^2 \varepsilon_0 \varepsilon_i(\mathbf{r}, \omega)}$ and $j_{0,m}(\mathbf{r}, \omega) = \sqrt{4\pi\hbar\omega^2 \mu_0 \mu_i(\mathbf{r}, \omega)}$ ensuring that the field commutation relation in Eq. (2.31) is satisfied [24, 26, 100].

Substituting the polarization and magnetization noise-current operators in Eqs. (2.35) and (2.36) into the classical expressions for the electric and magnetic fields in terms of the Green's functions in Eqs. (2.14) and (2.16), we then obtain the positive frequency parts of the electric and magnetic field operators as

$$
\begin{aligned}
\hat{\mathbf{E}}^+(\mathbf{r},\omega) = \sum_k \int &\Big[ i\omega\mu_0 j_{0,\mathrm{e}}(\mathbf{r}',\omega) \overset{\leftrightarrow}{\mathbf{G}}_{\mathrm{ee}}(\mathbf{r},\omega,\mathbf{r}') \cdot \hat{\mathbf{e}}_k \hat{f}_{\mathrm{e}}(\mathbf{r}',\omega) \\
&+ k_0 j_{0,\mathrm{m}}(\mathbf{r}',\omega) \overset{\leftrightarrow}{\mathbf{G}}_{\mathrm{em}}(\mathbf{r},\omega,\mathbf{r}') \cdot \hat{\mathbf{e}}_k \hat{f}_{\mathrm{m}}(\mathbf{r}',\omega) \Big] d^3 r',
\end{aligned} \qquad (2.38)
$$

$$
\begin{aligned}
\hat{\mathbf{H}}^+(\mathbf{r},\omega) = \sum_k \int &\Big[ i\omega\varepsilon_0 j_{0,\mathrm{m}}(\mathbf{r}',\omega) \overset{\leftrightarrow}{\mathbf{G}}_{\mathrm{mm}}(\mathbf{r},\omega,\mathbf{r}') \cdot \hat{\mathbf{e}}_k \hat{f}_{\mathrm{m}}(\mathbf{r}',\omega) \\
&+ k_0 j_{0,\mathrm{e}}(\mathbf{r}',\omega) \overset{\leftrightarrow}{\mathbf{G}}_{\mathrm{me}}(\mathbf{r},\omega,\mathbf{r}') \cdot \hat{\mathbf{e}}_k \hat{f}_{\mathrm{e}}(\mathbf{r}',\omega) \Big] d^3 r',
\end{aligned} \qquad (2.39)
$$

The negative frequency parts are given by Hermitian conjugates. These field operators can be shown to result in the same cross-spectral correlation functions as obtained by using FDT in Sec. 2.1.3. From this fact, it also follows that the field fluctuations that will be presented in Sec. 3.1.4 are equal to those obtained by using the classical FED.

### 2.2.4 Wigner function formalism

Next, we review the standard relations of the Wigner function formalism [101] that can be applied in cases where the ladder operators and photon numbers are not position dependent, e.g., in the studies of the output field of a beam splitter setup. The Wigner function theory is commonly applied to model experiments based on optical quantum tomography [65, 102–106].

*Wigner function*

A quantum phase space distribution can be constructed to calculate observable quantities in a classical-like fashion. This quantum phase space distribution is called Wigner function according to its inventor Eugene Wigner who developed the distribution in 1932 while studying quantum corrections to classical mechanics [101]. A useful representation of the Wigner function of a state corresponding to the density operator $\hat{\rho}$ is given in a coherent basis by [107]

$$
W(\alpha) = \frac{1}{\pi^2} \int_{-\infty}^{\infty} \int_{-\infty}^{\infty} e^{\lambda^*\alpha - \lambda\alpha^*} \mathrm{Tr}\Big( \hat{\rho} \underbrace{e^{\lambda\hat{a}^\dagger - \lambda^*\hat{a}}}_{\hat{D}(\lambda)} \Big) d^2\lambda, \qquad (2.40)
$$

where $\hat{a}$ and $\hat{a}^\dagger$ are annihilation and creation operators obeying the canonical commutation relation in Eq. (2.27) and $\hat{D}$ is the displacement operator

which forms a coherent state from a vacuum state as $\hat{D}(\alpha)|0\rangle = |\alpha\rangle$ [16].

The basis variables $\alpha$ and $\alpha^*$ of the coherent basis obey the relations $\hat{a}|\alpha\rangle = \alpha|\alpha\rangle$ and $\langle\alpha|\hat{a}^\dagger = \langle\alpha|\alpha^*$ [107]. These variables are clearly not independent as being a complex number and its conjugate. Their relation to the position and momentum quadrature variables $x$ and $p$ is given by $x = (\alpha + \alpha^*)/(\sqrt{2}\kappa)$ and $p = -i\hbar\kappa(\alpha - \alpha^*)/\sqrt{2}$, where $\kappa$ is the spring constant of the field oscillator.

In many cases, it is useful to compare quantum states with each other. A practical measure for this purpose is the fidelity, which is a measure of closeness of two quantum states. A commonly used definition is the Bures-Uhlmann fidelity [108, 109]. If at least one of the states is pure, the fidelity is given by the overlap between the states as [110]

$$F(W_1, W_2) = \pi \int_{-\infty}^{\infty} \int_{-\infty}^{\infty} W_1(\alpha)W_2(\alpha)\, d^2\alpha. \qquad (2.41)$$

In the Wigner function formalism, the expectation value of an operator can be calculated in two ways. In the case of an operator $\hat{O}$, the first method is to calculate the Wigner function $W_{\hat{O}}(\alpha)$ of $\hat{O}$ by using Eq. (2.40), where the density operator $\hat{\rho}$ has been replaced with $\hat{O}$. Then, the expectation value can be calculated as an overlap between $W_{\hat{O}}(\alpha)$ and the Wigner function of the state as

$$\langle\hat{O}\rangle = \pi \int_{-\infty}^{\infty} \int_{-\infty}^{\infty} W_{\hat{O}}(\alpha)W(\alpha)\, d^2\alpha. \qquad (2.42)$$

Another possibility for calculating expectation values is to mirror the action of the operator $\hat{O}$ directly on the Wigner function as follows [107]

$$\langle\hat{O}\rangle = \int_{-\infty}^{\infty} \int_{-\infty}^{\infty} \hat{D}_{\hat{O}}W(\alpha)\, d^2\alpha. \qquad (2.43)$$

Here $\hat{D}_{\hat{O}}$ is a differential operator corresponding to the operator $\hat{O}$. For example, an operator correspondence relation for the annihilation operator $\hat{a}$ is given by $\hat{D}_{\hat{a}} = \alpha + (1/2)\partial/\partial\alpha^*$ [111].

*Beam splitter description*

The Wigner function of an output state of a beam splitter has four degrees of freedom, two from each initial fields, and it can be written in terms of the initial Wigner functions $W_1$ and $W_2$ as [16, 17]

$$W'(\alpha_1, \alpha_2) = W_1(\alpha_1')W_2(\alpha_2') \qquad (2.44)$$

with the changed variables

$$\begin{pmatrix} \alpha_1' \\ \alpha_2' \end{pmatrix} = \mathbf{S}_{\mathrm{BS}}^\dagger \begin{pmatrix} \alpha_1 \\ \alpha_2 \end{pmatrix}, \qquad (2.45)$$

where $\mathbf{S}_{\text{BS}}$ is the scattering matrix of a beam splitter given in Eq. (2.33).

The Wigner functions of the emerging fields, $W_1'$ and $W_2'$, can be calculated as marginal distributions by integrating $W'$ with respect to the mode variables of the other emerging field, $\alpha_1$ or $\alpha_2$ depending on the output field as

$$W_1'(\alpha) = \int_{-\infty}^{\infty}\int_{-\infty}^{\infty} W'(\alpha,\alpha_2)\,d^2\alpha_2, \tag{2.46}$$

$$W_2'(\alpha) = \int_{-\infty}^{\infty}\int_{-\infty}^{\infty} W'(\alpha_1,\alpha)\,d^2\alpha_1. \tag{2.47}$$

If one knows the initial Wigner functions and observes the Wigner function of one emerging beam in a state $W_1'$, it is possible to calculate the Wigner function of the second output using standard relation of conditional probability given by

$$W_2'(\alpha) = \frac{\pi\int W'(\alpha_1,\alpha)W_1'(\alpha_1)d^2\alpha_1}{\pi\int W'(\alpha_1,\alpha_2)W_1'(\alpha_1)d^2\alpha_1 d^2\alpha_2}. \tag{2.48}$$

The numerator describes the overlap of the Wigner functions and the denominator equals the probability of observation and it renormalizes the obtained distribution.

*Quantum states of light*

Coherent, Fock, and thermal states are examples of the most commonly described quantum states of light. Coherent states are eigenstates of the annihilation operator. They are the closest quantum states to a classical sinusoidal wave such as a continuous laser wave. Fock states are eigenstates of the photon-number operator, thus having a perfectly fixed photon number. Thermal states are equilibrium states for a field coupled to a reservoir at temperature $T$, and their photon statistics obeys the Bose–Einstein distribution. The Wigner functions of these states are given, respectively, by [107]

$$W_{\text{coh}}(\alpha) = \frac{2}{\pi}\exp(-2|\alpha-\alpha_0|^2), \tag{2.49}$$

$$W_{|n\rangle\langle n|}(\alpha) = \frac{2(-1)^n}{\pi}\exp(-2|\alpha|^2)L_n(4|\alpha|^2), \tag{2.50}$$

$$W_{\text{th}}(\alpha) = \frac{2}{\pi}\tanh\left(\frac{\hbar\omega}{2k_BT}\right)\exp\left[-2|\alpha|^2\tanh\left(\frac{\hbar\omega}{2k_BT}\right)\right]. \tag{2.51}$$

Here $\alpha_0$ is the displacement parameter of a coherent state and $L_n$ denote Laguerre polynomials, which can be defined by the Rodrigues' formula, given by

$$L_n(x) = \frac{e^x}{n!}\frac{d^n}{dx^n}\left(e^{-x}x^n\right). \tag{2.52}$$

# 3. Developed models

This chapter reviews the key elements of the new theory of the QFED formalism developed in Publications II–VII and the coupled state description of the field and matter developed in Publication VIII. Section 3.1 describes the consistent commutation-relation-preserving photon-ladder operators and the related position-dependent photon-number concept of the QFED formalism. It also reviews the related density of state concepts and the application of the QFED method to the description of the local thermal balance between the field and matter. The separation of the ladder operators and photon numbers into the left and right propagating parts and the related quantum optical RTE are also described. Section 3.2 covers our coupled state description of the field and matter. While the QFED method mainly concentrates on describing photon numbers, in Sec. 3.2 we model light propagation in a medium as MP quasiparticles, coupled states of the field and matter. The MP and OCD models are shown to lead to the photon mass drag effect and the emergence of a MDW, which is inevitably associated with a light pulse propagating in a medium.

## 3.1 Quantized fluctuational electrodynamics

This section reviews the QFED formalism developed in this thesis in Publications II–VII. In Sec. 3.1.1, we describe the source-field number operator. In Sec. 3.1.2, we review the derivation of the consistent commutation-relation-preserving photon-ladder operators of the QFED formalism applicable to nonuniform structures and non-equilibrium conditions. This is followed by the review of the density of state concepts in Sec. 3.1.3 and the presentation of the photon numbers and field fluctuations in Sec. 3.1.4. The application of the QFED formalism to the description of the local

thermal balance is reviewed in Sec. 3.1.5. The separation of the ladder operators and photon numbers into the left and right propagating parts is described in Sec. 3.1.6 and the related quantum optical RTE is reviewed in Sec. 3.1.7. Here, we present certain parts of the theory in a one-dimensional form for easier interpretation, while other parts are presented in the complete three-dimensional form as described for dielectric and magnetic media in Publication VI.

### 3.1.1 Source-field number operator

As described in the one-dimensional case in Publication II, the bosonic source-field operators $\hat{f}_j(\mathbf{r}, \omega)$ of Sec. 2.2.3 give the local source-field number operator $\hat{\eta}(\mathbf{r}, \omega)$ as $\hat{\eta}(\mathbf{r}, \omega) = \int \hat{f}_j^\dagger(\mathbf{r}, \omega) \hat{f}_j(\mathbf{r}', \omega') d^3r' d\omega'$. In the case of thermal fields, the expectation value of the operator $\hat{\eta}(\mathbf{r}, \omega)$ is given by the Bose–Einstein distribution as $\langle \hat{\eta}(\mathbf{r}, \omega) \rangle = 1/(e^{\hbar\omega/[k_\mathrm{B}T(\mathbf{r})]} - 1)$, in which $T(\mathbf{r})$ is the possibly position-dependent temperature profile of the medium. In thermal non-equilibrium conditions, the local thermal equilibrium (LTE) approximation is often applied. The LTE approximation is justified when the temperature gradients are small compared to a material-dependent current-current correlation length scale, which is of the order of the atomic scale or the phonon mean-free path [86].

### 3.1.2 Commutation-relation-preserving ladder operators

In any NOF description, the canonical commutation relations are satisfied for field quantities, i.e., Eq. (2.31) [99], but the same is not generally true for the canonical commutation relations of the ladder operators in Eq. (2.27). The dominant approach in evaluating the ladder operators has been to separate the field operators obtained from QED into the left and right propagating normal modes $u_\mathrm{L}(x, \omega)$ and $u_\mathrm{R}(x, \omega)$ and the corresponding ladder operators $\hat{a}_\mathrm{L}(\omega)$ and $\hat{a}_\mathrm{R}(\omega)$ so that, e.g., the spectral component of the vector potential operator of a field propagating along $x$ axis is written as $\hat{A}^+(x, \omega) = u_\mathrm{R}(x, \omega)\hat{a}_\mathrm{R}(\omega) + u_\mathrm{L}(x, \omega)\hat{a}_\mathrm{L}(\omega)$ [29, 30, 112]. This is tempting in view of the analogy with the field operators in free space given in Eqs. (2.28)–(2.30), but in most cases results in ladder operators that are not uniquely determined due to the possibility to scale the normal modes nearly arbitrarily. More recently, physically more transparent interpretations also accounting for the noise contribution have been

reported [31], but none of the previously reported definitions consistently give the canonical commutation relations for the photon ladder operators.

In the QFED formalism, we adopt a different starting point that ensures the preservation of the canonical commutation relations of the ladder operators by simply writing the electric field operator as $\hat{E}^+(x,\omega) = C_{\mathrm{e}}(x,\omega)\hat{a}_{\mathrm{e}}(x,\omega)$, where $\hat{a}_{\mathrm{e}}(x,\omega)$ is the position-dependent electric part of the photon annihilation operator and $C_{\mathrm{e}}(x,\omega)$ is a normalization factor that corresponds to the classical mode function defined simultaneously for all the source points. This simple relation between $\hat{E}^+(x,\omega)$ and $\hat{a}_{\mathrm{e}}(x,\omega)$ is obviously of the same form as that in free space in Eq. (2.29). The electric part of the photon annihilation operator is then given by $\hat{a}_{\mathrm{e}}(x,\omega) = \hat{E}^+(x,\omega)/C_{\mathrm{e}}(x,\omega)$ and the normalization factor $C_{\mathrm{e}}(x,\omega)$ can be uniquely determined apart from the possible phase factor by requiring that the canonical commutation relation $[\hat{a}_{\mathrm{e}}(x,\omega), \hat{a}_{\mathrm{e}}^\dagger(x,\omega')] = \delta(\omega-\omega')$, corresponding to Eq. (2.27), is fulfilled at any position.

Above, the photon annihilation operator has been normalized with respect to the electric field. However, it is also possible to perform a corresponding normalization with respect to the magnetic field or other suitable quantity like the field component propagating in a certain direction as discussed later in Sec. 3.1.6. In the case of the normalization with respect to the magnetic field as $\hat{a}_{\mathrm{m}}(x,\omega) = \hat{H}^+(x,\omega)/C_{\mathrm{m}}(x,\omega)$, we denote the magnetic part of the photon annihilation operator with $\hat{a}_{\mathrm{m}}(x,\omega)$ and the corresponding normalization factor with $C_{\mathrm{m}}(x,\omega)$. Depending on the normalization, we obtain in general different photon ladder operators $\hat{a}_{\mathrm{e}}(\mathbf{r},\omega)$, $\hat{a}_{\mathrm{m}}(\mathbf{r},\omega)$, and $\hat{a}(\mathbf{r},\omega)$ and normalization factors $C_{\mathrm{e}}(x,\omega)$, $C_{\mathrm{m}}(x,\omega)$, and $C(x,\omega)$ for the electric, magnetic, and total electromagnetic fields. As presented in Publication III, using the explicit forms of the normalization factors, the electric and magnetic parts of the photon annihilation operator are then given by

$$\hat{a}_{\mathrm{e}}(x,\omega) = \sqrt{\frac{\varepsilon_0}{2\pi^2\hbar\omega\rho_{\mathrm{e}}(x,\omega)}}\hat{E}^+(x,\omega), \tag{3.1}$$

$$\hat{a}_{\mathrm{m}}(x,\omega) = \sqrt{\frac{\mu_0}{2\pi^2\hbar\omega\rho_{\mathrm{m}}(x,\omega)}}\hat{H}^+(x,\omega), \tag{3.2}$$

where $\rho_{\mathrm{e}}(x,\omega)$ and $\rho_{\mathrm{m}}(x,\omega)$ are, respectively, the one-dimensional electric and magnetic LDOSs and the electric and magnetic field operators are those obtained by using NOF given in Eqs. (2.38) and (2.39). The photon annihilation operator $\hat{a}(x,\omega)$ for the total electromagnetic field is

defined as a linear combination of the electric and magnetic field annihilation operators as discussed in Publications III and V. As conventional, the corresponding photon creation operators are Hermitian conjugates of the annihilation operators.

When we substitute the electric and magnetic field operators from Eqs. (2.14) and (2.16) into Eqs. (3.1) and (3.2), we obtain more abstract expressions for the annihilation operators in terms of the bosonic field operators $\hat{f}_\mathrm{e}(x,\omega)$ and $\hat{f}_\mathrm{m}(x,\omega)$. In terms of the three-dimensional nonlocal densities of states (NLDOSs) described in Publication VI and reviewed below, the electric and magnetic parts of the photon annihilation operators are given by

$$\hat{a}_j(\mathbf{r},\omega) = \frac{\int \left[ \sqrt{\rho_{\mathrm{NL},j}^{\mathrm{e}}(\mathbf{r},\omega,\mathbf{r}')}\hat{f}_\mathrm{e}(\mathbf{r}',\omega) + \sqrt{\rho_{\mathrm{NL},j}^{\mathrm{m}}(\mathbf{r},\omega,\mathbf{r}')}\hat{f}_\mathrm{m}(\mathbf{r}',\omega) \right] d^3r'}{\sqrt{\int \rho_{\mathrm{NL},j}(\mathbf{r},\omega,\mathbf{r}')d^3r'}}, \quad (3.3)$$

where $j \in \{\mathrm{e},\mathrm{m}\}$. The NLDOS components $\rho_{\mathrm{NL},j}^{\mathrm{e}}(\mathbf{r},\omega,\mathbf{r}')$ and $\rho_{\mathrm{NL},j}^{\mathrm{m}}(\mathbf{r},\omega,\mathbf{r}')$ in Eq. (3.3) denote, respectively, the first and the second terms of Eqs. (3.9) and (3.10) below. An equation corresponding to Eq. (3.3) also holds for the total annihilation operator $\hat{a}(\mathbf{r},\omega)$. In this case, the total NLDOS terms $\rho_{\mathrm{NL}}^{\mathrm{e}}(\mathbf{r},\omega,\mathbf{r}')$ and $\rho_{\mathrm{NL}}^{\mathrm{m}}(\mathbf{r},\omega,\mathbf{r}')$ are obtained by using Eq. (3.11) below with the corresponding terms in the electric and magnetic NLDOSs.

For easy comparison with the well-known field operator relations in vacuum in Eqs. (2.29) and (2.30), we next rewrite the time domain electric and magnetic field operators of QFED explicitly in terms of the corresponding photon annihilation operators. The time domain electric and magnetic field operators are naturally given by taking the inverse Fourier transforms of the frequency domain operators in Eqs. (3.1) and (3.2) as done for the electric field operator in Publication II. This results in the one-dimensional case in relations

$$\hat{E}(x,t) = \frac{1}{2\pi} \int_0^\infty C_\mathrm{e}(x,\omega)\left[\hat{a}_\mathrm{e}(x,\omega)e^{-i\omega t} + \hat{a}_\mathrm{e}^\dagger(x,\omega)e^{i\omega t}\right]d\omega, \quad (3.4)$$

$$\hat{H}(x,t) = \frac{1}{2\pi} \int_0^\infty C_\mathrm{m}(x,\omega)\left[\hat{a}_\mathrm{m}(x,\omega)e^{-i\omega t} + \hat{a}_\mathrm{m}^\dagger(x,\omega)e^{i\omega t}\right]d\omega, \quad (3.5)$$

which clearly resemble the equations for the field operators in the well-known field quantization in free space given in Eqs. (2.29) and (2.30). However, the field operators and their prefactors are now in general both position dependent, which is not the case with the free-space field operators in Eqs. (2.29) and (2.30).

### 3.1.3 Densities of states

Following the calculation performed in the three-dimensional case in Publication VI, we can define the electric, magnetic, and total electromagnetic NLDOSs $\rho_{\mathrm{NL},e}(\mathbf{r},\omega,\mathbf{r}')$, $\rho_{\mathrm{NL},m}(\mathbf{r},\omega,\mathbf{r}')$, and $\rho_{\mathrm{NL}}(\mathbf{r},\omega,\mathbf{r}')$ as factors that appear in the expressions for the field fluctuations. In terms of the NLDOSs, the electric and magnetic field fluctuations and the total energy density of the electromagnetic field are written as

$$\langle E^2(\mathbf{r},t)\rangle = \int_0^\infty \int \frac{\hbar\omega}{\varepsilon_0}\rho_{\mathrm{NL,e}}(\mathbf{r},\omega,\mathbf{r}')\Big[\langle\hat{\eta}(\mathbf{r}',\omega)\rangle+\frac{1}{2}\Big]d^3r'd\omega, \quad (3.6)$$

$$\langle H^2(\mathbf{r},t)\rangle = \int_0^\infty \int \frac{\hbar\omega}{\mu_0}\rho_{\mathrm{NL,m}}(\mathbf{r},\omega,\mathbf{r}')\Big[\langle\hat{\eta}(\mathbf{r}',\omega)\rangle+\frac{1}{2}\Big]d^3r'd\omega, \quad (3.7)$$

$$\langle u(\mathbf{r},t)\rangle = \int_0^\infty \int \hbar\omega\rho_{\mathrm{NL}}(\mathbf{r},\omega,\mathbf{r}')\Big[\langle\hat{\eta}(\mathbf{r}',\omega)\rangle+\frac{1}{2}\Big]d^3r'd\omega. \quad (3.8)$$

As shown in Publication VI, the NLDOSs for the electric, magnetic, and total electromagnetic fields, can be written as

$$\rho_{\mathrm{NL,e}}(\mathbf{r},\omega,\mathbf{r}') = \frac{2\omega^3}{\pi c^4}\Big\{\varepsilon_i(\mathbf{r}',\omega)\mathrm{Tr}[\overleftrightarrow{\mathbf{G}}_{\mathrm{ee}}(\mathbf{r},\omega,\mathbf{r}')\cdot\overleftrightarrow{\mathbf{G}}_{\mathrm{ee}}^\dagger(\mathbf{r},\omega,\mathbf{r}')]$$
$$+ \mu_i(\mathbf{r}',\omega)\mathrm{Tr}[\overleftrightarrow{\mathbf{G}}_{\mathrm{em}}(\mathbf{r},\omega,\mathbf{r}')\cdot\overleftrightarrow{\mathbf{G}}_{\mathrm{em}}^\dagger(\mathbf{r},\omega,\mathbf{r}')]\Big\}, \quad (3.9)$$

$$\rho_{\mathrm{NL,m}}(\mathbf{r},\omega,\mathbf{r}') = \frac{2\omega^3}{\pi c^4}\Big\{\varepsilon_i(\mathbf{r}',\omega)\mathrm{Tr}[\overleftrightarrow{\mathbf{G}}_{\mathrm{me}}(\mathbf{r},\omega,\mathbf{r}')\cdot\overleftrightarrow{\mathbf{G}}_{\mathrm{me}}^\dagger(\mathbf{r},\omega,\mathbf{r}')]$$
$$+ \mu_i(\mathbf{r}',\omega)\mathrm{Tr}[\overleftrightarrow{\mathbf{G}}_{\mathrm{mm}}(\mathbf{r},\omega,\mathbf{r}')\cdot\overleftrightarrow{\mathbf{G}}_{\mathrm{mm}}^\dagger(\mathbf{r},\omega,\mathbf{r}')]\Big\}, \quad (3.10)$$

$$\rho_{\mathrm{NL}}(\mathbf{r},\omega,\mathbf{r}') = \frac{|\varepsilon(\mathbf{r},\omega)|}{2}\rho_{\mathrm{NL,e}}(\mathbf{r},\omega,\mathbf{r}') + \frac{|\mu(\mathbf{r},\omega)|}{2}\rho_{\mathrm{NL,m}}(\mathbf{r},\omega,\mathbf{r}'). \quad (3.11)$$

The LDOSs $\rho_e(\mathbf{r},\omega)$, $\rho_m(\mathbf{r},\omega)$, and $\rho(\mathbf{r},\omega)$ are obtained as integrals of the corresponding NLDOSs as

$$\rho_j(\mathbf{r},\omega) = \int \rho_{\mathrm{NL},j}(\mathbf{r},\omega,\mathbf{r}')d^3r', \quad (3.12)$$

where $j\in\{\mathrm{e,m,tot}\}$ in which the index tot denotes the quantities for the total electromagnetic field, e.g., $\rho_{\mathrm{NL}}(\mathbf{r},\omega,\mathbf{r}')$ in Eq. (3.11), written throughout this thesis without the subscript tot for brevity. It is well-known that the electric and magnetic LDOSs $\rho_e(\mathbf{r},\omega)$ and $\rho_m(\mathbf{r},\omega)$ are given in vacuum by the imaginary parts of the traces of the dyadic Green's functions as [84, 92]

$$\rho_j(\mathbf{r},\omega) = \frac{2\omega}{\pi c^2}\mathrm{Im}\{\mathrm{Tr}[\overleftrightarrow{\mathbf{G}}_{jj}(\mathbf{r},\omega,\mathbf{r})]\}, \quad (3.13)$$

where $j\in\{\mathrm{e,m}\}$. As described in Publication III, a similar relation also applies for the normal components of the Fourier-transformed quantities

in stratified media. Typically, the spatially resolved form in Eq. (3.13) is also expected to be valid inside lossy media. However, in lossy media, these LDOSs are generally known to become infinite due to the contribution of evanescent fields, which do not propagate in the medium as electromagnetic waves, but whose energy density is spatially concentrated in the vicinity of the field sources [84, 92].

Next we also familiarize the concept of the interference density of states (IFDOS) that was introduced in Publication IV and that is related to the definition of the Poynting vector. The quantum optical Poynting vector of an optical mode is defined as a normal-ordered operator in terms of the positive- and negative-frequency parts of the electric and magnetic field operators as $\hat{\mathbf{S}}(\mathbf{r}, t) =: \hat{\mathbf{E}}(\mathbf{r}, t) \times \hat{\mathbf{H}}(\mathbf{r}, t) := \hat{\mathbf{E}}^-(\mathbf{r}, t) \times \hat{\mathbf{H}}^+(\mathbf{r}, t) - \hat{\mathbf{H}}^-(\mathbf{r}, t) \times \hat{\mathbf{E}}^+(\mathbf{r}, t)$ [98]. As detailed in the three-dimensional case in Publication VI, we obtain the Poynting vector expectation value as

$$\langle \hat{\mathbf{S}}(\mathbf{r}, t) \rangle = \int_0^\infty \int \hbar \omega v(\mathbf{r}, \omega) \boldsymbol{\rho}_{\mathrm{IF}}(\mathbf{r}, \omega, \mathbf{r}') \langle \hat{\eta}(\mathbf{r}', \omega) \rangle d^3 r' d\omega, \quad (3.14)$$

where $v(\mathbf{r}, \omega) = c/n_{\mathrm{r}}(\mathbf{r}, \omega)$ is the propagation velocity of the field in the direction of the wave vector with the real part of the refractive index denoted by $n_{\mathrm{r}}(\mathbf{r}, \omega)$. Inside the integral in Eq. (3.14), we have defined the IFDOS $\boldsymbol{\rho}_{\mathrm{IF}}(\mathbf{r}, \omega, \mathbf{r}')$ as

$$\begin{aligned}
\boldsymbol{\rho}_{\mathrm{IF}}(\mathbf{r}, \omega, \mathbf{r}') = \frac{2\omega^3 n_{\mathrm{r}}(\mathbf{r}, \omega)}{\pi c^4} \\
\times \Big( \mu_{\mathrm{i}}(\mathbf{r}', \omega) \mathrm{Im}\Big\{ \mathrm{Tr}[\overset{\leftrightarrow}{\mathbf{G}}_{\mathrm{mm}}(\mathbf{r}, \omega, \mathbf{r}') \times \overset{\leftrightarrow}{\mathbf{G}}_{\mathrm{em}}^\dagger(\mathbf{r}, \omega, \mathbf{r}')] \Big\} \\
- \varepsilon_{\mathrm{i}}(\mathbf{r}', \omega) \mathrm{Im}\Big\{ \mathrm{Tr}[\overset{\leftrightarrow}{\mathbf{G}}_{\mathrm{ee}}(\mathbf{r}, \omega, \mathbf{r}') \times \overset{\leftrightarrow}{\mathbf{G}}_{\mathrm{me}}^\dagger(\mathbf{r}, \omega, \mathbf{r}')] \Big\} \Big). \quad (3.15)
\end{aligned}$$

Here we have used the shorthand notation $\mathrm{Tr}[\overset{\leftrightarrow}{\mathbf{G}}_1(\mathbf{r}, \omega, \mathbf{r}') \times \overset{\leftrightarrow}{\mathbf{G}}_2^\dagger(\mathbf{r}, \omega, \mathbf{r}')] = \sum_j [\overset{\leftrightarrow}{\mathbf{G}}_1(\mathbf{r}, \omega, \mathbf{r}') \cdot \hat{\mathbf{e}}_j] \times [\overset{\leftrightarrow}{\mathbf{G}}_2(\mathbf{r}, \omega, \mathbf{r}') \cdot \hat{\mathbf{e}}_j]^\dagger$, where the result is by definition a vector, in contrast to the conventional trace of a matrix, which is a scalar. The integral of the IFDOS with respect to $\mathbf{r}'$ is always zero, i.e., $\int \boldsymbol{\rho}_{\mathrm{IF}}(\mathbf{r}, \omega, \mathbf{r}') d^3 r' = 0$, which is required by the fact that, in a medium at thermal equilibrium, there is no net energy flow.

In Publication IV, it was found that the IFDOS concept describing interference effects is instrumental in allowing an unambiguous separation of the fields and the related quantum operators into parts propagating in different directions. This is described further in Sec. 3.1.6.

### 3.1.4 Photon numbers and field fluctuations

Using, the ladder operators presented in Sec. 3.1.2 and the source-field photon-number expectation value given for thermal fields in Sec. 3.1.1, the position-dependent photon-number expectation values are given for the electric, magnetic, and total electromagnetic fields, $j \in \{\mathrm{e}, \mathrm{m}, \mathrm{tot}\}$, by

$$\langle \hat{n}_j(\mathbf{r}, \omega) \rangle = \frac{\int \rho_{\mathrm{NL},j}(\mathbf{r}, \omega, \mathbf{r}') \langle \hat{\eta}(\mathbf{r}', \omega) \rangle d^3 r'}{\int \rho_{\mathrm{NL},j}(\mathbf{r}, \omega, \mathbf{r}') d^3 r'}. \tag{3.16}$$

In terms of the photon-number expectation values in Eq. (3.16) and the LDOSs in Eq. (3.12), the spectral electric and magnetic field fluctuations and the energy density in Eqs. (3.6)–(3.8) can be written as

$$\langle \hat{E}^2(\mathbf{r}, t) \rangle_\omega = \frac{\hbar \omega}{\varepsilon_0} \rho_{\mathrm{e}}(\mathbf{r}, \omega) \Big[ \langle \hat{n}_{\mathrm{e}}(\mathbf{r}, \omega) \rangle + \frac{1}{2} \Big], \tag{3.17}$$

$$\langle \hat{H}^2(\mathbf{r}, t) \rangle_\omega = \frac{\hbar \omega}{\mu_0} \rho_{\mathrm{m}}(\mathbf{r}, \omega) \Big[ \langle \hat{n}_{\mathrm{m}}(\mathbf{r}, \omega) \rangle + \frac{1}{2} \Big], \tag{3.18}$$

$$\langle \hat{u}(\mathbf{r}, t) \rangle_\omega = \hbar \omega \rho(\mathbf{r}, \omega) \Big[ \langle \hat{n}(\mathbf{r}, \omega) \rangle + \frac{1}{2} \Big]. \tag{3.19}$$

Here the subscript $\omega$ denotes the spectral component of the total quantities which are obtained as integrals over positive frequencies. These expressions are equivalent with the spectral components of the field fluctuations and the energy density obtained in the classical FED. Therefore, we can conclude that using the canonical commutation relations of the source-field operators as a starting point automatically leads to results that are consistent with FDT.

### 3.1.5 Thermal balance

An insightful view of the effective photon numbers of the QFED framework in Eq. (3.16) is provided by their connection to local thermal balance between the field and matter as detailed in Publication II and as described in the three-dimensional case in Publication VI. For the macroscopic description of the field–matter interaction, we first define the normal-ordered emission and absorption operators $\hat{Q}_{\mathrm{em}}(\mathbf{r}, t)$ and $\hat{Q}_{\mathrm{abs}}(\mathbf{r}, t)$ as

$$\hat{Q}_{\mathrm{em}}(\mathbf{r}, t) = -:\hat{\mathbf{J}}_{\mathrm{e}}(\mathbf{r}, t) \cdot \hat{\mathbf{E}}(\mathbf{r}, t): - :\hat{\mathbf{J}}_{\mathrm{m}}(\mathbf{r}, t) \cdot \hat{\mathbf{H}}(\mathbf{r}, t):, \tag{3.20}$$

$$\hat{Q}_{\mathrm{abs}}(\mathbf{r}, t) = :\hat{\mathbf{J}}_{\mathrm{e,abs}}(\mathbf{r}, t) \cdot \hat{\mathbf{E}}(\mathbf{r}, t): + :\hat{\mathbf{J}}_{\mathrm{m,abs}}(\mathbf{r}, t) \cdot \hat{\mathbf{H}}(\mathbf{r}, t): . \tag{3.21}$$

Here $\hat{\mathbf{J}}_{\mathrm{e,abs}}(\mathbf{r}, t)$ and $\hat{\mathbf{J}}_{\mathrm{m,abs}}(\mathbf{r}, t)$ are the electric and magnetic absorption-current operators that are written in the spectral domain in terms of the

electric and magnetic field operators as $\hat{\mathbf{J}}_{e,abs}^{+}(\mathbf{r},\omega) = -i\omega\varepsilon_0\chi_e(\mathbf{r},\omega)\hat{\mathbf{E}}^{+}(\mathbf{r},\omega)$ and $\hat{\mathbf{J}}_{m,abs}^{+}(\mathbf{r},\omega) = -i\omega\mu_0\chi_m(\mathbf{r},\omega)\hat{\mathbf{H}}^{+}(\mathbf{r},\omega)$, where $\chi_e(\mathbf{r},\omega) = \varepsilon(\mathbf{r},\omega) - 1$ and $\chi_m(\mathbf{r},\omega) = \mu(\mathbf{r},\omega) - 1$ are the electric and magnetic susceptibilities of the medium.

The net emission operator $\hat{Q}(\mathbf{r},t)$ is defined as the difference of the emission and absorption operators in Eqs. (3.20) and (3.21) as $\hat{Q}(\mathbf{r},t) = \hat{Q}_{em}(\mathbf{r},t) - \hat{Q}_{abs}(\mathbf{r},t)$. It describes the total energy transfer between the electromagnetic field and the local medium and it is given by

$$\hat{Q}(\mathbf{r},t) = -:\hat{\mathbf{J}}_{e,tot}(\mathbf{r},t) \cdot \hat{\mathbf{E}}(\mathbf{r},t): -:\hat{\mathbf{J}}_{m,tot}(\mathbf{r},t) \cdot \hat{\mathbf{H}}(\mathbf{r},t):. \qquad (3.22)$$

Here $\hat{\mathbf{J}}_{e,tot}(\mathbf{r},t) = \hat{\mathbf{J}}_e(\mathbf{r},t) + \hat{\mathbf{J}}_{e,abs}(\mathbf{r},t)$ and $\hat{\mathbf{J}}_{m,tot}(\mathbf{r},t) = \hat{\mathbf{J}}_m(\mathbf{r},t) + \hat{\mathbf{J}}_{m,abs}(\mathbf{r},t)$ are the total noise-current operators, which correspond to the classical total current densities that are sums of the classical free and bound current densities. As presented in the three-dimensional case in Publication VI, the spectral component of the expectation value of the net emission operator in Eq. (3.22) can be written in terms of the LDOSs and the electric and magnetic parts of the photon number in Eq. (3.16) as

$$\begin{aligned} &\langle\hat{Q}(\mathbf{r},t)\rangle_\omega \\ &= \hbar\omega^2\varepsilon_i(\mathbf{r},\omega)\rho_e(\mathbf{r},\omega)[\langle\hat{\eta}(\mathbf{r},\omega)\rangle - \langle\hat{n}_e(\mathbf{r},\omega)\rangle] \\ &\quad + \hbar\omega^2\mu_i(\mathbf{r},\omega)\rho_m(\mathbf{r},\omega)[\langle\hat{\eta}(\mathbf{r},\omega)\rangle - \langle\hat{n}_m(\mathbf{r},\omega)\rangle]. \end{aligned} \qquad (3.23)$$

From Eq. (3.23) it follows that local thermal balance, described by the condition $\langle\hat{Q}(\mathbf{r},t)\rangle_\omega = 0$, is generally reached when the source-field photon numbers coincide with the electric and magnetic field parts of the photon number defined in Eq. (3.16). One can also note that the expectation value of the net emission operator in Eq. (3.23) equals the divergence of the Poynting vector in Eq. (3.14) as $\langle\hat{Q}(\mathbf{r},t)\rangle_\omega = \nabla \cdot \langle\hat{\mathbf{S}}(\mathbf{r},t)\rangle_\omega$.

In the case of resonant systems, where the exchange of energy is dominated by a narrow frequency band, the condition $\langle\hat{Q}(\mathbf{r},t)\rangle_\omega = 0$ can be used to approximately determine the steady-state temperature of a resonant particle that is interacting weakly with the electromagnetic field [113]. Therefore, in Publication II, we have suggested that the electric field temperature is experimentally measurable by measuring the steady-state temperature reached by a detector whose field–matter interaction is weak and dominated by the coupling to the electric field. Such a detector is, e.g., the movable transparent intracavity photodetector studied and demonstrated by Lazar *et al.* [114, 115]. In Publication III, we have

also suggested that a similar measurement setup for the measurement of the magnetic field related effective temperature might also be possible to construct. In this kind of a setup, at least at microwave frequencies, one would need to use materials whose field–matter interactions have been engineered to be sensitive to magnetic fields instead of electric fields, using, e.g., magnetic metamaterials [116] or micro-coil sensors [117].

### 3.1.6 Left and right propagating fields

It is commonly known how to separate the electric and magnetic fields into parts propagating in different directions [82, 83]. However, due to the interference of the field components inside resonant structures, the same is not true for all field-related quantities. Especially, in previous literature, it has not been shown how the separation should be made for the energy density or the photon number, which are quantities that do not directly depend on the fields but on their squares.

In Publication IV, we have used the LDOS and photon-number concepts of Publications II and III and Eq. (3.16) to separately account for the left and right propagating fields. In the derivation of this generalization, we first write the left and right propagating field spectral Poynting vector expectation values $\langle \hat{S}_+(x,\omega) \rangle_\omega$ and $\langle \hat{S}_-(x,\omega) \rangle_\omega$ as $\langle \hat{S}_\pm(x,\omega) \rangle_\omega = \hbar \omega v(x,\omega) \rho_\pm(x,\omega) \left[ \langle \hat{n}_\pm(x,\omega) \rangle + \frac{1}{2} \right]$, where $\rho_\pm(x,\omega)$ and $\langle \hat{n}_\pm(x,\omega) \rangle$ are the left and right propagating field LDOSs and photon numbers to be determined, and the term one half describes the zero-point fluctuation current. The left and right propagating photon numbers are additionally assumed to satisfy two equations as the total Poynting vector is given by

$$\langle \hat{S}(x,t) \rangle_\omega = \hbar \omega v(x,\omega) \rho_+(x,\omega) \left[ \langle \hat{n}_+(x,\omega) \rangle + \frac{1}{2} \right]$$
$$- \hbar \omega v(x,\omega) \rho_-(x,\omega) \left[ \langle \hat{n}_-(x,\omega) \rangle + \frac{1}{2} \right], \qquad (3.24)$$

and the total energy density in Eq. (3.19) is given by

$$\langle \hat{u}(x,t) \rangle_\omega = \hbar \omega \rho_+(x,\omega) \left[ \langle \hat{n}_+(x,\omega) \rangle + \frac{1}{2} \right]$$
$$+ \hbar \omega \rho_-(x,\omega) \left[ \langle \hat{n}_-(x,\omega) \rangle + \frac{1}{2} \right]. \qquad (3.25)$$

At zero temperature, where $\langle \hat{n}_+(x,\omega) \rangle = \langle \hat{n}_-(x,\omega) \rangle = 0$, the Poynting vector is also zero and thus the equality of the densities of states of the left and right propagating fields $\rho_+(x,\omega) = \rho_-(x,\omega)$ follows from Eq. (3.24). Respectively, at zero temperature, Eq. (3.25) leads to the relation $\rho_+(x,\omega)+$

$\rho_-(x,\omega) = \rho(x,\omega)$. Together, these conditions uniquely define the left and right propagating LDOSs in terms of the total LDOS as $\rho_+(x,\omega) = \rho_-(x,\omega) = \rho(x,\omega)/2$.

Using the LDOS relations above, we can unambiguously solve the left and right propagating photon numbers from Eqs. (3.24) and (3.25) as $\langle \hat{n}_\pm(x,\omega) \rangle = [\hbar\omega\rho(x,\omega)]^{-1}[\langle \hat{u}(x,t) \rangle_\omega \pm \langle \hat{S}(x,t) \rangle_\omega/v(x,\omega)] - 1/2$. As described in Publication IV, in terms of the densities of states and the source-field photon number, this corresponds to

$$\langle \hat{n}_\pm(x,\omega) \rangle = \frac{1}{\rho(x,\omega)} \int_{-\infty}^{\infty} [\rho_{\mathrm{NL}}(x,\omega,x') \pm \rho_{\mathrm{IF}}(x,\omega,x')] \langle \hat{\eta}(x',\omega) \rangle dx'. \quad (3.26)$$

Equation (3.26) indicates that the propagating field photon-number expectation values are also obtained as weighted sums of the source-field values, but the weight factors now contain an additional IFDOS related term that describes the interference and propagation direction.

Above we have only focused on the photon-number expectation values that are directly related to the Poynting vector and energy density. In order to find the corresponding ladder and photon-number operators in QFED, we investigate the forms of the photon creation and annihilation operators $\hat{a}_\pm^\dagger(x,\omega)$ and $\hat{a}_\pm(x,\omega)$ that fulfill the canonical commutation relations and lead to the photon-number expectation values in Eq. (3.26). The photon annihilation operators satisfying these conditions are of the form

$$\begin{aligned} \hat{a}_\pm&(x,\omega) \\ &= \frac{1}{\sqrt{\rho(x,\omega)}} \int_{-\infty}^{\infty} \Big[ e^{i(\phi_\mathrm{e} \pm \pi/4)} \sqrt{\rho_{\mathrm{NL}}^\mathrm{e}(x,\omega,x') \pm \rho_{\mathrm{IF}}^\mathrm{e}(x,\omega,x')}\, \hat{f}_\mathrm{e}(x',\omega) \\ &\quad + e^{i(\phi_\mathrm{m} \pm \pi/4)} \sqrt{\rho_{\mathrm{NL}}^\mathrm{m}(x,\omega,x') \pm \rho_{\mathrm{IF}}^\mathrm{m}(x,\omega,x')}\, \hat{f}_\mathrm{m}(x',\omega) \Big] dx', \quad (3.27) \end{aligned}$$

where $\rho_{\mathrm{NL}}^j(x,\omega,x')$ and $\rho_{\mathrm{IF}}^j(x,\omega,x')$, with $j \in \{\mathrm{e},\mathrm{m}\}$, denote the electric and magnetic source related terms of the NLDOS and IFDOS in Eqs. (3.11) and (3.15). The phase factors $\phi_\mathrm{e}$ and $\phi_\mathrm{m}$ in Eq. (3.27) are in principle arbitrary and they do not play a role in our calculations as they cancel in the commutators. The annihilation operator $\hat{a}(x,\omega)$ of the total field is given by the sum $\hat{a}(x,\omega) = \frac{1}{\sqrt{2}}[\hat{a}_+(x,\omega) + \hat{a}_-(x,\omega)]$. It is straightforward to verify that the annihilation operators of the left and right propagating field in Eq. (3.27) also obey the commutation relation of the form $[\hat{a}_\pm(x,\omega), \hat{a}_\pm^\dagger(x,\omega')] = \delta(\omega - \omega')$. However, as the reflecting interfaces couple the left and right propagating fields originating from the same source

points, the cross-commutators become nonzero as $[\hat{a}_\pm(x,\omega), \hat{a}^\dagger_\mp(x,\omega')] \neq 0$. This cross-commutator form is intuitively reasonable and it has not been found to present any complications as the only commutation relations that are expected to be directly related to physical observables are the self-commutators.

### 3.1.7 Quantum optical radiative transfer equation

Next, we discuss the connection between the QFED formalism and the well-known RTE model [75–79] whose main limitation is that it does not capture interference effects that are crucial in the exact description of fields in any inhomogeneous structures. The same limitation in the description of interference effects also applies to many recently developed quantum models of light propagation in a medium [118–121]. Therefore, establishing an interference-exact RTE model also provides means to extend the applicability of these non-interference-exact quantum models.

*RTE-model parameters*

Here we assume normal incidence for simplicity but, in Publication VII, the calculations have been performed in the case of general incidence. The connection between QFED and the RTE model is established by comparing the derivative of the photon numbers in Eq. (3.26) with the RTE model for stratified media written as

$$
\frac{d}{dx}\langle \hat{n}_\pm(x,\omega)\rangle = \mp \alpha_\pm(x,\omega)[\langle \hat{n}_\pm(x,\omega)\rangle - \langle \hat{\eta}(x,\omega)\rangle]
$$
$$
\pm \beta_\pm(x,\omega)[\langle \hat{n}_\mp(x,\omega)\rangle - \langle \hat{\eta}(x,\omega)\rangle]. \qquad (3.28)
$$

Here we have allowed that the damping and scattering coefficients $\alpha_\pm(x,\omega)$ and $\beta_\pm(x,\omega)$ can be in general position dependent.

Substituting the integral expressions for the photon numbers of the QFED framework given in Eq. (3.26) into the RTE model in Eq. (3.28) and omitting the function arguments $x$, $x'$, and $\omega$ for brevity, we obtain

$$
\int_{-\infty}^{\infty} \Big( \frac{1}{\rho}\frac{\partial \rho_{\mathrm{NL}\pm}}{\partial x} - \frac{1}{\rho^2}\frac{\partial \rho}{\partial x}\rho_{\mathrm{NL}\pm} \Big)\langle \hat{\eta}\rangle dx'
$$
$$
= \int_{-\infty}^{\infty} \Big\{ \mp \alpha_\pm \Big[\frac{\rho_{\mathrm{NL}\pm}}{\rho} - \delta(x-x')\Big] \pm \beta_\pm \Big[\frac{\rho_{\mathrm{NL}\mp}}{\rho} - \delta(x-x')\Big] \Big\}\langle \hat{\eta}\rangle dx'. \quad (3.29)
$$

Here we have imported the source-field photon numbers $\hat{\eta}$ of Eq. (3.28) within the integrals by using delta function representations. In order to determine the damping and scattering coefficients $\alpha_\pm$ and $\beta_\pm$, we require

that the RTE model must be valid for arbitrary temperature distributions of the material described by the position-dependent source-field photon number $\langle \hat{\eta} \rangle$. This requirement is equivalent to the condition that the integrands on the left and right hand side of Eq. (3.29) must be equal at all positions $x$ and $x'$. Although it is not directly evident, one can find that the integrands on the left and right in Eq. (3.29) are linearly dependent functions of $x'$ for $x' \neq x$. This enables us to separate Eq. (3.29) into two linearly independent equations, one for $x = x'$ and one for $x \neq x'$. For $x = x'$, by setting the integrands on the left and right hand side of Eq. (3.30) equal, we obtain an equation

$$\frac{1}{\rho} \int_{x^-}^{x^+} \frac{\partial \rho_{\mathrm{NL}\pm}}{\partial x} dx' = \pm \alpha_\pm \mp \beta_\pm, \tag{3.30}$$

where $x^-$ and $x^+$ denote positions on the left and right infinitesimally close to $x$. For $x \neq x'$, we respectively obtain an equation

$$\frac{\partial \rho_{\mathrm{NL}\pm}}{\partial x} - \frac{1}{\rho} \frac{\partial \rho}{\partial x} \rho_{\mathrm{NL}\pm} = \mp \alpha_\pm \rho_{\mathrm{NL}\pm} \pm \beta_\pm \rho_{\mathrm{NL}\mp}. \tag{3.31}$$

The solutions of the pair of equations for $\alpha_\pm$ and $\beta_\pm$, formed by Eqs. (3.29) and (3.30), are given by

$$\alpha_\pm(x, \omega) = \frac{1}{2\rho\rho_{\mathrm{IF}}} \left( \frac{\partial \rho}{\partial x} \rho_{\mathrm{NL}\pm} - \rho \frac{\partial \rho_{\mathrm{NL}\pm}}{\partial x} - \rho_{\mathrm{NL}\mp} \int_{x^-}^{x^+} \frac{\partial \rho_{\mathrm{NL}\pm}}{\partial x} dx' \right), \tag{3.32}$$

$$\beta_\pm(x, \omega) = \frac{1}{2\rho\rho_{\mathrm{IF}}} \left( \frac{\partial \rho}{\partial x} \rho_{\mathrm{NL}\pm} - \rho \frac{\partial \rho_{\mathrm{NL}\pm}}{\partial x} - \rho_{\mathrm{NL}\pm} \int_{x^-}^{x^+} \frac{\partial \rho_{\mathrm{NL}\pm}}{\partial x} dx' \right). \tag{3.33}$$

These quantum optical light-matter interaction parameters fully capture the interference, emission, damping and scattering of propagating photons in stratified media. To include the corrections in the conventional RTE model, one only needs to replace the classical damping and scattering coefficients with the position-dependent parameters in Eqs. (3.32) and (3.33). The derived interference-exact RTE model is also expected to extend the useful range of interference-aware optical models from simple structures to full device level simulations.

*Solution of the RTE model*

In order to write the photon number as a solution of the RTE model in a general form, we first rewrite the RTE model in Eq. (3.28) as a matrix equation

$$\frac{d}{dx} \mathbf{n}(x, \omega) = -\boldsymbol{\alpha}(x, \omega)[\mathbf{n}(x, \omega) - \boldsymbol{\eta}(x, \omega)]. \tag{3.34}$$

Here we have written the photon numbers of the left and right propagating fields and source fields as vectors $\mathbf{n}(x, \omega) = [\langle \hat{n}_+(x, \omega) \rangle, \langle \hat{n}_-(x, \omega) \rangle]^T$

and $\boldsymbol{\eta}(x,\omega) = [\langle\hat{\eta}(x,\omega)\rangle, \langle\hat{\eta}(x,\omega)\rangle]^T$, and the damping and scattering coefficients have been incorporated in a matrix

$$\boldsymbol{\alpha}(x,\omega) = \begin{bmatrix} \alpha_+ & -\beta_+ \\ \beta_- & -\alpha_- \end{bmatrix}. \tag{3.35}$$

With the boundary condition $\mathbf{n}(x_0,\omega) = \mathbf{n}_0$ defined at $x = x_0$, the solution to Eq. (3.34) is then given by

$$\mathbf{n}(x,\omega) = e^{-\int_{x_0}^{x} \boldsymbol{\alpha}(x',\omega)\,dx'}\mathbf{n}_0 + \int_{x_0}^{x} e^{-\int_{x'}^{x} \boldsymbol{\alpha}(x'',\omega)\,dx''}\boldsymbol{\alpha}(x',\omega)\boldsymbol{\eta}(x',\omega)dx'. \tag{3.36}$$

The form of Eq. (3.36) is fully analogous with the solution of the conventional RTE model whose damping coefficients are here replaced by the matrix $\boldsymbol{\alpha}(x,\omega)$. The same applies to some representations of the conventional quantum optical IOF [118].

## 3.2 Coupled state description of the field and matter

This section reviews the coupled state description of the field and matter in a medium described in Publication VIII. In Sec. 3.2.1, we briefly present some background for the Abraham–Minkowski controversy of photon momentum in a medium as this controversy was one of the main motivations for the development of the coupled state description in this thesis. In Sec. 3.2.2, we review the MP quasiparticle picture, where we consider the light pulse as a coupled state between a single photon and matter, isolated from the rest of the medium, and apply only the conservation laws and the Lorentz invariance. In Sec. 3.2.3, we describe the corresponding OCD model that is based on Newton's equation of motion. The OCD model presents an alternative derivation of the main results obtained in the MP quasiparticle approach, and it also allows simulations of the predicted photon mass drag effect with realistic material parameters.

### 3.2.1 Abraham–Minkowski controversy

The quantum hypothesis by Max Planck in 1900 [122] related the energy $E$ of a photon to the frequency of light as $E = \hbar\omega$. Since then, the momentum of a photon propagating in vacuum has been known to be given by $p = \hbar\omega/c$. However, the momentum of light in a medium with refractive index $n$ has remained a subject of an extensive scientific controversy for more than a century [34–46, 123–132]. The controversy has culmi-
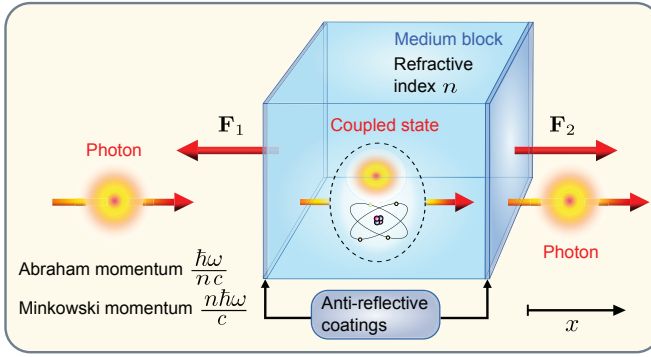
**Figure 3.1.** Schematic illustration of the problem of a photon propagating through a medium block having refractive index $n$. The photon emerges from vacuum on the left. Then it couples to the atoms of the medium block forming an MP quasiparticle, which propagates through the block. After penetrating the medium block, the photon continues to propagate in vacuum on the right. At the interfaces, the medium block experiences recoil forces $\mathbf{F}_1$ and $\mathbf{F}_2$ that depend on the total momentum of the MP in the medium. Figure adapted from Publication VIII.

nated in the difficulty to establish an unambiguous expression for the photon momentum and, in particular, in formulating a consistent theory to choose between the Abraham momentum $p_\mathrm{A} = \hbar\omega/(nc)$ [133, 134] and the Minkowski momentum $p_\mathrm{M} = n\hbar\omega/c$ [135]. Therefore, this momentum dilemma has become known as the Abraham–Minkowski controversy. The problem of the propagation of a light wave in a nondispersive medium is schematically illustrated in Fig. 3.1.

Neither the Abraham nor the Minkowski momentum has previously been proven to be fully consistent with the energy and momentum conservation laws, de Broglie hypothesis, Lorentz invariance, and available experimental data. To explain the controversy, it has been previously suggested that both forms of momenta are correct but describe different aspects of the momentum of light [37, 38]. In some other theoretical studies, the Abraham–Minkowski controversy has been reasoned to be resolved by arguing that the division of the total energy-momentum tensor into material and electromagnetic components would be completely arbitrary [36, 136, 137]. On the experimental side, several different setups have been introduced for the measurement of the momentum of light in a medium [138–149]. However, experimental results have been interpreted to be partly controversial, and therefore, they have not been able to conclusively resolve the controversy.

*Abraham model*

A simple derivation of the Abraham model of light can be presented by considering how the so-called Einstein's box thought experiment [150, 151] is traditionally applied to determine the momentum of a photon inside the medium. In this approach, the starting point is Newton's first law generalized to account for both the fields and particles [37]. This law is also known as the constant center of energy velocity (CEV) of an isolated system, such as the photon and the medium block in Fig. 3.1. The constant CEV for a system of a photon with energy $\hbar\omega$ and velocity $c$ initially in vacuum and a medium block with mass $M$ and energy $Mc^2$ initially at rest is argued to obey the equation

$$V_{\mathrm{CEV}} = \frac{\sum_i E_i v_i}{\sum_i E_i} = \frac{\hbar\omega c}{\hbar\omega + Mc^2} = \frac{\hbar\omega v + Mc^2 V}{\hbar\omega + Mc^2}. \tag{3.37}$$

Here the two forms on the right are written for the cases before and after the photon has entered the medium. It is assumed that inside the medium the initial photon energy $\hbar\omega$ propagates with velocity $v = c/n$ which results in the medium block obtaining a velocity $V$ to be determined from Eq. (3.37). From Eq. (3.37) we then obtain $\hbar\omega/c = \hbar\omega/(nc) + MV$ suggesting that the initial photon momentum $\hbar\omega/c$ in vacuum is split into the Abraham momentum of a photon in a medium equal to

$$p_{\mathrm{A}} = \frac{\hbar\omega}{nc} \tag{3.38}$$

and to the medium block momentum equal to $MV$. One might then conclude that the Abraham momentum would be the correct photon momentum in a medium and that the Minkowski momentum would thus violate Newton's first law [37].

*Minkowski model*

The simplest theoretical derivation of the Minkowski model is provided by the application of the de Broglie hypothesis to the state of a light wave in a medium. According to the de Broglie hypothesis, the momentum of a quantum state is related to the wavelength as

$$p = \frac{h}{\lambda}, \tag{3.39}$$

where $h$ is the (non-reduced) Planck constant and $\lambda$ is the wavelength. As the wavelength of light is very well known to be reduced in the medium as $\lambda = \lambda_0/n$, where $\lambda_0$ is the wavelength in vacuum, and $\lambda_0 = 2\pi c/\omega$,

we obtain that the momentum of light in the medium is given by the Minkowski formula as

$$p_{\mathrm{M}} = \frac{n\hbar\omega}{c}.$$
(3.40)

Therefore, one might conclude that the Minkowski momentum would be the quantum mechanically correct photon momentum in a medium. Thus, one might also conclude that there is a clear inconsistency between Newton's first law in Eq. (3.37) and the de Broglie hypothesis in Eq. (3.39). However, in Publication VIII, we show that this is not actually the case and there exists a unique and fully transparent resolution to the controversy.

### 3.2.2   Mass-polariton (MP) quasiparticle model

Next we review the MP quasiparticle model introduced in Publication VIII, where light quanta are described as MP quasiparticles that are formed by the coupled state of a photon and a mass displacement field associated with the photon. Due to the photon induced mass displacement propagating at speed $c/n$, the MP is also shown to have a rest mass. Since the MP does not involve a clear resonance with an internal excited state of the medium, the polariton term here has a meaning that fundamentally differs from its conventional use in the context of the exciton-polariton and the phonon-polariton quasiparticles.

As the consistent description of the propagation of a light field in a medium has appeared to be extremely difficult leading, e.g., to the Abraham–Minkowski controversy, we base the MP quasiparticle model on the most fundamental laws of energy and momentum provided by their conservation laws and the covariance principle of the special theory of relativity. The covariance condition in Eq. (2.26) clearly indicates that a photon with energy $\hbar\omega$ having either Abraham or Minkowski momentum propagating in a nondispersive medium cannot be covariantly described by a state with a zero rest mass. Therefore, we consider the possibility that the photon forms a new quasiparticle with a nonzero mass $\delta m$, consisting of the photon moving at speed $c/n$ and a photon induced mass displacement field that also propagates at speed $c/n$. This is equivalent to allowing that the medium is not perfectly rigid contrasting the typical assumption in previous works on the Abraham–Minkowski controversy. Therefore, our model allows the formation of a mass density wave (MDW), i.e., excess
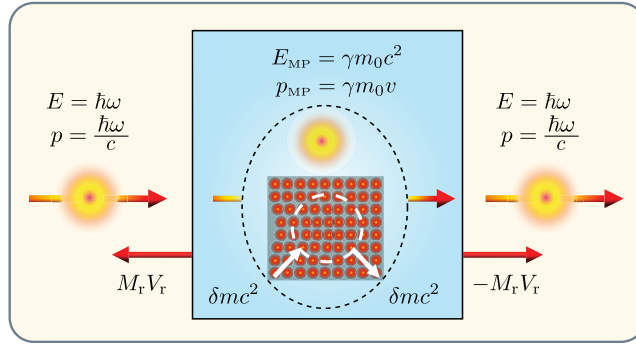
**Figure 3.2.** Schematic illustration of the energy and momentum transfer of the photon, the MP, and the medium block in the processes where the MP is created and destroyed. Inside the block, the mass energy is transferred as a MDW illustrated by the bending of the lattice planes. Figure adapted from Publication VIII.

mass density of the medium, which is associated with light as illustrated in Fig. 3.2.

Here, in the MP quasiparticle approach, we determine the value of $\delta m$ by requiring that the MP is described by a covariant state that enables the transfer of energy trough the medium at speed $v = c/n$. It is shown that the determination of $\delta m$ also determines the momentum of the MP. Consequently, the energy ratio $\delta m c^2 / \hbar\omega$ and the energy-momentum ratio $E/p$ of the MP are internal properties of the light wave. Separate interface forces in Fig. 3.1 are additionally needed to balance the possible momentum change between the photon momentum in vacuum and the momentum of the covariant MP state so that the total momentum is conserved. The related recoil energies and momenta at the interfaces are assumed to directly affect only thin material layers at the surface.

*Laboratory frame (L-frame)*

In L-frame, which is the initial rest frame of the medium block, the total energy of the MP in our model is given by $E_{\mathrm{MP}} = \hbar\omega + \delta m c^2$. It consists of the part $\hbar\omega$ describing the energy of the field including the potential energy of induced dipoles and the kinetic energy of MDW atoms, and the part $\delta m c^2$ related to the rest energy of $\delta m$ transferred as a MDW. It can be reasoned that, in the total energy of the MP in L-frame, all other contributions, but the mass energy $\delta m c^2$, have their origin in the field energy of the incoming photon. In any inertial frame, all this field energy can be exploited, for instance, in the resonance excitation of the medium atoms.

For example, the kinetic energy of $\delta m$ is included in the field energy $\hbar\omega$ as atoms are moved by the field–dipole forces following from the presence of the field. However, since $\delta m$ is not the mass of an isolated particle in vacuum but the mass carried by the MDW, where the total mass of contributing atoms is vastly larger than $\delta m$, the kinetic energy of $\delta m$ is negligible even though it is carried at the relativistic speed $v = c/n$ through the medium. In Publication VIII, this is reasoned by using the numerical results of the OCD model and also by using simple classical energy and momentum arguments.

*MP rest frame (R-frame)*

Next we transform the total L-frame energy of the MP, given by $E_{\text{MP}} = \hbar\omega + \delta m c^2$, to an inertial frame moving with the velocity $v'$ with respect to L-frame. Denoting the so far unknown momentum of the MP in L-frame by $p_{\text{MP}}$ and using the Lorentz transformation in Eqs. (2.22) and (2.23), we obtain the energy $E'_{\text{MP}}$ and momentum $p'_{\text{MP}}$ of the MP in the transformed frame as

$$E'_{\text{MP}} = \gamma'(E_{\text{MP}} - v'p_{\text{MP}}) = \gamma'(\hbar\omega - v'p_{\text{MP}}) + \gamma'\delta m c^2, \qquad (3.41)$$

$$p'_{\text{MP}} = \gamma'\left(p_{\text{MP}} - \frac{v'E_{\text{MP}}}{c^2}\right) = \gamma'\left(p_{\text{MP}} - \frac{v'\hbar\omega}{c^2} - v'\delta m\right). \qquad (3.42)$$

Here $\gamma'$ is the Lorentz factor corresponding to the velocity $v'$. In Eq. (3.41), the last term on the right presents the transformed rest energy of the MDW, while the first term $\hbar\omega' = \gamma'(\hbar\omega - v'p_{\text{MP}})$ originates from the field energy and it corresponds to the Doppler-shifted energy of a photon in a medium. According to the Doppler shift [152], the field energy becomes zero in the reference frame moving with the velocity of light in the medium. This condition is equivalent to the fact that photons do not have a rest mass. Therefore, setting $\hbar\omega' \longrightarrow 0$ in R-frame, where $v' = c/n$, one obtains

$$p_{\text{MP}} = \frac{n\hbar\omega}{c}. \qquad (3.43)$$

The Doppler shift has been used to justify the Minkowski momentum also earlier [37, 129]. However, in the earlier derivation, the Lorentz transformation in Eqs. (3.41) and (3.42) was not used, and thus, the transferred mass $\delta m$ carried by the MDW remained undetermined.

*Transferred mass carried by the MDW and the rest mass of the MP*

Since R-frame moves with the MP, the total momentum of the MP in R-frame is zero by definition. Therefore, inserting the momentum $p_{\text{MP}}$ of the

MP from Eq. (3.43) into Eq. (3.42) and setting $v' = c/n$, one obtains the transferred mass carried by the MDW as

$$\delta m = (n^2 - 1)\hbar\omega/c^2. \tag{3.44}$$

According to the special theory of relativity, the total energy of a particle or any structural system with rest mass $m_0$ in its rest frame can be written as $m_0 c^2$. Therefore, we denote the mass of the MP in R-frame by $m_0$ and call it the rest mass of the MP. Inserting $p_{\mathrm{MP}}$ and $\delta m$ from Eqs. (3.43) and (3.44) into Eq. (3.41) and setting $v' = c/n$, we can solve the rest mass of the MP as

$$m_0 = n\sqrt{n^2 - 1}\,\hbar\omega/c^2. \tag{3.45}$$

For the energy and momentum of the MP, one then obtains in L-frame

$$E_{\mathrm{MP}} = \gamma m_0 c^2 = n^2 \hbar\omega,$$
$$p_{\mathrm{MP}} = \gamma m_0 v = \frac{n\hbar\omega}{c}. \tag{3.46}$$

It can be directly observed that the energy and momentum of the MP in Eq. (3.46) and the rest mass in Eq. (3.45) fulfill the covariance condition in Eq. (2.26). Note that although knowing $\delta m$ is enough to understand the mass transfer associated with the MP, $m_0$ is useful for transparent understanding of the covariant MP state of light in a medium.

The rest mass of the MP, the transferred mass carried by the MDW, and the Minkowski form of the MP momentum were found to be direct consequences of the Lorentz transformation, Doppler shift, and the fundamental conservation laws of nature. This is in contrast with earlier explanations of the Minkowski momentum, where the transferred mass carried by the MDW has been neglected.

*Momenta of the field and matter parts of the MP*
The covariant energy-momentum ratio $E/p = c^2/v$ following from the Lorentz transformation in Eqs. (3.41)–(2.25) allows splitting the total MP momentum in Eq. (3.46) into parts corresponding to the electromagnetic energy $\hbar\omega$ and the MDW energy $\delta m c^2$. As a result, one obtains the field and MDW momenta given in L-frame by

$$p_{\mathrm{field}} = \frac{\hbar\omega}{nc},$$
$$p_{\mathrm{MDW}} = \left(n - \frac{1}{n}\right)\frac{\hbar\omega}{c}. \tag{3.47}$$

Therefore, one can observe that the field's share of the total MP momentum is of the Abraham form while the MDW's share is given by the difference of the Minkowski and Abraham momenta. However, due to the coupling, only the total momentum of the MP and the transferred mass are expected to be directly measurable.

*Einstein's box thought experiment revised*

Our results in Eqs. (3.45) and (3.46) show that the MP rest mass $m_0$ has not been taken properly into account in Einstein's box thought experiment discussed above. Accounting for the rest mass of the MP, we can write the constant CEV law in Eq. (3.37) before and after the photon has entered the medium as

$$V_{\text{CEV}} = \frac{\sum_i E_i v_i}{\sum_i E_i} = \frac{\hbar\omega c}{\hbar\omega + Mc^2} = \frac{\gamma m_0 c^2 v + M_{\text{r}} c^2 V_{\text{r}}}{\gamma m_0 c^2 + M_{\text{r}} c^2}, \qquad (3.48)$$

where $M_{\text{r}} = M - \delta m$ and $V_{\text{r}} = (1-n)\hbar\omega/(M_{\text{r}}c)$. The equality of the denominators corresponds to the conservation of energy and the equality of the numerators divided by $c^2$ corresponds to the momentum conservation. Equation (3.48) directly shows that the mass-polariton with the Minkowski momentum obeys the constant CEV motion and explains why earlier derivations of the Minkowski momentum assuming zero rest mass for the propagating light pulse lead to violation of the constant CEV motion [37, 38].

### 3.2.3 Optoelastic continuum dynamics (OCD)

*Newton's equation of motion and optoelastic forces*

Next we briefly review the essence of the OCD model that corresponds to the MP model above, but is an independent and complementary approach to the same problem of light propagation in a medium. In the OCD model introduced in Publication VIII, we apply Newtonian formulation of the continuum mechanics to show that the field–dipole forces give rise to the MDW, which propagates with the light field in a medium. The MDW effect disturbs the mass density of the medium from its equilibrium value $\rho_0$. Another related effect is the recoil effect, which exists only at material interfaces, where the refractive index changes. The total disturbed atomic mass density of the medium, in the OCD model, becomes $\rho_{\text{a}}(\mathbf{r}, t) = \rho_0 + \rho_{\text{rec}}(\mathbf{r}, t) + \rho_{\text{MDW}}(\mathbf{r}, t)$, where $\rho_{\text{rec}}(\mathbf{r}, t)$ is the mass density disturbance due to the recoil effect and $\rho_{\text{MDW}}(\mathbf{r}, t)$ is the mass density of

MDW. The mass density disturbances related to the recoil and MDW effects become spatially well separated after the light pulse has penetrated in the medium. While the recoil effect exists only at material interfaces, the MDW effect follows the light pulse inside the medium. As the velocities of atoms are nonrelativistic in the inertial reference frame where the medium is initially at rest, we can write Newton's equation of motion for the mass density of the medium as

$$\rho_{\mathrm{a}}(\mathbf{r},t)\frac{d^2 \boldsymbol{r}_{\mathrm{a}}(\mathbf{r},t)}{dt^2} = \mathbf{f}_{\mathrm{opt}}(\mathbf{r},t) + \mathbf{f}_{\mathrm{el}}(\mathbf{r},t), \tag{3.49}$$

where $\boldsymbol{r}_{\mathrm{a}}(\mathbf{r},t)$ is the atomic displacement field of the medium and $\mathbf{f}_{\mathrm{opt}}(\mathbf{r},t)$ and $\mathbf{f}_{\mathrm{el}}(\mathbf{r},t)$ are the optical and elastic force densities.

The optical force density $\mathbf{f}_{\mathrm{opt}}(\mathbf{r},t)$ has its origin in the interaction between the induced dipoles and the electromagnetic field. It has remained as a controversial topic related to the Abraham–Minkowski controversy [36, 40, 41, 149]. In the OCD model, we use the force density corresponding to the conventional Abraham model given by [41, 153]

$$\mathbf{f}_{\mathrm{opt}}(\mathbf{r},t) = -\frac{\varepsilon_0}{2}\mathbf{E}^2(\mathbf{r},t)\nabla n^2 + \frac{n^2-1}{c^2}\frac{\partial}{\partial t}\mathbf{S}(\mathbf{r},t). \tag{3.50}$$

The displacement of atoms from their equilibrium positions due to the optical force in Eq. (3.50) gives rise to the elastic force density $\mathbf{f}_{\mathrm{el}}(\mathbf{r},t)$ following from Hooke's law. In the simulations in Publication VIII, we assume a homogeneous isotropic elastic medium, in which case the stiffness tensor in Hooke's law has only two independent entries described in terms of the bulk modulus $B$ and the shear modulus $G$ [154]. The elastic force density is then given by [155]

$$\mathbf{f}_{\mathrm{el}}(\mathbf{r},t) = (B + \tfrac{4}{3}G)\nabla[\nabla \cdot \mathbf{r}_{\mathrm{a}}(\mathbf{r},t)] - G\nabla \times [\nabla \times \mathbf{r}_{\mathrm{a}}(\mathbf{r},t)]. \tag{3.51}$$

In the special case of non-viscous fluids, one could set the shear modulus $G$ to zero, in which case Eq. (3.51) is simplified so that only the first term remains.

In the OCD model, Newton's equation of motion in Eq. (3.49) with the optical and elastic force densities in Eqs. (3.50) and (3.51) can be solved by time integration using appropriate space and time discretization. To verify the correspondence with the MP quasiparticle model reviewed in Sec. 3.2.2, the OCD model has been applied to simulate the optical and elastic forces and the resulting mass and momentum transfer as a function of time when a Gaussian light pulse propagates through a diamond

crystal block in Publication VIII. The results of these simulations are re-
viewed in Sec. 4.3.

### 3.2.4  Comparison of the MP and OCD approaches

For the light pulse of energy $E_0 = N_0 \hbar \omega_0$, where $N_0$ is the number of
photons and $\omega_0$ is the central frequency of the pulse, the total mass carried
by the MDW can be written as

$$\delta M = \int \rho_{\text{MDW}}(\mathbf{r}, t) d^3 r = (n^2 - 1) N_0 \hbar \omega_0 / c^2. \qquad (3.52)$$

The integral expression is the result obtained from the OCD model of
Sec. 3.2.3 and the right hand side is the result obtained from the MP
quasiparticle model of Sec. 3.2.2. The total momentum of the coupled
state of the field and matter is a sum of the momenta of the field and the
MDW, and it is given by

$$\mathbf{p}_{\text{MP}} = \int \rho_0 \mathbf{v}_{\text{a}}(\mathbf{r}, t) d^3 r + \int \frac{\mathbf{S}(\mathbf{r}, t)}{c^2} d^3 r = \frac{n N_0 \hbar \omega_0}{c} \hat{\mathbf{x}}. \qquad (3.53)$$

The first term on the left is the MDW momentum and the second term is
the field momentum obtained from the OCD approach. On the right, we
have the momentum of the coupled state obtained from the MP quasipar-
ticle model. The splitting of the total momentum of the light pulse into the
field and MDW parts is given in the MP quasiparticle model by Eq. (3.47)
multiplied with the photon number.

In the simulations described in Publication VIII and reviewed in Sec.4.3,
it has been found that the MP quasiparticle and the OCD model results
agree within the numerical accuracy of the simulations. This complete
agreement between the MP and OCD approaches is only obtained if the
optical force density used in the OCD approach is of the Abraham form as
given in Eq. (3.50). Therefore, one can conclude that our results provide
significant support for the Abraham force density as the only form of the
optical force density in a nondispersive medium that is fully consistent
with the covariance principle.

# 4. Results and discussion

In this chapter, we review selected results obtained in this thesis. In Sec. 4.1, we present the results of Publication I, which applied the Wigner function formalism described in Sec. 2.2.4 to study the application of the photon creation and annihilation operators on an electromagnetic field in a way that leads to amplification of weak coherent fields in a probabilistic amplification approach. In Sec. 4.2, we present selected results obtained by applying the QFED formalism developed in Publications II–VII for one- and three-dimensional geometries also including plasmonic structures. After that, in Sec. 4.3, we describe the results of Publication VIII in which we applied the OCD model to simulate the dynamics of the medium atoms driven by the field–dipole forces of a light field propagating in a medium and the elastic forces that try to re-establish the mass equilibrium in the medium.

## 4.1  Noiseless amplification of weak coherent fields

It is well known that quantum states cannot be perfectly cloned or amplified without introducing some excess noise in the process. This no-cloning theorem formulated in 1982 [156, 157] has profound implications, e.g., in quantum computing. The result follows from the linear and unitary evolution of quantum mechanical states and it avoids the violation of Heisenberg's uncertainty principle. However, one can amplify signals without adding noise by relaxing the requirement of a deterministic operation. Experimental demonstrations of such probabilistic amplifiers for weak coherent fields have been reported, e.g., in Refs. [65, 66].

### 4.1.1  Amplification scheme

Nondeterministic amplifiers are usually based on adding and subtracting photons to and from the light field [158–161]. In experimental implementation, subtraction is typically performed using a beam splitter and a photodetector and addition using a heralded single-photon source, a beam splitter, and a photodetector [65–68]. In Publication I, we proposed a noiseless amplification scheme where, in contrast to previous works [65, 66], the energy required to amplify the signal did not originate from an external energy source, i.e., a single-photon source, but from the stochastic fluctuations in the field itself. The action of an ideal noiseless amplifier for coherent states can be described as $|\alpha_0\rangle \to |g\alpha_0\rangle$ where $\alpha_0$ is the initial field amplitude and $g$ is the gain of amplification. This operation cannot be implemented by commonly used deterministic amplifiers, but it can be approximated by using a probabilistic setup. Addition and subtraction of photons correspond to the application of the creation and annihilation operators $\hat{a}^\dagger$ and $\hat{a}$ to an arbitrary state of light.

It is previously known that the operator $\hat{G} = (g-2)\hat{a}^\dagger\hat{a} + \hat{a}\hat{a}^\dagger = (g-1)\hat{n} + 1$ is a good approximation of the action above for the ideal amplification process of weak coherent fields [162]. The nominal gain $g = 2$ is of particular interest since the operation $\hat{G}$ becomes a sequence of photon addition and subtraction as $\hat{G}_{g=2} = \hat{a}\hat{a}^\dagger$ [160]. The action of this transformation is evident since a weak coherent field is approximately described as $|\alpha\rangle \approx |0\rangle + \alpha|1\rangle$ and thus one has $\hat{a}\hat{a}^\dagger|\alpha\rangle \approx |0\rangle + 2\alpha|1\rangle$. An amplification scheme based on $\hat{G}_{g=2}$ was experimentally demonstrated by Zavatta *et al*. [65]. Since the coherent state is an eigenstate of the annihilation operator, the same outcome is also obtained by an operator $\hat{G}'_{g=2} = \hat{a}\hat{a}^\dagger\hat{a}$ implemented by the setup proposed in Publication I. This outcome is obvious since the additional annihilation operator conserves coherent states as its eigenstates.

In our scheme, introduced in Publication I and illustrated in Fig. 4.1, the setup by Zavatta *et al*. [65] using a single-photon source is replaced by a configuration where a single photon is first subtracted from the initial coherent field by a beam splitter and detected by a QND measurement which is followed by adding the photon back to the field by the second beam splitter. A successful photon addition occurs if no photons are detected at photodetector PD1. Finally, another photon is subtracted from
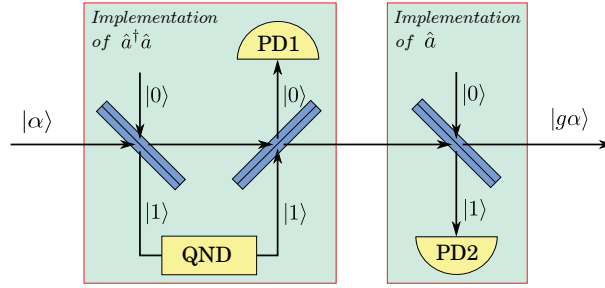
**Figure 4.1.** Schematic illustration of a setup for noiseless amplification of weak coherent fields as a realization of the operator $\hat{a}\hat{a}^\dagger\hat{a}$. In the successful operation, a single photon is first subtracted from the input field $|\alpha\rangle$ by the first beam splitter on the left. The subtracted photon is measured by a QND measurement after which it is added back to the field at the second beam splitter. Finally a photon is again subtracted from the field at the third beam splitter. The resulting output field of the setup is an amplified field $|g\alpha\rangle$. Figure adapted from Publication I.

the field at the third beam splitter. This subtracted photon is detected at photodetector PD2. The final output state resulting from these events is an amplified coherent state with high fidelity.

### 4.1.2  Output fields of successful amplification

The output fields of our setup have been calculated using the standard Wigner function formalism. For simplicity, in our calculations, we have made the usual assumption that the photodetectors of the setup in Fig. 4.1 are ideal. Also the QND measurement is assumed to be ideal since measurements made with QND detectors have been reported to produce single-photon Fock states with good accuracy [163–168]. The details of the analysis of how the initial coherent state propagates through the setup in the case of successful amplification are as follows.

The initial coherent field with a Wigner function $W_{\mathrm{coh}}$ is described by Eq. (2.49). The second input for the first beam splitter in our setup is a vacuum state $W_{|0\rangle\langle 0|}$ given by Eq. (2.50). The interference field after the first beam splitter is given by $W_{\mathrm{BS1}}$ following from Eqs. (2.44) and (2.45). The transmitted field $W_{\mathrm{BS1\to BS2}}$ after detecting one photon on the reflected field of the first beam splitter can be obtained by using Eq. 2.48 with $W' = W_{\mathrm{BS1}}$, $W_1' = W_{|1\rangle\langle 1|}$, and $W_2' = W_{\mathrm{BS1\to BS2}}$.

In the second beam splitter, a single photon with a Wigner function $W_{|1\rangle\langle 1|}$ emerging from the QND measurement is added back to the transmitted field $W_{\mathrm{BS1\to BS2}}$ of the first beam splitter. Therefore, using the in-

47

put fields $W_{\text{BS1}\rightarrow\text{BS2}}$ and $W_{|1\rangle\langle 1|}$ for the second beam splitter, the interference field $W_{\text{BS2}}$ after the second beam splitter can be again calculated by using Eqs. (2.44) and (2.45). The transmitted field $W_{\text{BS2}\rightarrow\text{BS3}}$ after detecting no photons on the reflected field of the second beam splitter is in turn obtained by using Eq. 2.48 with $W' = W_{\text{BS2}}$, $W'_1 = W_{|0\rangle\langle 0|}$, and $W'_2 = W_{\text{BS2}\rightarrow\text{BS3}}$.

The input fields for the third beam splitter are $W_{\text{BS2}\rightarrow\text{BS3}}$ and $W_{|0\rangle\langle 0|}$. The interference field $W_{\text{BS3}}$ after this last beam splitter again follows from Eqs. (2.44) and (2.45). At the third beam splitter, one photon is subtracted from the field. Thus the transmitted field of the third beam splitter, which is the total output field $W_{\text{out}}$ of the setup, is obtained by using Eq. 2.48 with $W' = W_{\text{BS3}}$, $W'_1 = W_{|1\rangle\langle 1|}$, and $W'_2 = W_{\text{out}}$.

The effective gain for the amplification setup can be defined as the ratio $g_{\text{eff}} = |\langle \hat{a}_{\text{out}} \rangle|/|\langle \hat{a}_{\text{in}} \rangle|$ [65] of the expectation values of the annihilation operators of the output and input fields calculated by using Eq. (2.42) or (2.43). Depending on the parameters of the setup, one can obtain effective gain values lower or equal to the nominal gain of $g = 2$. As a result, we obtained the effective gain, given by

$$g_{\text{eff}} = \frac{t_1 t_2 t_3 (2 + 4|t_1 t_2 t_3 \alpha|^2 + |t_1 t_2 t_3 \alpha|^4)}{1 + 3|t_1 t_2 t_3 \alpha|^2 + |t_1 t_2 t_3 \alpha|^4}, \tag{4.1}$$

where $t_i$, $i = 1, 2, 3$, are transmittivities of the beam splitters in the setup that are assumed to be real-valued and to obey the relations in Eq. (2.34).

In order to quantify how much the output state differs from an ideally amplified coherent state, we used Eq. (2.41) to calculate the fidelity of the successfully amplified field with respect to a coherent field $|g_{\text{eff}}\alpha\rangle$. This coherent field is obviously closer to the true amplified output state of the setup when compared to the ideal maximally amplified coherent field $|2\alpha\rangle$ corresponding to the nominal gain of $g = 2$. The result of our calculation is given by

$$F_{\text{eff}} = \frac{(1 + 2g_{\text{eff}} t_1 t_2 t_3 |\alpha|^2 + g_{\text{eff}}^2 t_1^2 t_2^2 t_3^2 |\alpha|^4) e^{-(g_{\text{eff}}^2 - t_1 t_2 t_3)^2 |\alpha|^2}}{1 + 3|t_1 t_2 t_3 \alpha|^2 + |t_1 t_2 t_3 \alpha|^4}. \tag{4.2}$$

In Fig. 4.2, we have plotted the effective gain, fidelity, and Wigner functions for the successfully amplified fields calculated by using Eqs. (4.1) and (4.2) above and the Wigner function formulas given in Sec. 2.2.4. The effective gain in Fig. 4.2(a) approaches the nominal gain value $g = 2$ for small values of the input field amplitude $|\alpha|$ and the beam splitter reflectivity $r$, which was chosen to be equal for all beam splitters in the setup.
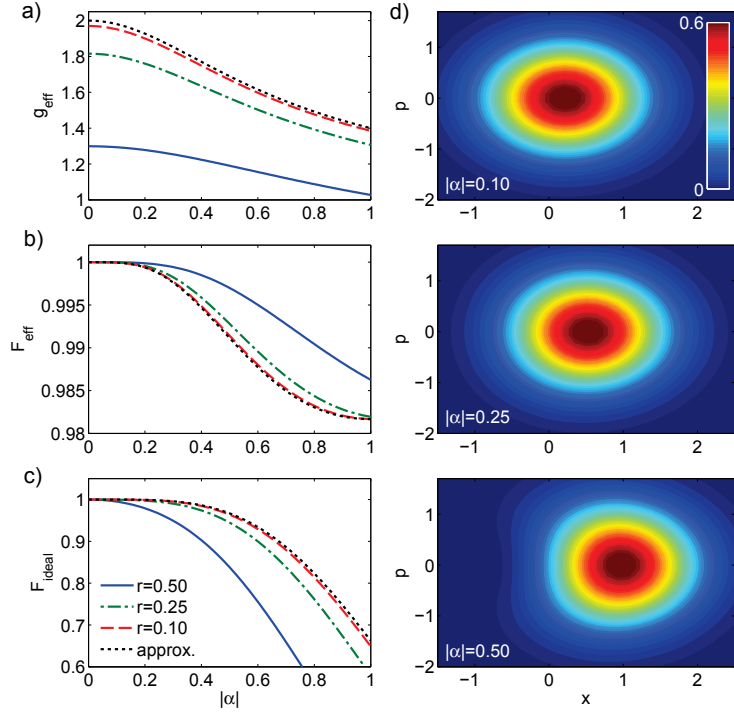
**Figure 4.2.** (a) Effective gain as a function of the input field amplitude calculated using beam splitter reflectivities $r = 0.1$ (red dashed line), $r = 0.25$ (green dash-dotted line), and $r = 0.5$ (blue solid line). The black dotted line corresponds to the low reflectivity approximation used by Zavatta *et al.* [65]. (b) Effective fidelity with respect to a coherent field $|g_{\mathrm{eff}}\alpha\rangle$ calculated using the three different beam splitter reflectivities and the low reflectivity approximation. (c) Fidelity with respect to an ideally amplified field $|2\alpha\rangle$ calculated for comparison with the results obtained by Zavatta *et al.* [65]. (d) Contour plots of the Wigner functions for three amplified output fields calculated using the coherent field input amplitudes $|\alpha| = 0.1$, $|\alpha| = 0.25$, and $|\alpha| = 0.5$ and the beam splitter reflectivity of $r = 0.4$. Figure adapted from Publication I.

Respectively, for larger values of the input field amplitude or the beam splitter reflectivity, the gain decreases. The effective fidelity $F_{\text{eff}}$ calculated with respect to a coherent field $|g_{\text{eff}}\alpha\rangle$ is shown in Fig. 4.2(b). One can observe that the effective fidelity decreases for increasing values of the input field amplitude. However, the decrease in the effective fidelity can be partly compensated by increasing the beam splitter reflectivity. For comparison with the results obtained by Zavatta *et al.* [65] using a setup including a specific single-photon source, in Fig. 4.2(c), we have plotted the fidelity calculated with respect to an ideal maximally amplified coherent field $|2\alpha\rangle$. As expected, this ideal fidelity $F_{\text{ideal}}$ decreases faster than the effective fidelity $F_{\text{eff}}$ in Fig. 4.2(b). This follows from the fact that $g_{\text{eff}}$ is reduced for stronger input fields. Therefore, $F_{\text{eff}}$ is a better measure for the quality of the successfully amplified output field. One can also observe, that $F_{\text{ideal}}$ decreases for increasing values of the beam splitter reflectivity whereas the opposite is true for $F_{\text{eff}}$. This is another result that follows from the reduction of the effective gain. The contour plots of the Wigner functions for the input field amplitudes $|\alpha| = 0.1$, $|\alpha| = 0.25$, and $|\alpha| = 0.50$ (with $|\alpha|^2$ being the photon number, i.e., essentially the intensity of the field) and for the beam splitter reflectivity $r = 0.4$ are shown in Fig. 4.2(d). It can be seen that, for small values of the input field amplitude, the output field is very close to a pure coherent field, but the deviation from a pure coherent state becomes apparent when the input field amplitude increases.

## 4.2 Quantized fluctuational electrodynamics

In Publications II–VI, we have applied the LTE approximation and the QFED formalism reviewed in Sec. 3.1 to describe field fluctuations, photon numbers, densities of states, Poynting vector, and thermal balance in stratified media at non-equilibrium conditions. Here we concentrate on the selected key results of these publications regarding the position-dependent photon numbers which, in contrast to the field quantities, have not been previously defined in the classical FED framework. Section 4.2.1 reviews the representation of the dyadic Green's functions for stratified media. In Sec. 4.2.2, we describe selected one- and three-dimensional results obtained by using our position-dependent photon-number concept. The results related to the division of the photon number into parts prop-

agating in different directions have been described in Sec. 4.2.3. Finally, the damping and scattering coefficients in the quantum optical RTE are discussed in Sec. 4.2.4.

### 4.2.1 Green's functions for stratified media

In order to use the formulas of Sec. 3.1 for practical modeling tasks, the Green's functions must be computed for the specific geometry. In our case, we have applied the QFED formalism to stratified media, for which it is convenient to use the plane-wave representation for the dyadic Green's functions. In this representation, a point in space is denoted in the Cartesian basis $(\hat{\mathbf{x}}, \hat{\mathbf{y}}, \hat{\mathbf{z}})$ by $\mathbf{r} = x\hat{\mathbf{x}} + y\hat{\mathbf{y}} + z\hat{\mathbf{z}} = \mathbf{R} + z\hat{\mathbf{z}}$, where $\mathbf{R} = x\hat{\mathbf{x}} + y\hat{\mathbf{y}}$ is the component of the position vector $\mathbf{r}$ in the $x$-$y$ plane. Correspondingly, a wave vector of a plane wave is denoted by $\mathbf{k} = \mathbf{K} + k_z \operatorname{sgn}(z - z')\hat{\mathbf{z}}$, where $\mathbf{K}$ is the in-plane component and $k_z$ is given by $k_z = \sqrt{k^2 - K^2}$. Here $k = nk_0 = k_{\mathrm{r}} + ik_{\mathrm{i}}$ is the wavenumber whose real and imaginary parts are denoted by $k_{\mathrm{r}}$ and $k_{\mathrm{i}}$ and the square root of a complex number has been defined so that the imaginary part is non-negative as $k_{z,\mathrm{i}} \geq 0$.

The adopted plane-wave representation is convenient since, in the $x$-$y$ plane, the dyadic Green's functions of stratified media depend only on the relative in-plane coordinate $\mathbf{R} - \mathbf{R}'$. Therefore, the dyadic Green's functions $\overset{\leftrightarrow}{\mathbf{G}}_{jk}(\mathbf{r}, \omega, \mathbf{r}')$, with $j, k \in \{\mathrm{e}, \mathrm{m}\}$, can be written as [169, 170]

$$
\begin{aligned}
&\overset{\leftrightarrow}{\mathbf{G}}_{jk}(\mathbf{r}, \omega, \mathbf{r}') \\
&= \frac{1}{4\pi^2} \int \overset{\leftrightarrow}{\mathbf{R}}{}^{\mathrm{T}} \overset{\leftrightarrow}{\mathbf{g}}_{jk}(z, K, \omega, z') \overset{\leftrightarrow}{\mathbf{R}} e^{i\mathbf{K}\cdot(\mathbf{R}-\mathbf{R}')} d^2 K.
\end{aligned} \tag{4.3}
$$

The terms $\overset{\leftrightarrow}{\mathbf{R}}{}^{\mathrm{T}} \overset{\leftrightarrow}{\mathbf{g}}_{jk}(z, K, \omega, z') \overset{\leftrightarrow}{\mathbf{R}}$ in Eq. (4.3) are the Fourier transforms of $\overset{\leftrightarrow}{\mathbf{G}}_{jk}(\mathbf{r}, \omega, \mathbf{r}')$ with respect to the in-plane position coordinate. The dyadic plane-wave Greens functions $\overset{\leftrightarrow}{\mathbf{g}}_{jk}(z, K, \omega, z')$ are calculated using standard techniques in a coordinate system where the in-plane components of the field sources are perpendicular and parallel to $\mathbf{K}$. The rotation matrix $\overset{\leftrightarrow}{\mathbf{R}}$ is used to return this convention of direction back to the coordinate system where the direction of the field sources does not depend on $\mathbf{K}$.

### 4.2.2 Photon numbers and densities of states

The physical implications of the position-dependent photon-number concepts of the QFED framework reviewed earlier in Sec. 3.1 have been investigated in stratified media in the case of normal incidence in Publications

II and III and in the case of general incidence in Publication VI. When studying the case of normal incidence, we separately examine the electric and magnetic field contributions while, in the general case, we restrict our studies to the quantities related to the total electromagnetic field.

*Normal incidence*

First, we present selected results obtained for normal incidence in Publication III. As the photon-number expectation values for thermal fields are relatively small and depend strongly on the frequency, it was found convenient to illustrate the results by using effective field temperatures defined in terms of the photon-number expectation values using the inverted Bose–Einstein distribution as

$$T_{\text{eff},j}(x,\omega) = \frac{\hbar\omega}{k_{\text{B}} \ln[1 + 1/\langle \hat{n}_j(x,\omega)\rangle]}. \tag{4.4}$$

We studied the properties of these effective field temperatures and the corresponding electric and magnetic LDOSs in the geometry of a $10$-$\mu$m-wide vacuum cavity formed between two semi-infinite media with refractive indices $n_1 = 1.5 + 0.3i$ and $n_2 = 2.5 + 0.5i$. The temperatures of these media acting as thermal reservoirs are $T_1 = 400$ K and $T_2 = 300$ K.

Figure 4.3 presents the LDOSs of the electric, magnetic, and total electromagnetic fields and the corresponding effective field temperatures as functions of the position and frequency. The electric and magnetic LDOSs in Figs. 4.3(a) and 4.3(b) clearly oscillate in the vacuum cavity and saturate to constant values in the reservoir media far from the interfaces. This is due to the formation of standing waves as a result of the interference. The oscillations of the electric and magnetic LDOSs inside the cavity were found to be strongest at resonant energies $\hbar\omega = 0.056$ eV, $\hbar\omega = 0.118$ eV, and $\hbar\omega = 0.180$ eV corresponding to the wavelengths $\lambda_0 = 22.1$ $\mu$m, $\lambda_0 = 10.5$ $\mu$m, and $\lambda_0 = 6.89$ $\mu$m. The oscillations in the electric and magnetic LDOSs manifest the well-known electric Purcell effect [171] and the corresponding magnetic effect. These effects are related to the position-dependent field–matter coupling strengths of particles placed in the cavity. The peaks in the electric LDOS coincide the minima in the magnetic LDOS and vice versa. In contrast to the electric LDOS, the magnetic LDOS reaches its maximum values within the semi-infinite media due to the low finesse cavity and different dependence on the refractive index. As a linear combination of the electric and magnetic LDOSs, the total electromagnetic LDOS in Fig. 4.3(c) is constant with respect to position
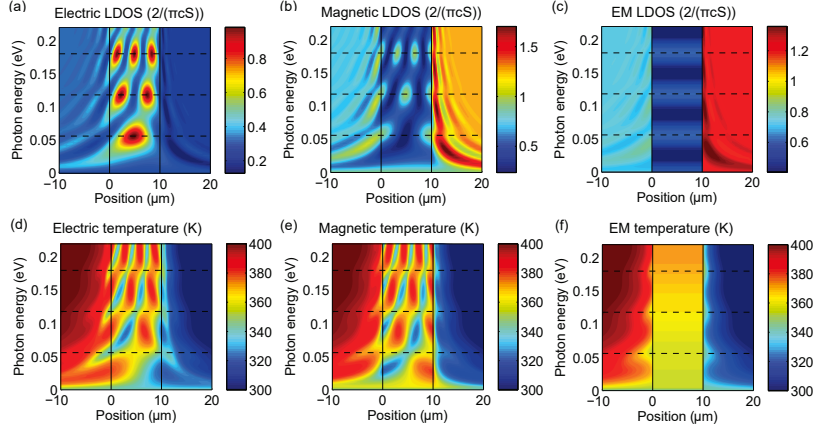
**Figure 4.3.** (a) Electric LDOS, (b) magnetic LDOS, (c) total electromagnetic LDOS, (d) electric field temperature, (e) magnetic field temperature, and (f) total electromagnetic field temperature in the cavity geometry formed by two lossy media with refractive indices $n_1 = 1.5 + 0.3i$ and $n_2 = 2.5 + 0.5i$ at temperatures 400 and 300 K separated by a 10-$\mu$m-wide vacuum gap. The vertical solid lines denote the cavity boundaries and the horizontal dashed lines denote resonant energies of the cavity. The LDOSs are given in units of $2/(\pi c S)$. Figure adapted from Publication III.

inside the cavity. However, the total electromagnetic LDOS is position-dependent and oscillatory inside the reservoir media since the oscillations of the electric and magnetic LDOSs do not cancel each other due to the existence of bound states related to the material polarizability.

The effective field temperatures defined using Eq. (4.4) are plotted for the electric and magnetic fields in Figs. 4.3(d) and 4.3(e). These effective field temperatures are strongly position dependent as they oscillate both in vacuum and near the interfaces inside the reservoir media. These position dependencies originate from the nonuniform coupling to the thermal reservoirs. Deep inside the reservoir media, the oscillations are then damped and the effective electric and magnetic field temperatures saturate to the reservoir temperatures. This damping depends on the photon energy and the absorptivity of the material taking place in a distance of the order of 10 $\mu$m in our example structure. The total electromagnetic field temperature is plotted in Fig. 4.3(f). As the total electromagnetic LDOS in Fig. 4.3(c), it is also constant with respect to position inside the cavity. One can also notice that the changes of the total electromagnetic field temperature near material interfaces are always monotonic with respect to position, which is an expected result for the photon number of the total electromagnetic field.
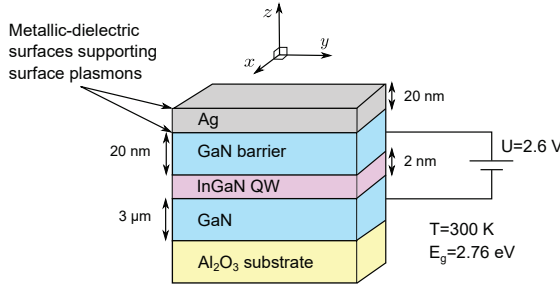
**Figure 4.4.** Schematic illustration of the studied Ag/GaN/In$_{0.15}$Ga$_{0.85}$N/GaN/Al$_2$O$_3$ heterostructure. The band gap of the light emitting In$_{0.15}$Ga$_{0.85}$N QW is $E_g = 2.76$ eV and the excitation of the QW corresponds to an applied voltage of $U = 2.6$ V. The background temperature of the materials and the radiation background is $T = 300$ K. Note that this figure is not to scale. Figure adapted from Publication VI.

*General incidence*

Next we present the results obtained by applying the QFED formalism to the case of general incidence in a layered structure as presented in Publication VI. In contrast to the case of normal incidence above, the description of plasmonic resonances is naturally included in the description in the general case. Therefore, it was of interest to use QFED to the study of the contribution of the evanescent SP modes to the position-dependent LDOSs and the effective-field temperatures in an example plasmonic multilayer structure, which had recently been of experimental and theoretical interest [172, 173]. This application also demonstrates the usefulness of the QFED method to the description of photon numbers and effective field temperatures in realistic three-dimensional layered structures.

The studied light-emitting Ag/GaN/In$_{0.15}$Ga$_{0.85}$N/GaN/Al$_2$O$_3$ multilayer structure is illustrated in Fig. 4.4. The light emitted from this structure is generated at the 2-nm In$_{0.15}$Ga$_{0.85}$N QW which has a band gap of $E_g = 2.76$ eV ($\lambda = 450$ nm). This emitter layer is deposited 20 nm below the 20-nm silver layer which supports SP modes. The whole structure is deposited on top of a sapphire substrate. In our QFED calculations, we used the frequency-dependent refractive indices of the materials taken from literature. The refractive indices of GaN and InN were taken from Refs. [174–179]. Based on the refractive index values of GaN and InN, the refractive index of In$_{0.15}$Ga$_{0.85}$N was deduced by using Vegard's law. The refractive index of silver was in turn calculated by using the Drude model with plasma frequency $\omega_\mathrm{p} = 9.04$ eV/$\hbar$ and damping frequency $\omega_\tau = 0.02125$ eV/$\hbar$ taken from Ref. [180]. The refractive index of sapphire substrate

was taken from Ref. [181].

In the QFED calculations, we compared the emission of the QW in two cases. In the first case, the QW was assumed to be thermally excited to temperature $T_{\text{ex}} = 350$ K and, in the second case, the QW was assumed to be electrically or optically excited to a state corresponding to a direct excitation by a $U = 2.6$ V voltage source. The background temperature of the materials was assumed to be $T = 300$ K meaning that all materials emit thermal radiation corresponding to this background temperature. The thermal radiation of the background materials and the radiation of a thermally excited QW were modeled by using the source-field photon-number expectation values given by the Bose–Einstein distribution as $\langle \hat{\eta}_{\text{bg}} \rangle = 1/(e^{\hbar\omega/(k_{\text{B}}T)} - 1)$ and $\langle \hat{\eta}_{\text{QW}} \rangle = 1/(e^{\hbar\omega/(k_{\text{B}}T_{\text{ex}})} - 1)$. This also corresponds to applying the LTE approximation described in Sec. 3.1.1. In the case of electrical or optical excitation, the source-field photon number of the QW was modeled using $\langle \hat{\eta}_{\text{QW}} \rangle = 1/(e^{(\hbar\omega - eU)/(k_{\text{B}}T)} - 1)$ for photon energies above the band gap, $\hbar\omega \geq E_g$, and the background value $\langle \hat{\eta}_{\text{bg}} \rangle = 1/(e^{\hbar\omega/(k_{\text{B}}T)} - 1)$ for photon energies below the band gap, $\hbar\omega \leq E_g$ [182]. The effective source-field temperature of the electrically or optically excited QW, which is calculated from the source-field photon number by using the inverted Bose–Einstein distribution in Eq. (4.4), ranges from $5175$ K to $625$ K as the photon energy ranges from $2.76$ to $5$ eV. Thus, the values of $\langle \hat{\eta}_{\text{bg}} \rangle$ in the case of electrical or optical excitation above the band gap are very large in comparison with the photon-number values of the thermal background or the thermally excited QW.

Figure 4.5(a) presents the base-10 logarithm of the total electromagnetic LDOS for photon energy $\hbar\omega = E_g + k_{\text{B}}T = 2.786$ eV plotted as a function of position and the in-plane component of the wave vector. The leftmost material is the sapphire substrate while the rightmost material is air. The light cones of the materials are defined by the values of the in-plane component of the wave vector satisfying $K < n_{\text{r}}k_0$, where $n_{\text{r}}$ is the real part of the refractive index of the respective material. The light cones of sapphire, GaN, and air are clearly visible in the LDOS and denoted by the horizontal dashed lines. The LDOS is also slightly elevated beyond the material interfaces due to the evanescent fields. The interference patterns resulting from the guided modes in the GaN layer between the light cones of GaN and sapphire with $1.78 < K/k_0 < 2.51$ can also be seen in the figure. The large LDOS values near $z = 0$ $\mu$m and $K/k_0 = 5.0$, seen as the
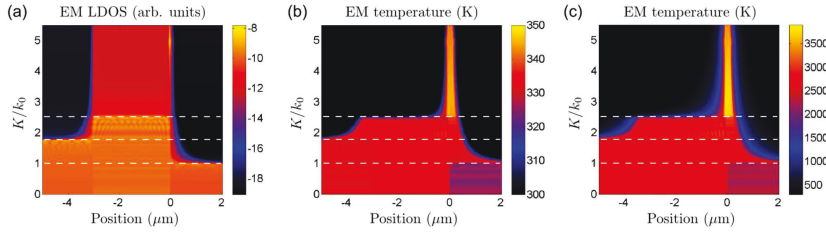
**Figure 4.5.** (a) The base-10 logarithm of the total electromagnetic LDOS, (b) the effective temperature of the total electromagnetic field in the case of a thermally excited QW, and (c) the corresponding effective field temperature calculated for an electrically or optically excited QW, where the excitation corresponds to the application of a bias voltage of $U = 2.6$ V. The plots are done for photon energy $\hbar\omega = E_g + k_B T = 2.786$ eV as a function of position and the normalized in-plane component $K/k_0$ of the wave vector. The position of the Ag/air interface is fixed to $z = 0$. The light cones of GaN, sapphire, and air are represented by the white dashed lines. Figure adapted from Publication VI.

yellow region in the plot, are associated with the GaN/Ag SP resonance. The air/Ag SP resonance is located near $z = 0$ $\mu$m and $K/k_0 = 1.0$, but it is not clearly visible in the figure.

Figure 4.5(b) presents the effective field temperature of the total electromagnetic field in the case of a thermally excited QW calculated from the photon number by using Eq. (4.4). At high values of $K$, the effective field temperature approaches the source field temperature that is $T_{ex} = 350$ K in the narrow In$_{0.15}$Ga$_{0.85}$N layer located slightly left from $z = 0$ $\mu$m and $T = 300$ K in other layers. Resembling the LDOS in Fig. 4.5(a), the light cones of the materials are also visible in the effective field temperatures. However, one can see that the patterns related to the evanescent fields near the material interfaces extend farther from the interfaces. The corresponding effective field temperature in the case of an electrically or optically excited QW is shown in Fig. 4.5(c). As expected, the values of this effective field temperature are significantly higher than those in the case of a thermally excited QW in Fig. 4.5(b). Otherwise, the effective field temperatures in Figs. 4.5(b) and 4.5(c) resemble each other.

Figures 4.6(a), 4.6(b), and 4.6(c) show the base-10 logarithm of the total electromagnetic LDOS as a function of the photon energy and the in-plane component of the wave vector in the QW, in air at 1 nm above the structure, and in air at 1 $\mu$m above the structure, respectively. The GaN/Ag SP resonance and GaN guided modes corresponding to the Fabry–Pérot resonances of the cavity are clearly visible in Figs. 4.6(a) and 4.6(b). Ag/air SP resonance can be seen above the light cone of air in Fig. 4.6(b). The
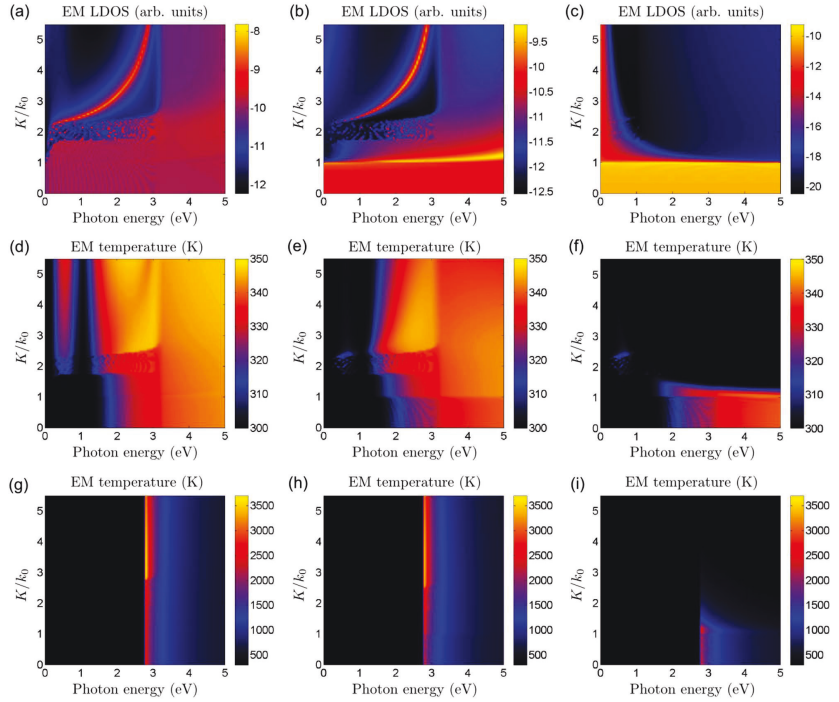
**Figure 4.6.** The base-10 logarithm of the total electromagnetic LDOS as a function of photon energy and the normalized in-plane component $K/k_0$ of the wave vector (a) in the QW, (b) in air at 1 nm above the surface, and (c) in air at 1 $\mu$m above the Ag/air interface. (d), (e), and (f) The effective temperatures of the total electromagnetic field at the corresponding positions in the case of a thermally excited QW. (g), (h), and (i) The corresponding effective field temperatures calculated for an electrically or optically excited QW, where the excitation corresponds to the application of a bias voltage of $U = 2.6$ V. Figure adapted from Publication VI.

resonances can be seen to disappear at photon energies above $3$ eV for which GaN becomes absorptive. At $1\ \mu$m above the structure, the LDOS in Fig. 4.6(c) mainly consists of the propagating modes in the light cone of air. Only a small contribution of the evanescent fields is visible at low photon energies.

Figures 4.6(d), 4.6(e), and 4.6(f) show the effective field temperatures corresponding to the LDOSs in Figs. 4.6(a), 4.6(b), and 4.6(c) for the case of a thermally excited QW. The InGaN QW becomes nearly transparent at low frequencies, and thus, the effective field temperatures reach the background temperature in the limit of low frequencies. The peak in the emissivity near $\hbar\omega = 0.5$ eV follows from the peak in the infrared absorption coefficient of the QW [179]. Due to the evanescent fields, the effective field temperatures in Figs. 4.6(d), 4.6(e) deviate from the background temperature at $K$ values above the cone lines of the materials. However, at very large $K$ values, the effective field temperatures reach the source-field temperature of the respective material layer as seen in Fig. 4.6(f). The same behavior is present in the case of Figs. 4.6(d) and 4.6(e) but it is not visible in the scale of these figures. When the distance to the QW becomes larger, the contribution of the evanescent fields is reduced and the effective field temperatures are mainly contributed by the propagating modes below the cone line of air as seen in Fig. 4.6(f).

Figures 4.6(g), 4.6(h), and 4.6(i) show the corresponding effective field temperatures calculated in the case of an electrically or optically excited QW. As expected, the emission starts to deviate from the background temperature when the photon energy exceeds the band gap and again decreases to the background temperature at high frequencies well above the band gap. The effective field temperature is also seen to increase as a function of the optical confinement: In the case of Fig. 4.6(g), inside the QW for the photon energy $\hbar\omega = E_g + k_{\mathrm{B}}T = 2.786$ eV, the evanescent InGaN modes reach effective field temperatures as high as $T_{\mathrm{eff}} \approx 3500$ K, whereas the modes extending into the light cone of GaN have $T_{\mathrm{eff}} \approx 2700$ K, and the modes bound to the light cone of air reach $T_{\mathrm{eff}} \approx 2200$ K. The values of the effective field temperatures are somewhat lower at $1$ nm above the structure as presented in Fig. 4.6(h) and much lower when the distance is increased to $1\ \mu$m as presented in Fig. 4.6(i). This mainly follows from the attenuation of the evanescent fields related to the increased distance to the QW.
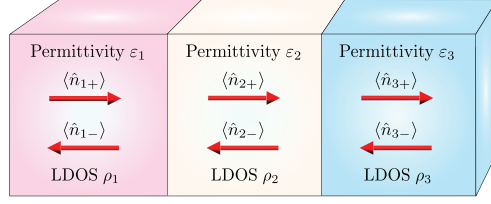
**Figure 4.7.** Illustration of an optical cavity that consists of three homogeneous dielectric layers with different permittivities and LDOSs. The left and right propagating field photon-number expectation values $\langle \hat{n}_+ \rangle$ and $\langle \hat{n}_- \rangle$ are calculated in each layer. Figure adapted from Publication IV.

### 4.2.3 Left and right propagating fields

In Publication IV, we presented how to separate the fields and photon numbers into parts propagating in different directions in interfering structures as reviewed in Sec. 3.1.6. Below, we discuss the application of these concepts to lossy and lossless example cavity structures described in Publication IV. The photon numbers in an optical cavity structure consisting of three homogeneous dielectric layers with permittivities $\varepsilon_1$, $\varepsilon_2$, and $\varepsilon_3$ are illustrated in Fig. 4.7.

*Lossless cavity*

First, we consider the case of a lossless cavity, where the left and right propagating photon numbers are piecewise constant and only depend on the left and right input field photon numbers $\langle \hat{n}_{1+} \rangle$ and $\langle \hat{n}_{3-} \rangle$ and the width and materials of the cavity and cavity walls. In the left and right semi-infinite media and inside the cavity, the propagating photon numbers can be written as

$$
\begin{aligned}
\langle \hat{n}_{1-} \rangle &= |\mathcal{R}_1|^2 \langle \hat{n}_{1+} \rangle + \sqrt{\varepsilon_1/\varepsilon_3}\, |\mathcal{T}_1' \mathcal{T}_2'|^2 \langle \hat{n}_{3-} \rangle, \\
\langle \hat{n}_{2+} \rangle &= \frac{\sqrt{\varepsilon_2/\varepsilon_1}\, |\mathcal{T}_1|^2 \langle \hat{n}_{1+} \rangle + \sqrt{\varepsilon_2/\varepsilon_3}\, |\mathcal{T}_2' \mathcal{R}_1'|^2 \langle \hat{n}_{3-} \rangle}{\mathrm{Re}(1 + 2\mathcal{R}_1' \mathcal{R}_2 \nu_2 e^{2ik_2 d_2})}, \\
\langle \hat{n}_{2-} \rangle &= \frac{\sqrt{\varepsilon_2/\varepsilon_1}\, |\mathcal{T}_1 \mathcal{R}_2|^2 \langle \hat{n}_{1+} \rangle + \sqrt{\varepsilon_2/\varepsilon_3}\, |\mathcal{T}_2'|^2 \langle \hat{n}_{3-} \rangle}{\mathrm{Re}(1 + 2\mathcal{R}_1' \mathcal{R}_2 \nu_2 e^{2ik_2 d_2})}, \\
\langle \hat{n}_{3+} \rangle &= \sqrt{\varepsilon_3/\varepsilon_1}\, |\mathcal{T}_1 \mathcal{T}_2|^2 \langle \hat{n}_{1+} \rangle + |\mathcal{R}_2'|^2 \langle \hat{n}_{3-} \rangle, \qquad\qquad (4.5)
\end{aligned}
$$

where $d_2$ is the thickness of the cavity, $k_2$ is the wave number in the cavity, $\nu_2 = 1/(1 + r_1 r_2 e^{2ik_2 d_2})$, $\mathcal{R}_1 = (r_1 + r_2 e^{2ik_2 d_2})\nu_2$, $\mathcal{R}_2 = r_2$, $\mathcal{T}_1 = t_1 \nu_2$, $\mathcal{T}_2 = t_2$, $\mathcal{R}_1' = r_1'$, $\mathcal{R}_2' = (r_2' + r_1' e^{2ik_2 d_2})\nu_2$, $\mathcal{T}_1' = t_1'$, and $\mathcal{T}_2' = t_2' \nu_2$ with the single-interface Fresnel reflection and transmission coefficients, which are given for left incidence by $r_i$ and $t_i$, $i \in \{1, 2\}$. The primed reflection coefficients
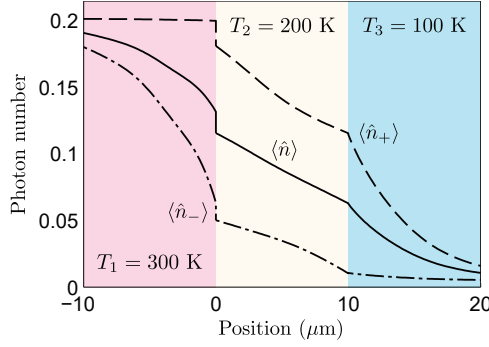
**Figure 4.8.** Left and right propagating photon numbers $\langle \hat{n}_- \rangle$ and $\langle \hat{n}_+ \rangle$ and the total photon number $\langle \hat{n} \rangle$ in the vicinity of a lossy cavity at the first cavity resonance $\hbar\omega = 0.046$ eV ($\lambda = 26.9$ $\mu$m). The refractive indices of the media from left to right are $n_1 = 2.5 + 0.4i$, $n_2 = 1.2 + 0.2i$, and $n_3 = 1.5 + 0.5i$, and the source-field temperatures are $T_1 = 300$ K, $T_2 = 200$ K, and $T_3 = 100$ K. Figure adapted from Publication IV.

are those for right incidence. It can be observed that the photon-number values inside the cavity and at the outputs in Eq. (4.5) are always between the input field photon numbers, which ensures that all photon numbers are equal in global thermal equilibrium and photons do not, e.g., accumulate inside the cavity.

*Lossy cavity*

In contrast to the case of a lossless cavity described above, in lossy structures, the photon numbers are no longer piecewise constant as all material points can act as field sources or drains through the position-dependent source field. In Publication IV, we have illustrated this by investigating the photon numbers in a lossy dielectric cavity structure, where the refractive indices of the media from left to right are $n_1 = 2.5 + 0.4i$, $n_2 = 1.2 + 0.2i$, and $n_3 = 1.5 + 0.5i$, The temperatures of medium layers are $T_1 = 300$ K, $T_2 = 200$ K, and $T_3 = 100$ K, respectively. They correspond to steady-state photon numbers $0.20$, $0.074$, and $0.0048$.

Figure 4.8 presents the total, right propagating, and left propagating photon numbers $\langle \hat{n} \rangle$, $\langle \hat{n}_+ \rangle$, and $\langle \hat{n}_- \rangle$ as a function of position at the first resonant energy of the cavity, given by $\hbar\omega = 0.046$ eV ($\lambda = 26.9$ $\mu$m). Due to the highest source-field temperature on the left, the photon numbers are highest on the left layer and decrease towards the right layer with lowest source-field temperature. The discontinuities of photon numbers at interfaces follow from reflections, while the decay inside the cavity and

near the interfaces is due to thermalization. On the left and right, the photon numbers eventually reach the source field temperature far from the cavity. The total photon number can also be seen to be equal to the average of the left and right propagating photon numbers. This is an expected result, since the photon number describes the average photon number in the collection of optical modes under study.

### 4.2.4 Quantum optical radiative transfer equation

In Publication VII, we developed the interference-exact quantum optical RTE model discussed in Sec. 3.1.7. Here we review the application of this model to a homogeneous space, a single-interface geometry, and a two-interface resonator, as also presented in Publication VII.

*Homogeneous space*

The damping and scattering coefficients in Eqs. (3.32) and Eq. (3.33) are in general position-dependent. Naturally, there is no position dependence in the case of a homogeneous space where the damping and scattering coefficients are constant and separately equal for fields that propagate in different directions. Using the Green's function representation of the densities of states, the damping and scattering coefficients of our RTE model in a homogeneous space become

$$
\begin{aligned}
\alpha_{\pm,\sigma} &= k_{z,\mathrm{i}}(\psi_\sigma + \psi_\sigma^{-1}), \\
\beta_{\pm,\sigma} &= k_{z,\mathrm{i}}(\psi_\sigma - \psi_\sigma^{-1}),
\end{aligned}
\tag{4.6}
$$

where the subscript $\sigma \in \{\mathrm{TE}, \mathrm{TM}\}$ denotes the TE and TM polarizations and the parameter $\psi_\sigma$ is given for the TE and TM polarizations by

$$
\psi_{\mathrm{TE}} = \frac{|k|^2 + |k_z|^2 + K^2}{2|\mu|k_{\mathrm{r}}\mathrm{Re}(k_z/\mu)}, \qquad \psi_{\mathrm{TM}} = \frac{|k|^2 + |k_z|^2 + K^2}{2|\varepsilon|k_{\mathrm{r}}\mathrm{Re}(k_z/\varepsilon)}.
\tag{4.7}
$$

In any homogeneous lossless medium, the RTE coefficients in Eq. (4.6) are all zero for propagating fields, which follows from the imaginary part $k_{z,\mathrm{i}} = 0$ of the wave vector $z$-component. Instead, in lossy media, these coefficients are typically positive and $\alpha_{\pm,\sigma}$ are larger than $\beta_{\pm,\sigma}$. In the case of normal incidence with $K = 0$, the RTE coefficients for the TE and TM polarizations are equal as expected. In a purely dielectric medium with $n = \sqrt{\varepsilon}$, the damping and scattering coefficients in Eq. (4.6) simplify for $K = 0$ to $\alpha_\pm = k_{\mathrm{i}}\big(|n|^2/n_{\mathrm{r}}^2 + n_{\mathrm{r}}^2/|n|^2\big)$ and $\beta_\pm = k_{\mathrm{i}}\big(|n|^2/n_{\mathrm{r}}^2 - n_{\mathrm{r}}^2/|n|^2\big)$. In the limit of small losses, one can approximate $|n| \approx n_{\mathrm{r}}$ in which case

the RTE coefficients approach the classical values $\alpha_{\pm} \approx 2k_{\mathrm{i}}$ and $\beta_{\pm} \approx 0$. For larger losses, however, the scattering coefficients become nonzero. For example, in the case of a dielectric material with refractive index $n = 2 + i$, the coefficients are given by $\alpha_{\pm} = 2.05k_0$ and $\beta_{\pm} = 0.45k_0$. The damping coefficient is still close to the classical value, but the scattering coefficient clearly deviates from the classical result of zero. This indicates that a part of photons is scattered backwards from the original direction.

*Single-interface geometry*

In order to illustrate the general position dependence of the obtained RTE coefficients, we have also investigated how these coefficients behave in an example single-interface geometry near the interface. The calculations are done for photon energy $\hbar\omega = 1$ eV ($\lambda = 1.24$ $\mu$m) assuming normal incidence and using refractive indices $n_1 = \sqrt{\varepsilon_1} = 2.5 + 0.5i$ and $n_2 = \sqrt{\varepsilon_2} = 1.5 + 0.3i$ for the lossy semi-infinite media.

Figure 4.9(a) shows the normalized damping coefficients $\alpha_+/k_0$ and $\alpha_-/k_0$ as a function of position. Near the interface, the damping coefficients are clearly oscillatory. These oscillations originate from interference and the related position-dependent emission and absorption rates in analogy with the Purcell effect [171]. Far from the interface, the damping coefficients saturate to homogeneous field values $1.00077k_0$ and $0.60046k_0$. These values are seen to be very close to the classical values $2k_{1,\mathrm{i}} = k_0$ and $2k_{2,\mathrm{i}} = 0.6k_0$.

Figure 4.9(b) presents the position dependence of the scattering coefficients $\beta_+$ and $\beta_-$. At certain distances from the interface, these coefficients are seen to obtain negative values, which is expected to be an indication of a dominant role of destructive interference between propagating fields. Compared to the values of the damping coefficients $\alpha_+$ and $\alpha_-$ in Fig. 4.9(a), the values of the scattering coefficients $\beta_+$ and $\beta_-$ in Fig. 4.9(b) are generally smaller. This is an expected result as the change of the field propagating in one direction generally depends more on the field itself than on the field propagating in the opposite direction assuming that these fields are of equal strength. Far from the interface, the scattering coefficients saturate to the homogeneous space values $0.03923k_0$ and $0.02354k_0$, which slightly deviate from the classical result of zero.
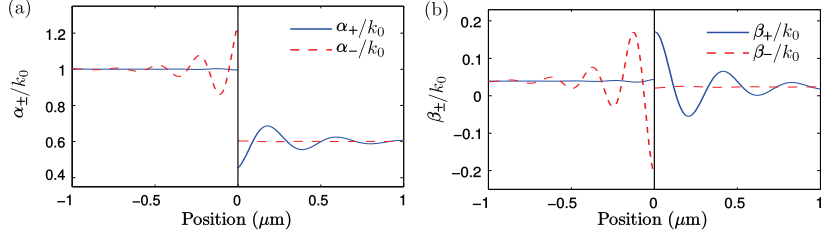
**Figure 4.9.** (a) Normalized damping coefficients $\alpha_+/k_0$ and $\alpha_-/k_0$ and (b) scattering coefficients $\beta_+/k_0$ and $\beta_-/k_0$ for photon energy $\hbar\omega = 1$ eV ($\lambda = 1.24$ $\mu$m) as a function of position near an interface between two lossy dielectric media. The refractive indices of the left and right media are $n_1 = 2.5 + 0.5i$ and $n_2 = 1.5 + 0.3i$. The interface between the media is represented by the vertical solid line. Figure adapted from Publication VII.

*Two-interface resonator*

Next we review the results obtained by applying the interference-exact RTE model to the geometry of a dielectric slab that acts as a two-interface resonator. The refractive index of the slab is $n = 2 + 0.1i$ and it is placed in vacuum. Figure 4.10(a) presents the coefficients of our RTE model as a function of position for normal incidence in the resonator geometry. The calculations were done for photon energy $\hbar\omega = 0.46$ eV ($\lambda = 2.68$ $\mu$m), which corresponds to the second constructive interference of the field reflected from the slab, i.e., the intensity of the reflected field obtains its second maximum when it is drawn as a function of frequency. The RTE coefficients clearly oscillate in the slab and become zero in vacuum outside the slab, where there are no losses. Even though the RTE coefficients have similarities with the densities of states, they are however significantly different.

We also compared the results of our RTE model to the classical exact method directly solving the fields by using Maxwell's equations with appropriate boundary conditions. In this comparison presented in Fig. 4.10(b), we plotted the net absorption rate, which is the negative divergence of the Poynting vector, as a function of position since it is well known to oscillate inside lossy resonant structures due to interference and the related Purcell effect. The conventional RTE model and other models that neglect interference effects cannot describe these oscillations correctly. The calculations were done by using the initial condition that there is no field incident from the right. The fixed average photon numbers on the right are $\langle \hat{n}_+ \rangle = 1$ and $\langle \hat{n}_- \rangle = 0$. In the classical field-based method, this boundary condition corresponds to fixing the electric and magnetic fields
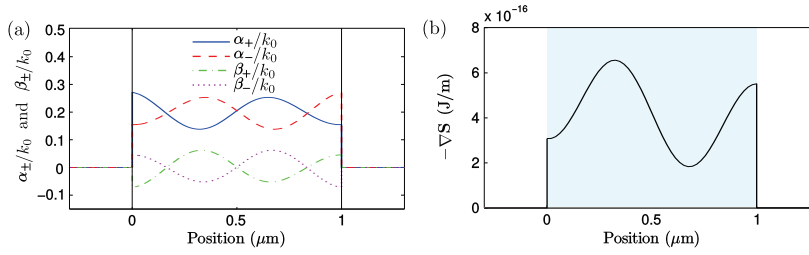
**Figure 4.10.** (a) Normalized damping coefficients $\alpha_\pm/k_0$ and scattering coefficients $\beta_\pm/k_0$ and (b) the spectral net absorption rate as a function of position for normal incidence in the resonator geometry, where a dielectric slab with refractive index $n = 2 + 0.1i$ is placed in vacuum. The plots are done for photon energy $\hbar\omega = 0.46$ eV ($\lambda = 2.68$ μm), which corresponds to the second resonance of the reflected field. In this configuration, the slab has a total power reflection coefficient of $R = 0.26$. The boundaries of the slab are represented by the vertical solid lines. Figure adapted from Publication VII.

on the right so that the resulting Poynting vector is the same as that in our interference-exact RTE model. The Poynting vector is calculated from the left and right propagating photon numbers of the RTE model by using Eq. (3.24). Only a single graph is visible in Fig. 4.10(b) as the results of the methods are equal within the numerical accuracy of the computations. This result clearly demonstrates that, by using the position-dependent damping and scattering coefficients of our method, the conventional RTE model can be generalized to account for interference effects.

## 4.3   Covariant theory and mass transfer

In Publication VIII, we applied the OCD model reviewed in Sec. 3.2.3 to present numerical simulations of the mass and momentum transfer and the related recoil effect and the relaxation of the resulting mass non-equilibrium when a light pulse propagates in a medium. The obtained results were then compared to the results of the MP quasiparticle model reviewed in Sec. 3.2.2 finding full agreement within the numerical accuracy of the simulations.

We assumed a titanium-sapphire laser pulse with a wavelength $\lambda_0 = 800$ nm ($\hbar\omega_0 = 1.55$ eV) and the total electromagnetic energy $E_0 = 5$ mJ. This corresponds to the photon number of $N_0 = E_0/\hbar\omega_0 = 2.0 \times 10^{16}$. The Gaussian form of the electromagnetic wave packet was assumed to propagate in the $x$ direction. The simulation geometry of a cubic diamond crystal block with anti-reflective coatings is illustrated in Fig. 4.11. The
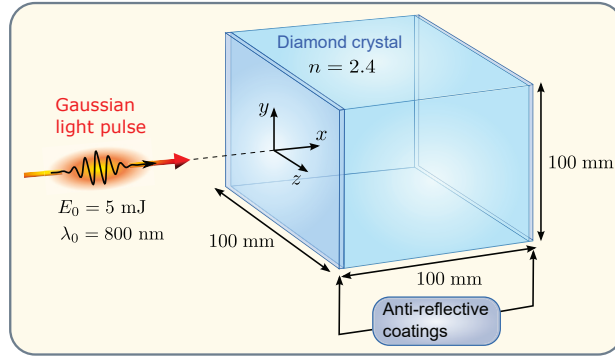
**Figure 4.11.** Illustration of the simulation geometry that consists of a cubic diamond crystal block with refractive index $n = 2.4$ coated with anti-reflective coatings. A Gaussian light pulse of energy $E_0 = 5$ mJ and central wavelength $\lambda_0 = 800$ nm is normally incident to the crystal from the left and propagates in the direction of the positive $x$-axis. The center of the light pulse enters the crystal at $x = y = z = 0$ mm. The second interface is located at $x = 100$ mm. Figure adapted from Publication VIII.

first and the second interfaces of the crystal are located at $x = 0$ mm and $x = 100$ mm. In the $y$ and $z$ directions, the geometry is centered so that the trajectory of the light pulse follows the line $y = z = 0$ mm. As material parameters for diamond, we used the refractive index $n = \sqrt{\varepsilon_r} = 2.4$ [183], mass density $\rho_0 = 3500$ kg/m$^3$ [184], bulk modulus $B = 443$ GPa [185], and shear modulus $G = 478$ GPa [186].

### 4.3.1  Mass transfer in one dimension

In the one-dimensional simulations, the simulation geometry corresponds to a plate that is infinite in the $y$ and $z$ directions but has the same thickness of $100$ mm in the $x$ direction as the three-dimensional block illustrated in Fig. 4.11. As an exact solution to Maxwell's equations, the electric field of the one-dimensional Gaussian pulse, with energy $E_0$ per cross-sectional area $A$, is given by

$$\mathbf{E}(\mathbf{r}, t) = \sqrt{\frac{2n\Delta k_x E_0}{\pi^{1/2}\varepsilon_0\varepsilon_r A(1+e^{-(k_0/\Delta k_x)^2})}} \cos\left[nk_0(x-ct/n)\right] e^{-(n\Delta k_x)^2(x-ct/n)^2/2}\hat{\mathbf{y}}.$$

(4.8)

The corresponding magnetic field is obtained by using Faraday's law in Eq. (2.1). Here $k_0 = \omega_0/c$ and $\Delta k_x$ are the wave number and its standard deviation corresponding to the central frequency $\omega_0$ in vacuum. In our simulations, we assumed that the relative spectral width of the pulse is $\Delta\omega/\omega_0 = \Delta k_x/k_0 = 10^{-5}$. The corresponding standard deviations of the

pulse width in space and time are $\Delta x = 1/(\sqrt{2}\Delta k_x) \approx 9$ mm and $\Delta t = \Delta x/c \approx 30$ ps. The normalization factor in Eq. (4.8) was determined so that the integral of the corresponding instantaneous energy density over $x$ gives $E_0/A$. In the simulations, we assumed a very high power per unit area as we used the small cross-sectional area given by $A = (\lambda/2)^2$, where $\lambda = \lambda_0/n$ is the wavelength in the crystal. This allowed us to attain an order of magnitude estimate of how large atomic displacements we would obtain if the whole vacuum energy $E_0 = 5$ mJ of the laser pulse could be coupled to a free-standing waveguide having a cross section $(\lambda/2)^2$. Without reducing the resulting atomic displacements in the crystal, the high power density could also be lowered by increasing the temporal width of the pulse.

Figure 4.12(a) presents the position dependence of the MDW when the light pulse is propagating in the middle of the crystal. This MDW is from the simulation where the optical force density was time-averaged over the harmonic cycle allowing us to use a coarse space and time discretization. As described in Sec. 3.2.3, the MDW mass density is the difference of the actual and equilibrium mass densities inside the crystal as $\rho_{\mathrm{MDW}}(\mathbf{r}, t) = \rho_{\mathrm{a}}(\mathbf{r}, t) - \rho_0$. The MDW is found to follow the Gaussian form of the pulse as expected. The mass density disturbance at the first interface resulting from the interface force is not shown in the figure. The subgraph focused near $x = 55$ mm shows the oscillations in the MDW obtained by using a finer discretization and the non-time-averaged optical force density following from the exact instantaneous fields. The Gaussian envelope of the pulse cannot be seen in the scale of this subgraph. As an integral of the MDW mass density, one obtains the total transferred mass carried by the MDW. In our example, we obtained the total transferred mass given by $2.6 \times 10^{-19}$ kg. This corresponds to the mass 7.4 eV/$c^2$ per photon in agreement with the MP quasiparticle model, where the transferred mass is calculated by using Eq. (3.44).

Figure 4.12(b) presents the position dependence of the atomic displacements obtained at the same instant of time as the MDW in Fig. 4.12(a). The negative atomic displacement at the first interface follows from the interface force and is required by the conservation law of momentum to balance the momentum increase between the photon momentum in vacuum and the MP momentum in the medium. The atomic displacements at the interfaces were calculated only approximatively in our simulations as
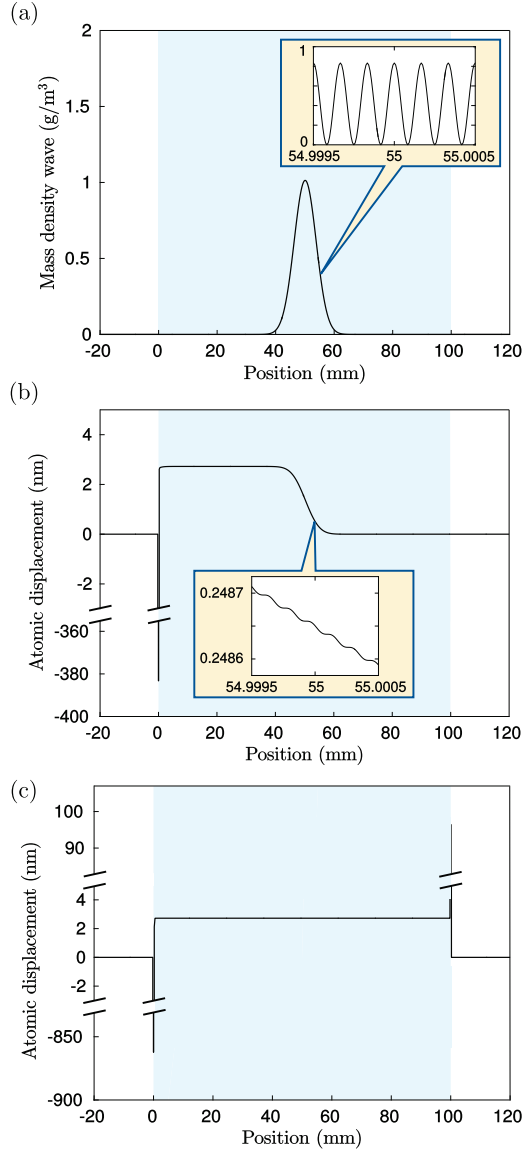
(a)



(b)



(c)



**Figure 4.12.** Simulation of the mass transfer of a Gaussian light pulse in one dimension. (a) Mass density of the MDW as a function of position when the light pulse is propagating in the middle of the crystal. This graph is calculated by averaging the optical force density over the harmonic cycle. The region of the crystal between $x = 0$ mm and $x = 100$ mm is represented by the light blue background. The focused subgraph shows the exact instantaneous MDW near $x = 55$ mm. (b) Atomic displacements at the same moment when the light pulse is propagating in the middle of the crystal obtained again with time-averaging over the harmonic cycle. The focused subgraph shows the exact atomic displacements near $x = 55$ mm. (c) The atomic displacements when the light pulse has just left the crystal. Note the breaks in the scales of the figures that are related to the larger atomic displacements at the interfaces. Figure adapted from Publication VIII.

the near interface dependence of the refractive index was not taken into account. There is a constant positive atomic displacement of $2.7$ nm on the left from the light pulse that is propagating in the middle of the crystal. On the right of the light pulse the atomic displacement drops to zero as the light pulse has not yet reached these positions. Due to the difference of the atomic displacements on the left and right of the light pulse, the atoms are more densely spaced at the position of the light pulse, which is related to the MDW mass density in Fig. 4.12(a). The subgraph focused near $x = 55$ mm presents the harmonic cycle level variations in atomic displacements obtained by using a finer discretization and the non-time-averaged optical force density following from the exact instantaneous fields.

Figure 4.12(c) presents the atomic displacements just after the light pulse has left the crystal. As expected, atoms inside the crystal have been displaced forward from their initial positions, while the atoms at the interfaces of the crystal have been displaced outwards due to the interface forces. The atomic displacements at the interfaces are changing as a function of time as the elastic forces try to re-establish the mass equilibrium in the crystal. This relaxation is a much slower process than the propagation of light through the crystal as it takes place at the velocity of sound. The relaxation will be studied in more detail in the case of the three-dimensional simulations reviewed in Sec. 4.3.2.

### 4.3.2 Mass transfer of a three-dimensional pulse

Next we review the simulations performed in the full three-dimensional geometry of Fig. 4.11. These simulations were done to give a deeper insight to the strain fields and their relaxation by sound waves. The three-dimensional simulations are computationally much more demanding compared to the one-dimensional simulations reviewed above. Therefore, we performed these simulations only by using a coarse grid and averaging the optical force density over the light pulse. The one-dimensional simulations had shown that this method is very accurate in the simulation of the transferred mass and momentum but the interface forces are modeled only approximately. In the three-dimensional case, a Gaussian light pulse is also known to be only an approximative solution to Maxwell's equations. For a more detailed description of the light pulse and the approximations made in these three-dimensional simulations, see Publication VIII.

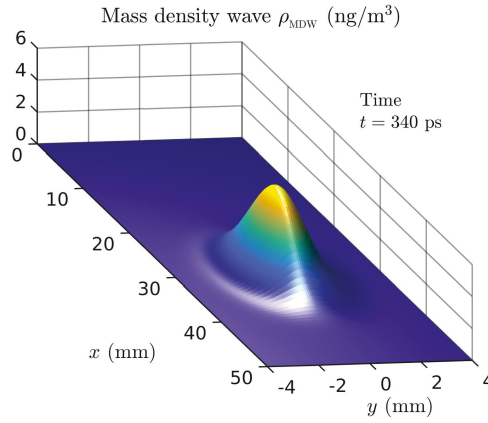Figure 4.13 presents the position dependence of the three-dimensional

**Figure 4.13.** Simulation of the MDW driven by optoelastic forces of a three-dimensional Gaussian light pulse. The figure shows the mass density of the MDW at time $t = 340$ ps after the start of the simulation. The light pulse propagates in the direction of the positive $x$-axis. The first interface of the crystal is located at $x = 0$ mm and the second interface at $x = 100$ mm, not shown in this figure. The mass density perturbance at the first interface is not drawn. Figure adapted from Publication VIII.

MDW in the $x$-$y$ plane at a specific time $t = 340$ ps of the simulation when the light pulse is propagating inside the crystal. As in the case of the one-dimensional MDW in Fig. 4.12, by integrating the MDW mass density in Fig. 4.13 and dividing the result with the photon number of the light pulse, we obtain the total transferred mass per photon of $7.4$ eV/$c^2$ within the numerical accuracy of the simulation. Therefore, the MP and OCD model results are found to be fully consistent with each other.

Figure 4.14(a) shows the position dependence of the $x$-component of the atomic displacements on $x$ axis at time $t = 340$ ps corresponding to the MDW in Fig. 4.13. The constant atomic displacement after the light pulse is $1.5 \times 10^{-17}$ m, which is much smaller than in the one-dimensional simulation in Fig. 4.12, where we assumed that the whole field energy propagates in a small cross-sectional area $A = (\lambda/2)^2$ as discussed above. The order of magnitude of the negative atomic displacement at the interface is $10^{-15}$ m, which is not shown in the scale of the figure. In Fig. 4.14(b), the same $x$-component of the atomic displacements is plotted as a function of $x$ and $y$ in the plane $z = 0$ mm. Away from the path of the pulse along the $y$-coordinate, the atomic displacement reaches zero as the optical force density acts only in the region of the light pulse and the elastic forces have not had time to displace atoms in this short time scale.

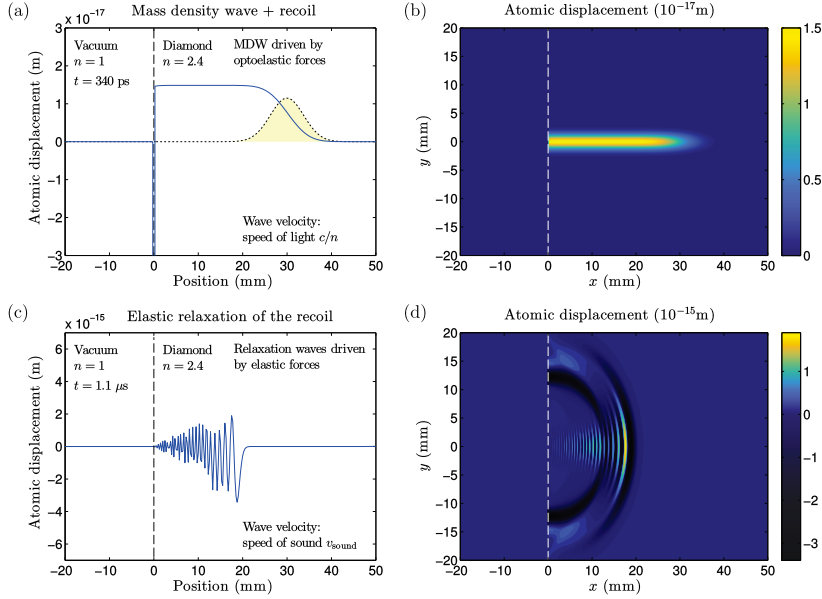Figure 4.14(c) shows the atomic displacements on the $x$ axis at a much

**Figure 4.14.** Simulation of the atomic displacements due to optical and elastic forces as a three-dimensional Gaussian light pulse propagates through a diamond crystal. (a) The $x$-component of the atomic displacements as a function position on the $x$ axis at time $t = 340$ ps. The dotted line represents the position of the Gaussian light pulse whose optical force density drives the MDW forward at velocity $v = c/n$. Atoms in a thin interface layer at $x = 0$ mm have recoiled to the left. (b) The corresponding atomic displacements plotted in the $x$-$y$ plane. (c) The same simulation at a later time $t = 1.1$ $\mu$s when the light pulse has gone and the recoil of the interface atoms starts to relax. Elastic waves propagate to the right at the velocity of sound. (d) The corresponding atomic displacements plotted in the $x$-$y$ plane. The position of the first interface of the crystal is represented by the dashed line. The second interface of the crystal is located at $x = 100$ mm, not shown in this figure. Therefore, in (c) and (d), we see only the relaxation transient close to the first interface of the crystal. Due to the very approximative treatment of the near interface region, only the order of magnitude of atomic displacements and the positions of the two wide wavefront are physically significant in (c) and (d). Figure adapted from Publication VIII.

later time $t = 1.1$ $\mu$s when the light pulse has left the crystal and is far away and the non-equilibrium atomic displacements at the interfaces have started to be relaxed by elastic forces. The simulation shows that the atomic displacements in Fig. 4.14(c) form elastic waves that propagate to the right at the speed of sound. Only the relaxation transient close to the first interface of the crystal is shown as the second interface of the crystal is at $x = 100$ mm. The positive constant atomic displacement inside the crystal seen in Figs. 4.14(a) and 4.14(b) is also being relaxed but it is very small and not visible in this scale. In Fig. 4.14(d), the same atomic displacements corresponding to Fig. 4.14(c) have been plotted as a function of $x$ and $y$ in the plane $z = 0$ mm. As the atomic displacements near the material interfaces were computed only approximatively, only the order of magnitude of the atomic displacements and the positions of the first and the second wide wavefront as a function of time are physically meaningful in Figs. 4.14(c) and 4.14(d). Since there does not exist any physical mechanism to return the energy of the elastic waves in Figs. 4.14(c) and 4.14(d) back to the light pulse, the OCD approach leads to the dissipation of the light pulse energy. In the simulations, we found that the recoil effect is the main source of the energy loss and it was roughly estimated to be of the order of $10^{-11}$ eV for the total light pulse, which corresponds to the fraction $10^{-28}$ of the total pulse energy, so it is very small compared to other physical nonidealities in a highly transparent real material.

# 5. Summary and conclusions

In this thesis, we have developed new models to study optical energy and momentum transfer and photon number in lossy and lossless microscopic and macroscopic structures. These investigations were mainly based on adopting the photon flow picture of the propagating electromagnetic fields, in which the electromagnetic field can be described either as waves or particles also inside resonant structures where interference effects are indispensable.

The research described in this thesis has, e.g., led to the development of the Green's functions-based QFED model that was shown to resolve the previously reported anomalies in the commutation relations of the photon ladder operators inside resonant structures. The field quantities of the QFED approach are equal to those in the conventional FED, but the QFED approach can be used to separate the field quantities to densities of states and the position-dependent photon numbers also in non-equilibrium conditions and in the case of fields propagating in different directions inside interfering structures. The propagating field representation also allowed bridging the results of QFED to the conventional RTE approach. This connection was shown to enable extending the applicability of the conventional RTE model beyond its main limitation in the description of interfering structures including near-field effects. In our interference-exact formulation of the RTE model, the wave and particle features associated with interference and emission in stratified geometries are fully captured by position-dependent damping and scattering coefficients.

To the best of our present knowledge, our QFED approach is the first and only way to consistently separate the optical fields in stratified media into left and right propagating components. Whereas previous methods

(FED, NOF) can be used to calculate any quantity corresponding to the field, energy density, or Purcell factor they do not provide the necessary information for analyzing the propagating fields without separation of the field quantities into parts propagating in different directions. As a first order differential equation, the derived RTE model provides an efficient method to compute the photon numbers and the related field quantities once the position-dependent damping and scattering coefficients of the problem geometry have been first computed. The next step in the further development of the interference-exact RTE model would be its extension to full three-dimensional geometries and the development of efficient methods to compute the position dependent damping and scattering coefficients. In general, the quantum optical RTE model has potential to become one of the standard approaches to model optical energy transfer in interfering structures.

In this thesis, we also investigated how the photon flow description of optical fields can be applied to study the momentum of light in a medium and to resolve the related Abraham–Minkowski controversy. This led to the derivation of the MP quasiparticle model, where light quanta in a medium are described as covariant coupled states of the field and matter providing a unique resolution to the Abraham–Minkowski controversy. The MP quasiparticle model also leads to the dissipation of photon energy when it propagates through transparent materials. The propagation of light in a medium was also studied using the OCD model, which coupled the electrodynamics of continuous media to continuum mechanics through Newton's equation of motion. Full agreement between the MP and OCD models was achieved within the numerical accuracy of the OCD simulations indicating that the wave and particle models are fully equivalent.

In general, the MP and OCD models provide independent but complementary views of how the covariance principle governs the propagation of light in a medium. In addition, the light associated MDW predicted by our theory implies a fundamental change in the understanding of light propagation in transparent materials. Our findings are also expected to raise new experimental interest in verifying the covariant state of light in a medium by measuring the transferred mass of a light pulse. On the theoretical side, the next steps include the generalization of the results for dispersive media and the more detailed studies of the interface and

dissipation effects. The simulations should also be performed for continuous light beams and incoherent fields, in which case one must presumably also account for the correlation properties of incoherent fields in the calculation of the optical force density and the related dynamics of the medium. Also nonlinear effects in the case of intense fields are worth of a careful study.

In addition to the main results above, we have studied several closely related topics and concepts and published some of the obtained results of these studies. The topics include the noiseless amplification of weak coherent fields using a beam-splitter-based setup and the Wigner function formalism; and the formation of local thermal balance, the field emission by magnetic source terms, and the three-dimensional Green's function representations in the QFED framework. Studying these topics has widened our understanding of the general applicability of the formalisms for different purposes and laid the foundation for the whole work described in this thesis.

The physics of light has been investigated for centuries leading to a manifold of different applications from incandescent light bulbs to modern optical communication technologies. On the theoretical side, the continuous research has led to the development of classical, quantum, and semiclassical theories. Future progress in the development of novel applications is more and more linked with the interplay of theoretical, computational, and experimental research. Therefore, transparent modeling tools that allow in-depth understanding of the phenomena of light in a sufficiently simple form are highly valuable. This thesis contributes to the scientific knowledge by providing new methods to modeling energy and momentum transfer in microscopic and macroscopic structures as well as by increasing the understanding of the relations of the energy and momentum transfer in the classical, quantum, and semiclassical theories. In particular, the results provide theoretical tools to study the wave–particle duality that is one of the most intriguing features of the field and matter that is deeply embedded into the foundations of quantum mechanics.

# References

[1] J. C. Maxwell, "On physical lines of force," *Phil. Mag.* **90**, 11 (1861).

[2] J. C. Maxwell, "A dynamical theory of the electromagnetic field," *Phil. Trans. R. Soc. Lond.* **155**, 459 (1865).

[3] P. A. M. Dirac, "The quantum theory of the emission and absorption of radiation," *Proc. R. Soc. Lond. A* **114**, 243 (1927).

[4] M. Born and P. Jordan, "Zur Quantenmechanik," *Z. Phys.* **34**, 858 (1925).

[5] M. Born, W. Heisenberg, and P. Jordan, "Zur Quantenmechanik. II." *Z. Phys.* **35**, 557 (1926).

[6] S. Tomonaga, "On a relativistically invariant formulation of the quantum theory of wave fields," *Prog. Theor. Phys.* **1**, 27 (1946).

[7] J. Schwinger, "On quantum-electrodynamics and the magnetic moment of the electron," *Phys. Rev.* **73**, 416 (1948).

[8] J. Schwinger, "Quantum electrodynamics. I. A covariant formulation," *Phys. Rev.* **74**, 1439 (1948).

[9] R. P. Feynman, "Space-time approach to quantum electrodynamics," *Phys. Rev.* **76**, 769 (1949).

[10] R. P. Feynman, "The theory of positrons," *Phys. Rev.* **76**, 749 (1949).

[11] R. P. Feynman, "Mathematical formulation of the quantum theory of electromagnetic interaction," *Phys. Rev.* **80**, 440 (1950).

[12] F. J. Dyson, "The radiation theories of Tomonaga, Schwinger, and Feynman," *Phys. Rev.* **75**, 486 (1949).

[13] S. M. Rytov, *Theory of Electric Fluctuations and Thermal Radiation*, Air Force Cambridge. Research Center, Bedford, Mass., AFCRC-TR-59-162 (1959).

[14] S. M. Rytov, Y. A. Kravtsov, and V. I. Tatarskii, *Principles of Statistical Radiophysics 3: Elements of Random Fields*, Springer, New York (1989).

[15] H. B. Callen and T. A. Welton, "Irreversibility and generalized noise," *Phys. Rev.* **83**, 34 (1951).

[16] U. Leonhardt, *Measuring the Quantum State of Light*, Cambridge University Press, Cambridge (1997).

[17] U. Leonhardt, "Quantum physics of simple optical instruments," *Rep. Prog. Phys.* **66**, 1207 (2003).

[18] L. Knöll, W. Vogel, and D.-G. Welsch, "Quantum noise in spectral filtering of light," *J. Phys. Am. B* **3**, 1315 (1986).

[19] L. Knöll, W. Vogel, and D.-G. Welsch, "Action of passive, lossless optical systems in quantum optics," *Phys. Rev. A* **36**, 3803 (1987).

[20] L. Knöll, W. Vogel, and D.-G. Welsch, "Resonators in quantum optics: A first-principles approach," *Phys. Rev. A* **43**, 543 (1991).

[21] L. Allen and S. Stenholm, "Quantum effects at a dielectric interface," *Opt. Commun.* **93**, 253 (1992).

[22] B. Huttner and S. M. Barnett, "Quantization of the electromagnetic field in dielectrics," *Phys. Rev. A* **46**, 4306 (1992).

[23] S. M. Barnett, R. Matloob, and R. Loudon, "Quantum theory of a dielectric-vacuum interface in one dimension," *J. Mod. Opt.* **42**, 1165 (1995).

[24] R. Matloob, R. Loudon, S. M. Barnett, and J. Jeffers, "Electromagnetic field quantization in absorbing dielectrics," *Phys. Rev. A* **52**, 4823 (1995).

[25] R. Matloob and R. Loudon, "Electromagnetic field quantization in absorbing dielectrics. II," *Phys. Rev. A* **53**, 4567 (1996).

[26] H. T. Dung, S. Y. Buhmann, L. Knöll, D.-G. Welsch, S. Scheel, and J. Kästel, "Electromagnetic-field quantization and spontaneous decay in left-handed media," *Phys. Rev. A* **68**, 043816 (2003).

[27] M. Ueda and N. Imoto, "Anomalous commutation relation and modified spontaneous emission inside a microcavity," *Phys. Rev. A* **50**, 89 (1994).

[28] M. G. Raymer and C. J. McKinstrie, "Quantum input-output theory for optical cavities with arbitrary coupling strength: Application to two-photon wave-packet shaping," *Phys. Rev. A* **88**, 043819 (2013).

[29] S. M. Barnett, C. R. Gilson, B. Huttner, and N. Imoto, "Field commutation relations in optical cavities," *Phys. Rev. Lett.* **77**, 1739 (1996).

[30] A. Aiello, "Input-output relations in optical cavities: A simple point of view," *Phys. Rev. A* **62**, 063813 (2000).

[31] O. Di Stefano, S. Savasta, and R. Girlanda, "Three-dimensional electromagnetic field quantization in absorbing and dispersive bounded dielectrics," *Phys. Rev. A* **61**, 023803 (2000).

[32] S. Gauvin, M. Collette, and N. Beaudoin, "Second harmonic generation inside microcavities: On the existence of a threshold," in *Frontiers in Optics 2014*, OSA (2014).

[33] M. Collette, N. Beaudoin, and S. Gauvin, "Second order optical nonlinear processes as tools to probe anomalies inside high confinement microcavities," *Proc. SPIE* **8772**, 87721D (2013).

[34] U. Leonhardt, "Momentum in an uncertain light," *Nature* **444**, 823 (2006).

[35] A. Cho, "Century-long debate over momentum of light resolved?" *Science* **327**, 1067 (2010).

[36] R. N. C. Pfeifer, T. A. Nieminen, N. R. Heckenberg, and H. Rubinsztein-Dunlop, "Colloquium: Momentum of an electromagnetic wave in dielectric media," *Rev. Mod. Phys.* **79**, 1197 (2007).

[37] S. M. Barnett, "Resolution of the Abraham-Minkowski dilemma," *Phys. Rev. Lett.* **104**, 070401 (2010).

[38] S. M. Barnett and R. Loudon, "The enigma of optical momentum in a medium," *Phil. Trans. R. Soc. A* **368**, 927 (2010).

[39] U. Leonhardt, "Abraham and Minkowski momenta in the optically induced motion of fluids," *Phys. Rev. A* **90**, 033801 (2014).

[40] B. A. Kemp, "Resolution of the Abraham-Minkowski debate: Implications for the electromagnetic wave theory of light in matter," *J. Appl. Phys.* **109**, 111101 (2011).

[41] P. W. Milonni and R. W. Boyd, "Momentum of light in a dielectric medium," *Adv. Opt. Photon.* **2**, 519 (2010).

[42] R. N. C. Pfeifer, T. A. Nieminen, N. R. Heckenberg, and H. Rubinsztein-Dunlop, "Constraining validity of the Minkowski energy-momentum tensor," *Phys. Rev. A* **79**, 023813 (2009).

[43] T. Ramos, G. F. Rubilar, and Y. N. Obukhov, "First principles approach to the Abraham-Minkowski controversy for the momentum of light in general linear non-dispersive media," *J. Opt.* **17**, 025611 (2015).

[44] M. Testa, "The momentum of an electromagnetic wave inside a dielectric," *Annals of Physics* **336**, 1 (2013).

[45] M. E. Crenshaw, "Decomposition of the total momentum in a linear dielectric into field and matter components," *Annals of Physics* **338**, 97 (2013).

[46] I. Brevik, "Minkowski momentum resulting from a vacuum-medium mapping procedure, and a brief review of Minkowski momentum experiments," *Ann. Phys.* **377**, 10 (2017).

[47] D. L. Andrews and M. Babiker, *The Angular Momentum of Light*, Cambridge University Press, Cambridge (2013).

[48] L. Allen, M. W. Beijersbergen, R. J. C. Spreeuw, and J. P. Woerdman, "Orbital angular momentum of light and the transformation of Laguerre-Gaussian laser modes," *Phys. Rev. A* **45**, 8185 (1992).

[49] M. W. Beijersbergen, L. Allen, H. E. L. O. van der Veen, and J. P. Woerdman, "Astigmatic laser mode converters and transfer of orbital angular momentum," *Opt. Commun.* **96**, 123 (1993).

[50] S. Nakamura and M. Krames, "History of gallium-nitride-based light-emitting diodes for illumination," *Proceedings of the IEEE* **101**, 2211 (2013).

[51] O. Heikkilä, J. Oksanen, and J. Tulkki, "Influence of internal absorption and interference on the optical efficiency of thin-film GaN-InGaN light-emitting diodes," *Appl. Phys. Lett.* **102**, 111111 (2013).

[52] V. J. Sorger and X. Zhang, "Spotlight on plasmon lasers," *Science* **333**, 709 (2011).

[53] R. F. Oulton, V. J. Sorger, R. Zentgraf, R.-M. Ma, C. Gladden, L. Dai, G. Bartal, and X. Zhang, "Plasmon lasers at deep subwavelength scale," *Nature* **461**, 629 (2009).

[54] L. Huang, X. Chen, H. Mühlenbernd, H. Zhang, S. Chen, B. Bai, Q. Tan, G. Jin, K.-W. Cheah, C.-W. Qiu, J. Li, T. Zentgraf, and S. Zhang, "Three-dimensional optical holography using a plasmonic metasurface," *Nat. Commun.* **4**, 2808 (2013).

[55] T. Sadi, J. Oksanen, J. Tulkki, P. Mattila, and J. Bellessa, "The Green's function description of emission enhancement in grated LED structures," *IEEE J. Sel. Top Quantum Electron.* **19**, 1 (2013).

[56] T. Taubner, D. Korobkin, Y. Urzhumov, G. Shvets, and R. Hillenbrand, "Near-field microscopy through a SiC superlens," *Science* **313**, 1595 (2006).

[57] R. Hillenbrand, T. Taubner, and F. Keilmann, "Phonon-enhanced light-matter interaction at the nanometre scale," *Nature* **418**, 159 (2002).

[58] K. Tanaka, E. Plum, J. Y. Ou, T. Uchino, and N. I. Zheludev, "Multifold enhancement of quantum dot luminescence in plasmonic metamaterials," *Phys. Rev. Lett.* **105**, 227403 (2010).

[59] N. Mattiucci, M. J. Bloemer, N. Aközbek, and G. D'Aguanno, "Impedance matched thin metamaterials make metals absorbing," *Sci. Rep.* **3**, 3203 (2013).

[60] P. Russell, "Photonic crystal fibers," *Science* **299**, 358 (2003).

[61] Y. Akahane, T. Asano, B. S. Song, and S. Noda, "High-Q photonic nanocavity in a two-dimensional photonic crystal," *Nature* **425**, 944 (2003).

[62] S. I. Bozhevolnyi, V. S. Volkov, E. Deveaux, J. Y. Laluet, and T. W. Ebbesen, "Channel plasmon subwavelength waveguide components including interferometers and ring resonators," *Nature* **440**, 508 (2006).

[63] B. Lamprecht, J. R. Krenn, G. Schider, H. Ditlbacher, M. Salerno, N. Felidj, A. Leitner, F. R. Aussenegg, and J. C. Weeber, "Surface plasmon propagation in microscale metal stripes," *Appl. Phys. Lett.* **79**, 51 (2001).

[64] Y. Zhai, Y. Ma, S. N. David, D. Zhao, R. Lou, G. Tan, R. Yang, and X. Yin, "Scalable-manufactured randomized glass-polymer hybrid metamaterial for daytime radiative cooling," *Science* (2017).

[65] A. Zavatta, J. Fiurášek, and M. Bellini, "A high-fidelity noiseless amplifier for quantum light states," *Nat. Photon.* **5**, 52 (2011).

[66] F. Ferreyrol, M. Barbieri, R. Blandino, S. Fossier, R. Tualle-Brouri, and P. Grangier, "Implementation of a nondeterministic optical noiseless amplifier," *Phys. Rev. Lett.* **104**, 123603 (2010).

[67] F. Ferreyrol, R. Blandino, M. Barbieri, R. Tualle-Brouri, and P. Grangier, "Experimental realization of a nondeterministic optical noiseless amplifier," *Phys. Rev. A* **83**, 063801 (2011).

[68] M. Barbieri, F. Ferreyrol, R. Blandino, R. Tualle-Brouri, and P. Grangier, "Nondeterministic noiseless amplification of optical signals: a review of recent experiments," *Laser Phys. Lett.* **8**, 411 (2011).

[69] V. Dunjko and E. Andersson, "Truly noiseless probabilistic amplification," *Phys. Rev. A* **86**, 042322 (2012).

[70] J. Bernu, S. Armstrong, T. Symul, T. C. Ralph, and P. K. Lam, "Theoretical analysis of an ideal noiseless linear amplifier for Einstein-Podolsky-Rosen entanglement distillation," *J. Phys. B* **47**, 215503 (2014).

[71] R. Blandino, M. Barbieri, P. Grangier, and R. Tualle-Brouri, "Heralded noiseless linear amplification and quantum channels," *Phys. Rev. A* **91**, 062305 (2015).

[72] S. Gröblacher, K. Hammerer, M. R. Vanner, and M. Aspelmeyer, "Observation of strong coupling between a micromechanical resonator and an optical cavity field," *Nature* **460**, 724 (2009).

[73] T. Häyrynen, J. Oksanen, and J. Tulkki, "Dynamics of cavity fields with dissipative and amplifying couplings through multiple quantum two-state systems," *Phys. Rev. A* **83**, 013801 (2011).

[74] T. Häyrynen, J. Oksanen, and J. Tulkki, "On the origin of divergences in the coincidence probabilities in cavity photodetection experiments," *J. Phys. B* **42**, 145506 (2009).

[75] S. Chandrasekhar, *Radiative transfer*, Dover, New York (1960).

[76] M. I. Mishchenko, *Electromagnetic Scattering by Particles and Particle Groups: An Introduction*, Cambridge University Press, Cambridge (2014).

[77] M. I. Mishchenko, "Directional radiometry and radiative transfer: The convoluted path from centuries-old phenomenology to physical optics," *J. Quant. Spectrosc. Radiat. Transfer* **146**, 4 (2014).

[78] M. I. Mishchenko, "Maxwell's equations, radiative transfer, and coherent backscattering: A general perspective," *J. Quant. Spectrosc. Radiat. Transfer* **101**, 540 (2006).

[79] M. I. Mishchenko, L. D. Travis, and A. A. Lacis, *Multiple Scattering of Light by Particles: Radiative Transfer and Coherent Backscattering*, Cambridge University Press, Cambridge (2006).

[80] L. de Broglie, "XXXV. A tentative theory of light quanta," *Philos. Mag.* **47**, 446 (1924).

[81] J. D. Jackson, *Classical Electrodynamics*, Wiley, New York (1999).

[82] J. E. Sipe, "New Green-function formalism for surface optics," *J. Opt. Soc.* **4**, 481 (1987).

[83] G. S. Agarwal, "Quantum electrodynamics in the presence of dielectrics and conductors. I. Electromagnetic-field response functions and black-body fluctuations in finite geometries," *Phys. Rev. A* **11**, 230 (1975).

[84] K. Joulain, J.-P. Mulet, F. Marquier, R. Carminati, and J.-J. Greffet, "Surface electromagnetic waves thermally excited: Radiative heat transfer, coherence properties and Casimir forces revisited in the near field," *Surf. Sci. Rep.* **57**, 59 (2005).

[85] A. Narayanaswamy and Y. Zheng, "A Green's function formalism of energy and momentum transfer in fluctuational electrodynamics," *J. Quant. Spectrosc. Radiat. Transf.* **132**, 12 (2014).

[86] A. G. Polimeridis, M. T. H. Reid, W. Jin, S. G. Johnson, J. K. White, and A. W. Rodriguez, "Fluctuating volume-current formulation of electromagnetic fluctuations in inhomogeneous media: Incandescence and luminescence in arbitrary geometries," *Phys. Rev. B* **92**, 134202 (2015).

[87] C.-T. Tai, *Dyadic Green's functions in electromagnetic theory*, Intext, Scranton, PA (1971).

[88] L. Novotny and B. Hecht, *Principles of Nano-Optics*, Cambridge University Press, Cambridge (2006).

[89] M. Paulus, P. Gay-Balmaz, and O. J. F. Martin, "Accurate and efficient computation of the Green's tensor for stratified media," *Phys. Rev. E* **62**, 5797 (2000).

[90] R. Carminati and J.-J. Greffet, "Near-field effects in spatial coherence of thermal sources," *Phys. Rev. Lett.* **82**, 1660 (1999).

[91] M. Francoeur and M. P. Mengüç, "Role of fluctuational electrodynamics in near-field radiative heat transfer," *J. Quant. Spectrosc. Radiat. Transf.* **109**, 280 (2008).

[92] K. Joulain, R. Carminati, J.-P. Mulet, and J.-J. Greffet, "Definition and measurement of the local density of electromagnetic states close to an interface," *Phys. Rev. B* **68**, 245405 (2003).

[93] A. Narayanaswamy and G. Chen, "Dyadic Green's functions and electromagnetic local density of states," *J. Quant. Spectrosc. Radiat. Transf.* **111**, 1877 (2010).

[94] N. M. J. Woodhouse, *Special Relativity*, Springer, Berlin (1992).

[95] V. Fock, "Konfigurationsraum und zweite Quantelung," *Z. Phys.* **75**, 622 (1932).

[96] P. Jordan and E. Wigner, "Über das Paulische Äquivalenzverbot," *Z. Phys.* **47**, 631 (1928).

[97] C. Cohen-Tannoudji, J. Dupont-Roc, and G. Grynberg, *Photons and Atoms: Introduction to Quantum Electrodynamics*, Wiley, New York (1989).

[98] R. Loudon, *The Quantum Theory of Light*, Oxford University Press, Oxford (2000).

[99] S. Scheel, L. Knöll, and D.-G. Welsch, "QED commutation relations for inhomogeneous Kramers-Kronig dielectrics," *Phys. Rev. A* **58**, 700 (1998).

[100] M. Khanbekyan, L. Knöll, D.-G. Welsch, A. A. Semenov, and W. Vogel, "QED of lossy cavities: Operator and quantum-state input-output relations," *Phys. Rev. A* **72**, 053813 (2005).

[101] E. Wigner, "On the quantum correction for thermodynamic equilibrium," *Phys. Rev.* **40**, 749 (1932).

[102] D. T. Smithey, M. Beck, M. G. Raymer, and A. Faridani, "Measurement of the wigner distribution and the density matrix of a light mode using optical homodyne tomography: Application to squeezed states and the vacuum," *Phys. Rev. Lett.* **70**, 1244 (1993).

[103] A. I. Lvovsky, H. Hansen, T. Aichele, O. Benson, J. Mlynek, and S. Schiller, "Quantum state reconstruction of the single-photon fock state," *Phys. Rev. Lett.* **87**, 050402 (2001).

[104] A. I. Lvovsky and M. G. Raymer, "Continuous-variable optical quantum-state tomography," *Rev. Mod. Phys.* **81**, 299 (2009).

[105] V. Parigi, A. Zavatta, M. Kim, and M. Bellini, "Probing quantum commutation rules by addition and subtraction of single photons to/from a light field," *Science* **317**, 1890 (2007).

[106] L. Zhang, H. B. Coldenstrodt-Ronge, A. Datta, G. Puentes, J. S. Lundeen, X.-M. Jin, B. J. Smith, M. B. Plenio, and I. A. Walmsley, "Mapping coherence in measurement via full quantum tomography of a hybrid optical detector," *Nat. Photon.* **6**, 364 (2012).

[107] C. W. Gardiner and P. Zoller, *Quantum Noise*, Springer, Berlin (2004).

[108] A. Uhlmann, "The 'transition probability' in the state space of a *-algebra," *Rep. Math. Phys.* **9**, 273 (1976).

[109] R. Jozsa, "Fidelity for mixed quantum states," *J. Mod. Opt.* **41**, 2315 (1994).

[110] J. Lee, M. S. Kim, and H. Jeong, "Transfer of nonclassical features in quantum teleportation via a mixed quantum channel," *Phys. Rev. A* **62**, 032305 (2000).

[111] W. P. Schleich, *Quantum optics in phase space*, Wiley-VCH, Berlin (2001).

[112] T. Gruner and D.-G. Welsch, "Quantum-optical input-output relations for dispersive and lossy multilayer dielectric plates," *Phys. Rev. A* **54**, 1661 (1996).

[113] C. F. Bohren and D. R. Huffman, *Absorption and Scattering of Light by Small Particles*, Wiley, Chichester, UK (1998).

[114] J. Lazar, O. Cip, J. Oulehla, P. Pokorny, A. Fejfar, and J. Stuchlik, "Position measurement in standing wave interferometer for metrology of length," in *Proc. SPIE 8306, Photonics, Devices, and Systems V*, 830607, SPIE (2011).

[115] M. Hola, J. Hrabina, O. Cip, A. Fejfar, J. Stuchlik, J. Kocka, J. Oulehla, and J. Lazar, "Nanopositioning with detection of a standing wave," in *Nanocon 2013, 5th International Conference* (2013).

[116] J. P. Pendry, A. J. Holden, D. J. Robbins, and W. J. Stewart, "Magnetism from conductors, and enhanced non-linear phenomena," *IEEE Trans. Microw. Theory Tech.* **47**, 2075 (1999).

[117] S. Tumanski, "Induction coil sensors—a review," *Meas. Sci. Technol.* **18**, R31 (2007).

[118] T. Häyrynen and J. Oksanen, "Quantum description of light propagation in generalized media," *J. Opt.* **18**, 025401 (2016).

[119] K. Inoue, "Quantum mechanical treatment of traveling light in an absorptive medium of two-level systems," *Opt. Commun.* **381**, 158 (2016).

[120] K. Inoue, "Quantum mechanical treatment of parametric amplification in an absorptive nonlinear medium," *Opt. Commun.* **383**, 69 (2017).

[121] B. Roy Bardhan and J. H. Shapiro, "Ultimate capacity of a linear time-invariant bosonic channel," *Phys. Rev. A* **93**, 032342 (2016).

[122] M. Planck, "Zur Theorie des Gesetzes der Energieverteilung im Normalspektrum," *Verh. Dtsch. Phys. Ges.* **2**, 237 (1900).

[123] M. E. Crenshaw, "Electromagnetic momentum and the energy–momentum tensor in a linear medium with magnetic and dielectric properties," *J. Math. Phys.* **55**, 042901 (2014).

[124] M. E. Crenshaw and T. B. Bahder, "Energy–momentum tensor for the electromagnetic field in a dielectric," *Opt. Commun.* **284**, 2460 (2011).

[125] M. E. Crenshaw and T. B. Bahder, "Electromagnetic energy, momentum, and angular momentum in an inhomogeneous linear dielectric," *Opt. Commun.* **285**, 5180 (2012).

[126] R. Loudon, S. M. Barnett, and C. Baxter, "Radiation pressure and momentum transfer in dielectrics: The photon drag effect," *Phys. Rev. A* **71**, 063802 (2005).

[127] M. Mansuripur, "Radiation pressure and the linear momentum of light in dispersive dielectric media," *Opt. Express* **13**, 2245 (2005).

[128] D. H. Bradshaw, Z. Shi, R. W. Boyd, and P. W. Milonni, "Electromagnetic momenta and forces in dispersive dielectric media," *Opt. Commun.* **283**, 650 (2010).

[129] P. W. Milonni and R. W. Boyd, "Recoil and photon momentum in a dielectric," *Laser Phys.* **15**, 1432 (2005).

[130] P. L. Saldanha, "Division of the momentum of electromagnetic waves in linear media into electromagnetic and material parts," *Opt. Express* **18**, 2258 (2010).

[131] C. Wang, "Can the Abraham light momentum and energy in a medium constitute a Lorentz four-vector?" *J. Mod. Phys.* **4**, 1123 (2013).

[132] C. Wang, "Self-consistent theory for a plane wave in a moving medium and light-momentum criterion," *Can. J. Phys.* **93**, 1510 (2015).

[133] M. Abraham, "Zur Elektrodynamik bewegter Körper," *Rend. Circ. Matem. Palermo* **28**, 1 (1909).

[134] M. Abraham, "Sull'elettrodinamica di Minkowski," *Rend. Circ. Matem. Palermo* **30**, 33 (1910).

[135] H. Minkowski, "Die Grundgleichungen für die elektromagnetischen Vorgänge in bewegten Körpern," *Nachr. Ges. Wiss. Göttn Math.-Phys. Kl.* 53 (1908), reprinted in Math. Ann. **68**, 472 (1910).

[136] P. Penfield and H. A. Haus, *Electrodynamics of Moving Media*, MIT Press, Cambridge, MA (1967).

[137] S. R. de Groot and L. G. Suttorp, *Foundations of Electrodynamics*, North-Holland, Amsterdam (1972).

[138] G. K. Campbell, A. E. Leanhardt, J. Mun, M. Boyd, E. W. Streed, W. Ketterle, and D. E. Pritchard, "Photon recoil momentum in dispersive media," *Phys. Rev. Lett.* **94**, 170403 (2005).

[139] R. E. Sapiro, R. Zhang, and G. Raithel, "Atom interferometry using Kapitza-Dirac scattering in a magnetic trap," *Phys. Rev. A* **79**, 043630 (2009).

[140] R. V. Jones and J. C. S. Richards, "The pressure of radiation in a refracting medium," *Proc. R. Soc. Lond. A* **221**, 480 (1954).

[141] R. V. Jones and B. Leslie, "The measurement of optical radiation pressure in dispersive media," *Proc. R. Soc. Lond. A* **360**, 347 (1978).

[142] G. B. Walker and D. G. Lahoz, "Experimental observation of Abraham force in a dielectric," *Nature* **253**, 339 (1975).

[143] A. F. Gibson, M. F. Kimmitt, and A. C. Walker, "Photon drag in germanium," *Appl. Phys. Lett.* **17**, 75 (1970).

[144] W. She, J. Yu, and R. Feng, "Observation of a push force on the end face of a nanometer silica filament exerted by outgoing light," *Phys. Rev. Lett.* **101**, 243601 (2008).

[145] L. Zhang, W. She, N. Peng, and U. Leonhardt, "Experimental evidence for Abraham pressure of light," *New J. Phys.* **17**, 053035 (2015).

[146] N. G. C. Astrath, L. C. Malacarne, M. L. Baesso, G. V. B. Lukasievicz, and S. E. Bialkowski, "Unravelling the effects of radiation forces in water," *Nat. Commun.* **5**, 4363 (2014).

[147] A. Ashkin and J. M. Dziedzic, "Radiation pressure on a free liquid surface," *Phys. Rev. Lett.* **30**, 139 (1973).

[148] A. Casner and J.-P. Delville, "Giant deformations of a liquid-liquid interface induced by the optical radiation pressure," *Phys. Rev. Lett.* **87**, 054503 (2001).

[149] I. Brevik, "Experiments in phenomenological electrodynamics and the electromagnetic energy-momentum tensor," *Phys. Rep.* **52**, 133 (1979).

[150] A. Einstein, "Das Prinzip von der Erhaltung der Schwerpunktsbewegung und die Trägheit der Energie," *Ann. Phys.* **325**, 627 (1906).

[151] N. L. Balazs, "The energy-momentum tensor of the electromagnetic field inside matter," *Phys. Rev.* **91**, 408 (1953).

[152] J. Chen, Y. Wang, B. Jia, T. Geng, X. Li, L. Feng, W. Qian, B. Liang, X. Zhang, M. Gu, and S. Zhuang, "Observation of the inverse Doppler effect in negative-index materials at optical frequencies," *Nat. Photon.* **5**, 239 (2011).

[153] L. D. Landau, E. M. Lifshitz, and L. P. Pitaevskii, *Electrodynamics of Continuous Media*, Pergamon, Oxford (1984).

[154] G. Mavko, T. Mukerji, and J. Dvorkin, *The Rock Physics Handbook*, Cambridge University Press, Cambridge (2003).

[155] A. Bedford and D. S. Drumheller, *Introduction to Elastic Wave Propagation*, Wiley, Chichester (1994).

[156] W. K. Wootters and W. H. Zurek, "A single quantum cannot be cloned," *Nature* **299**, 802 (1982).

[157] D. Dieks, "Communication by EPR devices," *Physics Letters A* **92**, 271 (1982).

[158] V. Josse, M. Sabuncu, N. J. Cerf, G. Leuchs, and U. L. Andersen, "Universal optical amplification without nonlinearity," *Phys. Rev. Lett.* **96**, 163602 (2006).

[159] T. C. Ralph and A. P. Lund, "Nondeterministic noiseless linear amplification of quantum systems," in *Quantum Communication Measurement and Computing Proceedings of 9th International Conference*, edited by A. Lvovsky, 155–160, AIP, New York (2008).

[160] P. Marek and R. Filip, "Coherent-state phase concentration by quantum probabilistic amplification," *Phys. Rev. A* **81**, 022302 (2010).

[161] T. Häyrynen, J. Oksanen, and J. Tulkki, "Quantum trajectory model for photon detectors and optoelectronic devices," *Phys. Scr.* **T143**, 014011 (2011).

[162] J. Fiurášek, "Engineering quantum operations on traveling light beams by multiple photon addition and subtraction," *Phys. Rev. A* **80**, 053822 (2009).

[163] W. J. Munro, K. Nemoto, R. G. Beausoleil, and T. P. Spiller, "High-efficiency quantum-nondemolition single-photon-number-resolving detector," *Phys. Rev. A* **71**, 033819 (2005).

[164] G. Nogues, A. Rauschenbeutel, S. Osnaghi, M. Brune, J. M. Raimond, and S. Haroche, "Seeing a single photon without destroying it," *Nature* **400**, 239 (1999).

[165] C. Guerlin, J. Bernu, S. Deleglise, C. Sayrin, S. Gleyzes, S. Kuhr, M. Brune, J.-M. Raimond, and S. Haroche, "Progressive fields-state collapse and quantum non-demolition photon counting," *Nature* **448**, 889 (2007).

[166] P. Grangier, J. A. Levenson, and J.-P. Poizat, "Quantum non-demolition measurements in optics," *Nature* **396**, 537 (1998).

[167] M. Brune, S. Haroche, V. Lefevre, J.-M. Raimond, and N. Zagury, "Quantum nondemolition measurement of small photon numbers by Rydberg-atom phase-sensitive detection," *Phys. Rev. Lett.* **65**, 976 (1990).

[168] G. J. Milburn and D. F. Walls, "State reduction in quantum-counting quantum nondemolition measurements," *Phys. Rev. A* **30**, 56 (1984).

[169] M. S. Tomaš, "Green function for multilayers: Light scattering in planar cavities," *Phys. Rev. A* **51**, 2545 (1995).

[170] F. Intravaia and K. Busch, "Fluorescence in nonlocal dissipative periodic structures," *Phys. Rev. A* **91**, 053836 (2015).

[171] E. M. Purcell, "Spontaneous emission probabilities at radio frequencies," *Phys. Rev.* **69**, 681 (1946), Note B10 in "Proceedings of the American Physical Society" *Phys. Rev.* **69**, 674 (1946).

[172] E. Homeyer, P. Mattila, J. Oksanen, T. Sadi, H. Nykänen, S. Suihkonen, C. Symonds, J. Tulkki, F. Tuomisto, M. Sopanen, and J. Bellessa, "Enhanced light extraction from InGaN/GaN quantum wells with silver gratings," *Applied Physics Letters* **102**, 081110 (2013).

[173] T. Sadi, J. Oksanen, and J. Tulkki, "Effect of plasmonic losses on light emission enhancement in quantum-wells coupled to metallic gratings," *J. Appl. Phys.* **114**, 223104 (2013).

[174] M. M. Y. Leung, A. B. Djurisic, and E. H. Li, "Refractive index of InGaN/GaN quantum well," *J. Appl. Phys.* **84**, 6312 (1998).

[175] A. S. Barker and M. Ilegems, "Infrared lattice vibrations and free-electron dispersion in GaN," *Phys. Rev. B* **7**, 743 (1973).

[176] O. Ambacher, W. Rieger, P. Ansmann, H. Angerer, T. Moustakas, and M. Stutzman, "Electron transport characteristics of GaN for high temperature device modeling," *Sol. State Commun.* **97**, 365 (1996).

[177] A. B. Djurisic and E. H. Li, "Modeling the optical constants of hexagonal GaN, InN, and AlN," *J. Appl. Phys.* **85**, 2848 (1999).

[178] J. W. Trainor and R. K., "Some properties of InN films prepared by reactive evaporation," *J. Electron. Mater.* **3**, 821 (1974).

[179] T. L. Tansley and C. P. Foley, "Optical band gap of indium nitride," *J. Appl. Phys.* **59**, 3241 (1986).

[180] E. J. Zeman and G. C. Schatz, "An accurate electromagnetic theory study of surface enhancement factors for silver, gold, copper, lithium, sodium, aluminum, gallium, indium, zinc, and cadmium," *J. Phys. Chem.* **91**, 634 (1987).

[181] I. H. Malitson, "Refraction and dispersion of synthetic sapphire," *J. Opt. Soc. Am.* **52**, 1377 (1962).

[182] P. Wurfel, "The chemical potential of radiation," *J. Phys. C* **15**, 3967 (1982).

[183] H. R. Phillip and E. A. Taft, "Kramers-Kronig analysis of reflectance data for diamond," *Phys. Rev.* **136**, A1445 (1964).

[184] D. R. Lide, ed., *CRC Handbook of Chemistry and Physics*, CRC Press, Boca Raton, FL (2004).

[185] C. Kittel, *Introduction to Solid State Physics*, Wiley, Hoboken, NJ (2005).

[186] H. J. McSkimin and P. Andreatch, "Elastic moduli of diamond as a function of pressure and temperature," *J. Appl. Phys.* **43**, 2944 (1972).

BUSINESS +
ECONOMY

ART +
DESIGN +
ARCHITECTURE

SCIENCE +
TECHNOLOGY

CROSSOVER

**DOCTORAL**
**DISSERTATIONS**